SURFACE BRIGHTNESS DISTRIBUTIONS OF LATE-TYPE STARS

Sandra Victoria Jeffers

A Thesis Submitted for the Degree of PhD
at the
University of St Andrews

2005

Please use this identifier to cite or link to this item:
http://hdl.handle.net/10023/12941

THE UNIVERSITY OF ST ANDREWS

University
of
St Andrews

Surface Brightness Distributions of Late-Type Stars

Sandra Victoria Jeffers

Submitted for the degree of Ph.D.

September 2004

DECLARATION

I, Sandra Victoria Jeffers, hereby certify that this thesis, which is approximately 25,000 words in length, has been written by me, that it is the record of work carried out by me and that it has not been submitted in any previous application for a higher degree.

September 2004

I was admitted as a research student in October 2000 and as a candidate for the degree of Ph.D. in October 2000; the higher study for which this is a record was carried out in the University of St Andrews between 2000 and 2004.

September 2004

In submitting this thesis to the University of St Andrews I understand that I am giving permission for it to be made available for use in accordance with the regulations of the University Library for the time being in force, subject to any copyright vested in the work not being affected thereby. I also understand that the title and abstract will be published, and that a copy of the work may be made and supplied to any bona fide library or research worker.

September 2004

I hereby certify that the candidate has fulfilled the conditions of the Resolution and Regulations appropriate for the degree of Ph.D. in the University of St Andrews and that the candidate is qualified to submit this thesis in application for that degree.

September 2004

THE UNIVERSITY OF ST ANDREWS

Surface Brightness Distributions of Late-Type Stars

Submitted for the degree of Ph.D., September 2004

Sandra Victoria Jeffers

ABSTRACT

The aim of this work has been to increase our understanding of the surface brightness distributions of late-type stars through Doppler imaging and eclipse mapping techniques. Combining spectroscopic and photometric observations with the technique of Doppler Imaging, I have reconstructed surface images of the G2 V star He 699 (for 08 October 2000), which show high latitude and polar structures. In the case of the K0V star AB Dor, the Doppler images for January 1992 and November 1993 show a large polar cap with small dark features also present at intermediate to high latitudes. As the phase sampling of the observations was insufficient to apply the sheared-image method it was not possible to detect any differential rotation.

In the second part of my thesis I determine the surface brightness distribution of the primary component of the RS CVn eclipsing binary SV Cam. I have used extrapolated size distributions of sunspots to an active star to synthesize images of stellar photospheres with high spot filling factors. The resulting surface images, reconstructed with the Maxium Entropy eclipse mapping technique, show large spurious spot features at the quadrature points. It is concluded that two-spot modelling or chi-squared minimisation techniques are more susceptible to spurious structures being generated by systematic errors, arising from incorrect assumptions about photospheric surface brightness, than simple Fourier analysis of the light-curves.

Spectrophotometric data from 9 HST orbits, observed in November 2001, have been used to eclipse-map the primary component of SV Cam. In combination with its HIPPARCOS parallax it is found that the surface flux in the eclipsed low-latitude region is about 30% lower than computed from the best fitting PHOENIX model atmosphere. This flux deficit can only be accounted for if about a third of the primary's surface is covered with unresolved spots. However, when the spottedness from the eclipsed region is applied to the entire surface of the primary star, there still remains an unaccounted flux deficit. The remaining flux deficit is explained by the presence of a large polar spot extending down to latitude 48±6°.

When the Maximum Entropy eclipse mapping technique is used to fit SV Cam's lightcurve, the observed minus computed residuals show strong spurious peaks at the quadrature points. It is only possible to reduce these peaks with the addition of a polar cap and the reduction of the primary star's temperature, to account for the star being peppered with unresolvable spots. Motivated by this result we investigate the limb darkening of the primary component of SV Cam. The wavelength dependence of the limb darkening is analysed by sub-dividing the HST lightcurve into 10 bands of equal emission flux. Flux variations between the first and fourth contact of the primary eclipse indicate that the limb darkening decreases towards longer wavelengths, in accordance with published limb darkening laws. Comparing fits of ATLAS and PHOENIX model atmospheres we find a wavelength dependence of the best fitting model. Due to its smooth cutoff at the stellar limb, the spherical geometry of the PHOENIX model atmosphere gives the best fit during partial eclipse. Between the second and third contact the difference between spherical and plane-parallel geometry is less important.

ACKNOWLEDGMENTS

There are a great number of people that deserve thanks for their contributions not only to this thesis, but who also added to the enjoyment of my time at St Andrews over the last few years.

On a professional level, I would like to thank my supervisor Andrew Collier Cameron for providing me with a suitably challenging Ph.D. and for the numerous opportunities along the way. For valuable contributions to this work I would like to thank John Barnes, Jean-Francois Donati, and Jason Aufdenberg. Special thanks also go to Gaitee Hussain for facilitating a visit to CfA. I would also like to thank Tim Lister for installing Condor on the network here; without it, I'm not sure I would ever have finished.

I would like to acknowledge support from a PPARC studentship in conjunction with a scholarship from the University of St Andrews. I would also like to thank the Russell Trust for financing an observing run at the Anglo Australian Telescope. The Scottish International Education Trust also supported an observing run at Telescope Bernard Lyot with a collaborative visit to Observatoire Midi-Pyrenees.

On a personal level, I would like to thank my office mates, Chris John, Mildred, Tim, Ed, lardy and grumpy for many entertaining moments! Indeed those demonstrations on plant growing, projectile motion, strange collections, and tea brewing... are unlikely to be ever erased from my memory!!

I would like to thank my parents, Jonathan, Nicholas and of course Lucy for their enthusiasm, support and entertainment (!).. maybe it's just as well I didn't do solid state physics! I would also like to thank my extended family for their interest in my work.

Volkmar, what can I say? Without you the last one and half years would have been very different. Thank you.

CONTENTS

LIST OF FIGURES

LIST OF TABLES

CHAPTER 1

Introduction

Magnetic fields are often at the heart of astrophysical phenomena. On the large scale, magnetic fields thread the spiral arms and core of the Milky Way, and result in the formation of jets, narrow flows of material emanating from the galactic centre (Sagittarius A). On an intermediate scale magnetic fields play an important role in the structure and stability of the interstellar medium, for example in large molecular clouds. In the process of star formation, magnetic fields are particularly important as they provide an efficient means of the redistribution of angular momentum.

Magnetic fields are a crucial ingredient throughout a star's life. During the star formation phase, magnetic fields drive molecular outflows that brake the rotation in young stellar objects. During a star's T Tauri phase, magnetic fields give rise to surface activity and large X-ray fluctuations. Many late-type main-sequence and giant stars display magnetic activity signatures analogous to those observed on the Sun. Magnetic fields are also important during the final stages of a star's life. In the white dwarf phase magnetic field strengths can reach values that are many orders of magnitude greater than observed on the Sun, due to the conservation of magnetic flux. For higher mass stars, radio pulsars are considered to be magnetic neutron stars, and supernovae remnants such as the Crab Nebula also exhibit evidence, in the form of synchrotron radiation, for the presence of magnetic fields.

Individual stellar categories show a wealth of magnetic variability. Magnetic fields on stars are variable, with some undergoing polarity reversals, and spectral variability as in the case of peculiar A stars. RS Canum Venaticorum stars are chromospherically active stars in binary systems that display a host of magnetically induced phenomena throughout the electro-magnetic spectrum. Flare stars are among the most energetic stars, whose near-

UV fluxes can increase by a factor of 2 or more when magnetically trapped particles are released into the star's corona. Flares on the Sun are one of the most spectacular aspects of solar activity. They can dramatically change the magnetic field structure of the solar wind. Among the most impressive magnetically induced phenomena here on Earth are aurorae, where the excitation of oxygen and nitrogen atoms in the upper atmosphere by energetically charged particles results in diffuse forms of light in the Earth's atmosphere.

In the following section, I review the forms of solar magnetic activity throughout the Sun's atmosphere, and provide an insight into the dynamo mechanism that generates and sustains this activity. I then consider this in terms of the solar-stellar connection, and the implications it has for magnetic activity on late-type stars.

1.1 Solar Magnetic Activity

Sunspots are the most well recorded signature of solar activity. Numerous sightings of sunspots are present in historical records, starting with Theophrastus (374-287 B.C.). The most extensive records are those of the Chinese imperial courts starting from 165 B.C. In the west, the views of Aristotle on the incorruptibility of the heavens meant that sunspots were impossible, so that sightings were often interpreted as being transits of Mercury or Venus (van Helden 1996). The first surviving sunspot drawing is from the 'Chronicles of John of Worcester' in 1128. The drawing is shown in Figure 1.1.

The first telescopic observations of sunspots were made in England by Harriot on 8 December 1610, as evidenced through entries in his notebook. The first results to be published were those of Fabricius in 1611 from observations commencing 27 February 1611, who correctly interpreted their apparent motion as being related to the axial rotation of the Sun. Later that year on 21 October, Scheiner also began observing sunspots, while it was not until 3 May 1612 that Galileo began his observations. A difference of opinion as to the origin of sunspots led Galileo to write 'Letters on Sunspots', where he argued that the spots were rotating on the rotating Sun, as opposed to being satellites of the Sun. At this time, the Sun was thought of as the symbol of perfection, and a 'spotty and impure' Sun represented another blow to the traditional cosmos (Hoskin 1999). It was at the beginning of the twentieth century that the magnetic nature of sunspots was discovered, when Hale (1908) mapped the solar magnetic field using the Zeeman effect on

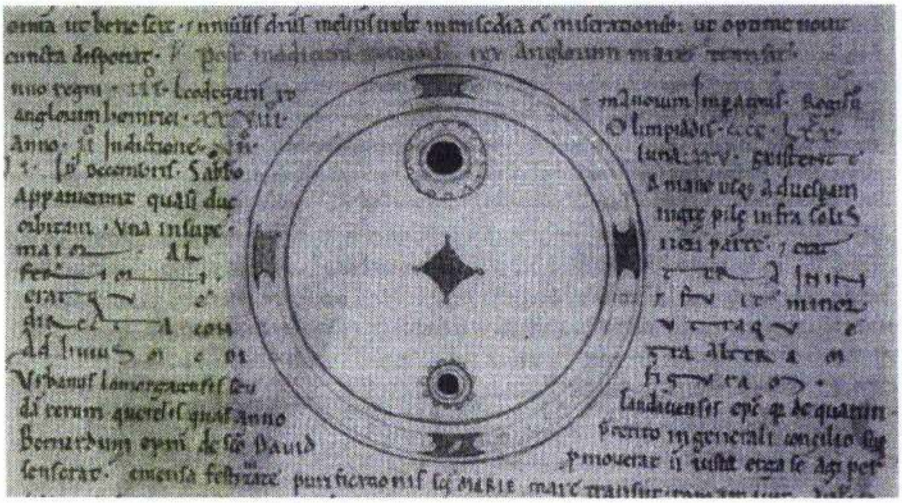

Figure 1.1: The first recorded drawing of a sunspot as described in 'The Chronicle of John of Worcester' (McGurk 1998).

the Sun's spectral lines.

1.1.1 Activity through the solar atmosphere

The solar magnetic field and its evolution in the solar atmosphere spans a wide spectrum of spatial and temporal scales. The timescales range from the global 11 year reversal in magnetic polarity down to seconds in the case of explosive events such as flares. The largest signatures of magnetic activity are the global approximately dipolar field and coronal loops, where mass streaming off the Sun drags magnetic field into space forming an extended heliosphere. The smallest magnetic features are magnetic flux tubes in the inter granular lanes on the solar surface that are below current resolution capabilities.

1.1.2 Photosphere

The base of the solar atmosphere is the photosphere, a thin (330 km) dense layer of plasma from which emanates the majority of visible solar radiation. The photospheric temperature and gas number density (Vernazza, Avrett & Loeser 1981) respectively range from 6600 K and $10^{23}\mathrm{m}^{-3}$ at its base, to 4300 K and $10^{21}\mathrm{m}^{-3}$ at its interface with the chromosphere. In the general case, the signatures of magnetic activity are concentrated in large active regions, as shown in Figure 1.2. The smallest magnetic features are the small scale flux

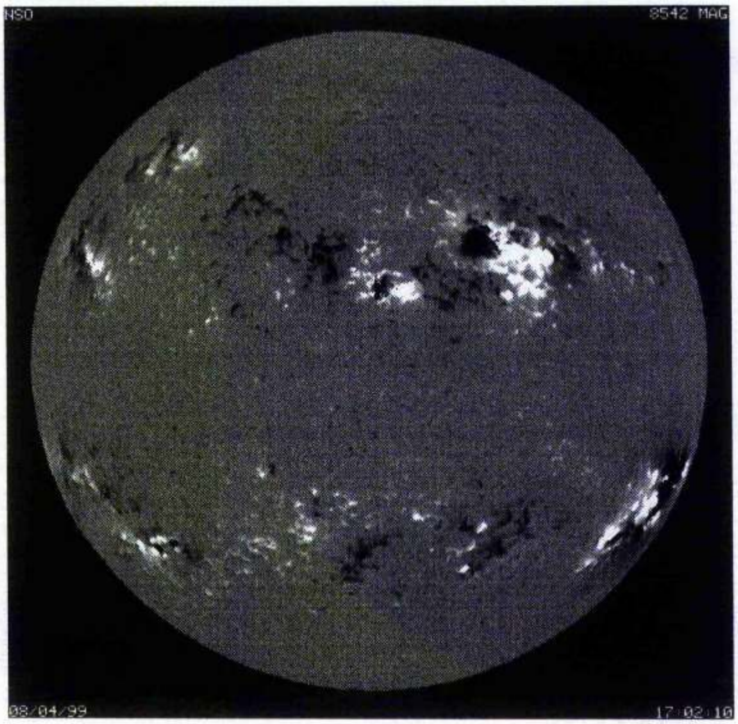

Figure 1.2: Solar magnetogram showing the presence of large active regions (image courtesy of the National Solar Observatory). Tick marks are 1000 km apart.

tubes with fields of 1.5 kG. They are typically located in the intergranular lanes, that are the cooler and darker downflow regions of convective motions. Pores are larger, with a clearly defined umbra and magnetic field strengths up to 2 kG. Larger flux concentrations develop filamentary penumbra that surround the umbra. Penumbrae distinguish spots from pores as shown in Figure 1.3.

The magnetic fields of sunspots have been measured, using Zeeman splitting, to be 1 to 3 kG (Livingston 2002). In contrast to this, the surface-averaged magnetic field has a field strength of the order of a few Gauss. The size distribution of magnetic features, spanning the range from 20,000 to 30,000 km in the case of the largest sunspots down to < 100 km in the case of flux tubes, follows a log-normal distribution (Bogdan et al. 1988). Sunspots mostly occur in bipolar pairs. At any stage of the solar cycle the preceding and following spots have opposite polarities in the northern and southern hemispheres, where the polarity of the leading spot is the same polarity as the polar field in the same hemisphere (Hale's law) . The preceding and following spots are linked through magnetic flux loops. The preceding spot lies east of the following spot and is generally closer to the equator (Joy's law). Sunspots are constrained to a latitude band around the equator

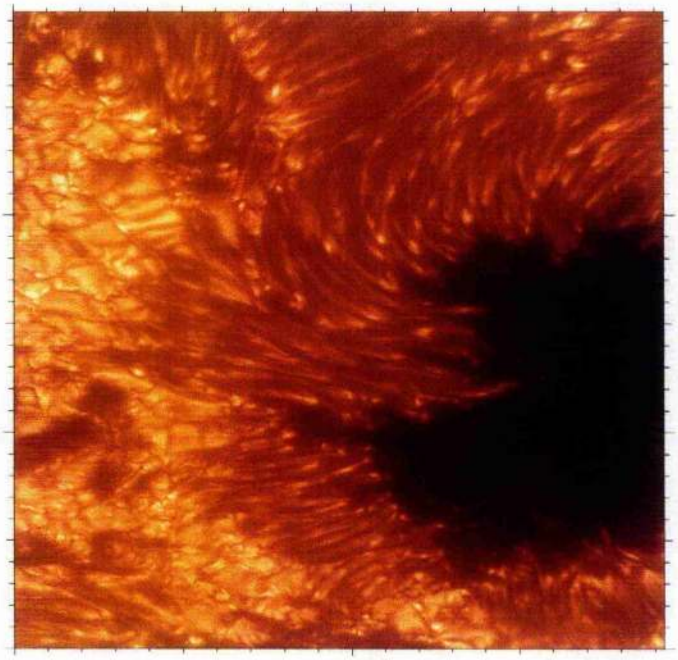

Figure 1.3: Umbra and penumbra of a spot (image courtesy of the Swedish 1-m Solar Telescope on La Palma)

of ±35°. During the solar cycle the latitude of flux emergence decreases resulting in the solar 'butterfly diagram'. In the following magnetic cycle the polarity of the leading spot reverses, making the 11 year cycle of the spot number a 22 year magnetic cycle. The total area of sunspots on the solar surface varies from 1.5×10^{-6} to 141×10^{-6} of the visible hemisphere (Bogdan et al. 1988).

Seen in white light, active regions are marked by photospheric faculae and are easily distinguishable on the solar limb, where the photosphere appears darker. The emission of the faculae, integrated over all wavelengths, outweighs the missing radiative flux caused by the presence of sunspots. As a result the total solar irradiation increases with solar activity. Between minimum and maximum activity this can result in a increase of approximately 0.1% (Fröhlich & Lean 1998).

1.1.3 Chromosphere

The chromosphere extends out about 2000 km from the top of the photosphere where its temperature increases steeply up to 2×10^4 K. Its gas density is less than the photosphere, decreasing to 10^{16} m^{-3} (Vernazza, Avrett & Loeser 1981) at the base of the transition

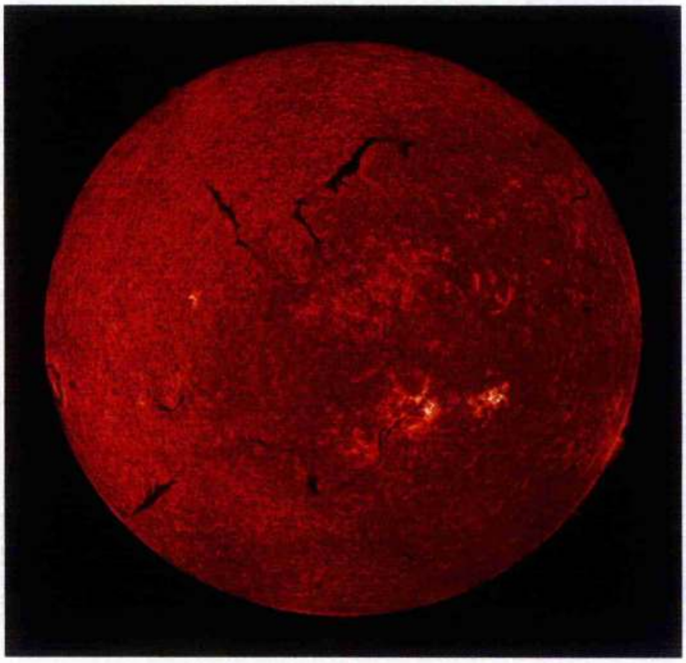

Figure 1.4: Photograph of the Sun in H_{α}, showing the chromospheric network, bright regions of plage, and long and dark filaments (image courtesy of the Big Bear Solar Observatory).

region. Chromospheric magnetic features are observed in UV and EUV regions of the electromagnetic spectrum. The chromospheric network is a web that follows the boundaries of supergranular cells, and is detected as emission in $H\alpha$ and in the cores of the H & K resonance lines of Ca II. The cores of these lines are formed above the temperature minimum in a region where temperature increases outwards, and so appear in emission. Above the active regions in the photosphere exist bright plages, which are the chromospheric equivalent of photospheric faculae visible predominantly in the spectral lines of Ca II, but also in H_{α}. They are regions where the density and the temperature are higher than in the surrounding chromosphere. The Mount Wilson survey of Ca II H&K has monitored these spectral lines in stars over 40 years, and is discussed further in later sections.

Prominences are cool dense clouds of chomospheric gas that extend into the corona, and are held in place by the Sun's magnetic field. Prominences seen in front of the solar disc are seen as dark filaments, but appear in emission at the solar limb. There are two main types of prominences: active prominences that are associated with solar flares, and last a few hours, and quiescent prominences that are more stable and can last up to a few months. They can extend for thousands of kilometres above the chromosphere, and exhibit motions that are dependant on the evolution of supporting magnetic loops (Priest & Smith 1979).

1.1.4 Transition region and corona

The transition region is a very thin layer of approximately 100 km between the chromosphere and the corona. It is characterised by a steep temperature gradient bridging the chromospheric temperature of 2×10^4 K to the coronal temperature of 2×10^6 K. This strongly dynamic region is subject to explosive events and high speed flows like jets (Dere & Subramanian 2001).

At solar eclipses the corona appears as a white halo extending several solar radii above the solar limb. The white halo results from the scattering of photospheric radiation by free electrons. Average coronal temperatures reach up to 2×10^6 K with a number density of approximately $10^{15}\,\mathrm{m}^{-3}$ (Vernazza, Avrett & Loeser 1981). The origin of such high temperatures is still debated, but is considered to result mainly from magnetic heating such as magnetic reconnection (Narain & Ulmschneider 1990). The magnetic topology of the solar corona comprises 'closed regions', where coronal loops connect active regions of opposite polarity in the photosphere, and large unipolar 'open regions', where the field lines extend far out into the solar system. The structure of closed regions is observed in X-ray and EUV emission as the magnetic field channels the mass and energy flows, as shown in Figure 1.5. In contrast, open regions show less emission, and are referred to as coronal holes. Here the coronal plasma can freely stream along open field lines, resulting in the emanation of the tenuous fast solar wind (with velocities up to $800\,\mathrm{km\,s^{-1}}$). Mass loss emanating from the vicinity of closed regions, e.g. helmet streamers and closed coronal loops and arches, forms the denser and variable slow solar wind (with velocities up to $400\,\mathrm{km\,s^{-1}}$).

The magnetic topology also changes on much shorter timescales such as coronal mass ejections that reach velocities up to $2000\,\mathrm{km\,s^{-1}}$. Other very energetic events are solar flares, which originate in the lower atmosphere through the reconnection of magnetic fields, but can extend up to 6×10^4 km above the solar limb, and reach temperatures of up to 10^7 K.

Figure 1.5: Transition Region And Coronal Explorer (TRACE) image of coronal loops.

1.2 Solar Dynamo

The global large scale magnetic field of the Sun could result from a primordial field as the decay timescale of such a magnetic field is of the order of 10^{10} years (Priest 1984) and comparable with the age of the Sun. The decay time assumes classical resistivity. However, due to the convective motions in the Sun, turbulent resistivity will dominate. As turbulent resistivity is many magnitudes greater than the classical value, the solar magnetic field would decay over a timescale that is shorter than the age of the Sun if it were not sustained by dynamo action. The solar magnetic field is observed to vary on timescales from seconds, in the case of flares, to decades in the case of the magnetic cycle. These timescales, in combination with magnetic cycle, could not be sustained by a primordial magnetic field and must result from dynamo mechanisms present in the solar interior.

The current solar interior comprises two zones. The outer 30% is a convection zone that surrounds a radiative zone. Helioseismological analyses of rotational splitting of solar p-modes indicate that the solar radiative zone rotates almost rigidly. This rigid rotation can be attributed to a weak fossil field of the order of 1 G (Kosovichev et al. 1997).

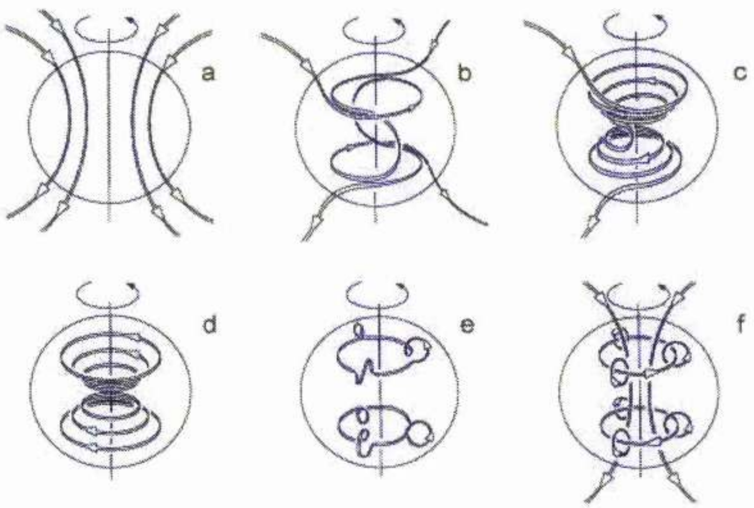

Figure 1.6: Schematic phases of the solar dynamo: (a) initial dipolar field. The Ω effect is shown in (b,c), where differential rotation wraps the magnetic field around the rotation axis creating (d). The cycle of the dynamo is completed by the α effect where loops of magnetic field are created (e). These loops then form the original dipolar field (f) (Love 1999).

1.2.1 Modes of dynamo operation

The generation and amplification of magnetic field by a dynamo process is a self-sustaining conversion of kinetic and thermal energy, in the form of solar (differential) rotation and convection, into magnetic energy (Parker 1955). Differential rotation, where the equator rotates faster than the poles, generates a toroidal (east-west) field from an initial poloidal (north-south) field, which is called the Ω effect. The presence of a toroidal field is confirmed by the east-west orientation and polarity rules of sunspots. The poloidal field is regenerated through the action of rising plasma in the convection zone and the twisting of convective motions due to the Coriolis force. The generation of the poloidal field is the α effect (Steenbeck, Krause & Rädler 1966). If the regenerated poloidal field is opposite in polarity to the original poloidal field then the toroidal field produced from this field will also have reverse polarity. The dynamo cycle is completed when a poloidal field of the same polarity as the original field has been generated, as is observed in the 22 year magnetic cycle on the Sun. The schematic phases of the solar dynamo are illustrated in Figure 1.6. The combined motions of convection and differential rotation are referred to as an $\alpha\Omega$ dynamo, where the Ω effect is dominant (Babcock 1965, Leighton 1964 and Leighton 1969).

Other modes of dynamo operation (Priest 1984) are $\alpha^2\Omega$-dynamo, which generates toroidal field with approximately equal contributions from the α-effect and Ω-effect, and the α^2-dynamo, where both the toroidal and poloidal fields are generated by the α-effect and the Ω-effect is relatively small. Kitchatinov & Rüdiger (1999) predict that a decrease in differential rotation with angular velocity may result in a change in the stellar dynamo from the $\alpha\Omega$ regime to the α^2 mechanism. The α^2-dynamos normally produce a steady (i.e. non-cyclic) but non-axisymmetric magnetic field (Rüdiger & Elstner 1994), providing a possible explanation as to why rapidly rotating young stars do not exhibit activity cycles (Baliunas et al. 1995). In the distributed dynamo the α and Ω effects operate throughout the convection zone, whereas in the shell dynamo model, the dynamo originates from the convective overshoot layer, that lies between the radiative core and the convective envelope (Spruit & Weiss 1980).

1.2.2 Flux tube emergence

It is considered that the solar dynamo operates in a thin layer of over-shooting below the solar convective zone (Galloway & Weiss 1981). The loop-like strands of magnetic field are expelled into the convection zone as a consequence of a non-axis-symmetric instability (Spruit & Van Ballegooijen 1982). During the amplification process of the toroidal field, its magnetic field strength increases. Beyond a critical field strength, an instability forms and leads to the formation of rising flux tubes (Choudhuri & Gilman 1987 and Choudhuri 1989). Once it is located in the convection zone it will continue to rise to the photosphere, and form the observed bi-polar magnetic regions.

1.3 Observations of Magnetic Activity on Late-type Stars

1.3.1 Solar-stellar connection

Many late-type stars display activity that is analogous to the solar magnetic features described in the previous section. This activity indicates that a dynamo mechanism is also present in their convective envelopes. The variation of stellar activity provides an indication as to how the dynamo is affected by stellar parameters such as age, mass, and rotation rate. On the other hand the Sun is the only star where it is possible to observe its internal structure, through helioseismology, and its outer structure in great detail, with both ground based and space based instruments.

In addition to this we have also learnt that tidal interaction between binary components can impart high rotation rates at later evolutionary stages leading to increased magnetic activity; that stellar rotation is slowed over time by stellar winds; that heating of the outer atmosphere results from the actions of the magnetic field and the damping of purely acoustic waves; and that convection requires rotation to excite a global dynamo that generates and maintains the stellar magnetic field.

1.3.2 Overview

Kron (1947) first proposed the starspot model to account for the out of eclipse photometric light variations of AR Lac. Later Hall (1976) defined a class of variable star, named after their prototype RS Canum Venaticorum (RS CVn), which exhibit large and variable spots. Evidence that G and K dwarfs in the Pleiades show short-period photometric variability was reported by van Leeuwen, Alphenaar & Meys (1987). Stauffer et al. (2003) attribute the anomalous spectral energy distribution the Pleiades K dwarfs to a spot filling factor of $\geq 50\%$. Other methods such as TiO-band strength analysis indicate that 20% to 40% of active star's surfaces are occupied by spots (O'Neal, Neff & Saar 1998).

The surface brightness distribution of late-type stars, resulting from magnetic activity, can be observed by using tomographic techniques such as Doppler imaging. The magnetic field strengths and topologies of late-type stars can be determined using Zeeman-Doppler imaging (Donati & Collier Cameron 1997). Doppler images have been applied to more than 50 (Strassmeier 2002) single and binary stars which are briefly summarised here.

1.3.3 Doppler Imaging

Deutsch (1958) and Deutsch (1970) first proposed the usage of line profiles to map the stellar surface of Ap stars while Goncharsky et al. (1982) developed the first surface image of an Ap star from a time-series of spectra, but it was Vogt & Penrod (1983) who first used the term Doppler imaging. The principles of this technique are well explained in the literature, e.g. Rice, Wehlau & Khokhlova (1989) and Collier Cameron (2001).

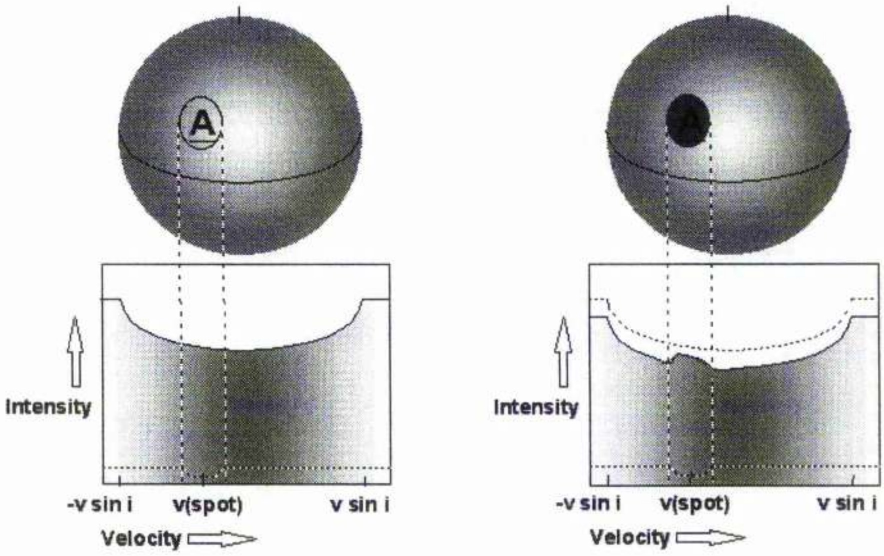

Figure 1.7: Illustration of the formation of a bright 'bump' on the rotationally broadened profile as as result of a spot on the stellar surface. (picture credit A.Collier Cameron)

A rapidly rotating star will have rotationally broadened photospheric lines since one limb of the star is approaching, while the other is receding. A starspot produces a bump in the rotationally broadened profile, as less light is removed at the Doppler shift of the spot relative to the centre of the line, causing a bright bump in every photospheric absorption line in the star's spectrum. This is illustrated in Figure 1.7. The velocity difference between a bump and the line centre is proportional to the projected distance of the feature from the rotation axis. As the star rotates, this bump will move across the rotationally broadened profile. The radial acceleration of the bump through the rotation profile is proportional to the spot's latitude. The axial inclination of the star can be determined from the length of time that high latitude spots remain visible. The resulting time-series of spectra thus contains sufficient information to reconstruct the map of the stellar surface that best fits the amplitude and velocity variations of the bump.

The effectiveness of the technique of Doppler imaging primarily depends on the ratio of the rotational broadening of the spectral line to the intrinsic line width. This imposes a lower limit on the required rotational velocity. Most stars that satisfy this criterion are fast rotators having high activity levels as rotation is a significant factor in the dynamo process that generates their activity.

1.3.4 Single stars

Doppler imaging has revealed the locations of star-spots on numerous single late-type stars ranging from T Tauri stars through main-sequence stars to evolved giants.

T Tauri stars represent the earliest evolutionary stages that are optically visible. They occupy the evolutionary stages from the very youngest protostellar objects, immersed in gas and dust, to solar-type stars on the main sequence. T Tauri stars are sub-classified according to the presence (classical T Tauri, CTT) or lack (weak T Tauri, WTT) of a circumstellar disc. Both classifications display a host of photometric and spectroscopic peculiarities related to their youth, activity and environment. Doppler imaging has revealed spots on the CTT Sz 68 (K2 IV) to be located at the rotation poles (Johns-Krull & Hatzes 1997), and on the CTT DF Tau (M0) to be located at high and low latitudes (Unruh, Collier Cameron & Guenther 1998). Spots on the WTT V410 Tau (K4) are present at both equatorial and high latitudes (Rice & Strassmeier 1996, Hatzes 1995), and at polar and high latitudes on the WTT PZ Tel (K0V-IV) (Barnes et al. 2000). Donati et al. (1997) provided the first *direct* measurement of a magnetic field on a WTT star.

Doppler imaging has revealed dark polar caps on main-sequence stars, with some low latitude structure present (Strassmeier & Rice 1998, Donati & Collier Cameron 1997, Jeffers, Barnes & Collier Cameron 2002). The latest spectral type to be Doppler imaged is M1-2V for HK Aqr, and RE1816+541 (EY Dra), where spots are present at all latitudes but without a polar cap (Barnes & Collier Cameron 2001).

To date there exists only a small sample of giant stars which have been Doppler imaged. These include HD 31993 (K2 III) where spots are present at high and low latitudes (Kratzwald 2002). Also included in this sample is CM Cam, which is considered to be effectively a single star of spectral type G8 II-III. It shows a polar cap, with spots also at high and low latitudes (Strassmeier et al. 1998).

Also included in the classification of giant stars are FK Com stars. The latitude distribution of spots on FK Com stars includes polar, high and low latitude structure e.g. HD 199178 (Strassmeier et al. 1999) and FK Com (Korhonen et al. 2001). These stars are particular noteworthy as they are the only single stars that exhibit active longitudes of flux emergence. The active longitudes also undergo a 'flip-flop' effect, where the relative strengths of the two active spot group alternate (Korhonen et al. 2001).

1.3.5 Binary stars

RS CVn stars (Hall 1976) are well established to exhibit signatures of magnetic activity in the same forms that are found on single stars. However some of these stars are considered to be tidally locked such that the stellar rotation period is synchronised with the binary rotation period. Tidal locking is considered to be responsible for the suppressed differential rotation on these stars, as noted by Petit, Donati & Collier Cameron (2002) and Vogt et al. (1999) from observations of HR 1099. It also has the effect of maintaining rapid rotation compared with single stars of the same spectral type.

Like single active stars, the active sub-giants in RS CVn systems exhibit dark polar caps. They have been observed on several RS CVns ranging in spectral type from G5 IV (El Eri – Washuettl, Strassmeier & Collier-Cameron 2001) to K1 IV (V711 Tau / HR 1099 – Petit, Donati & Collier Cameron 2002). High latitude and low latitude spots have been observed on RS CVns of spectral type F9V (SV Cam - Hempelmann et al. 1995) to K4 IV (CF Tuc - Kuerster & Dennerl 1993). Berdyugina & Tuominen (1998) have reported a tendency for binaries to exhibit persistent active longitudes, suggesting that flux tubes may emerge at preferred longitudes.

Contact binaries of W Uma type have also been successfully Doppler imaged. In contrast to the RS CVns, these stars show a preponderance of activity at high and low latitudes. Examples include AE Phe (Maceroni et al. 1994, Barnes et al. 2004), YY Eri A & B (Maceroni et al. 1994).

1.4 Latitude Distribution of Spots

As described in the previous section, Doppler images usually show large cool features that can be categorised into three latitude regions; polar spots, high latitude spots and low latitude spots. In contrast to this, sunspots only occur between ±35°. Another problem is that with surface imaging the quantifiable errors are associated with the data rather than the image. These two caveats have led to the validity of some of these features, in particular the existence of polar spots, to be questioned (Byrne 1992).

1.4.1 Spectral profile of polar spots

The spectroscopic signature of a polar spot is a line profile with a flat-bottomed core when compared with a synthetic rotation profile for a non-spotted star of the same $v \sin i$. This flattening has an almost time independent existence and is interpreted as being a long-lived and stable polar spot. Alternative explanations for the occurrence of the 'flattened' spectral line cores have been proposed by, among others, Byrne (1992) and Strassmeier et al. (1993). They suggest that the filling in of the spectral line cores could also be a result of chromospheric activity, e.g. plages.

Byrne (1996) also suggests that a theoretical model of a stellar atmosphere for a non rotating star may not replicate the atmosphere of the more active star. A particular case of this is the handling of the Na D doublet, where the line cores form above the chromospheric temperature minimum due to sufficiently high opacities (Andretta, Doyle & Byrne 1997). However when Unruh & Collier Cameron (1997) used only these lines to reconstruct a surface image, the results were showed that less high latitude structure was present in images formed from these lines than from other commonly used photospheric mapping lines. Bruls, Solanki & Schüssler (1998) investigated the effect of chromospheric lines on the spectral profile by using NLTE radiative transfer on 14 of the most commonly used lines for Doppler imaging. They concluded that it is unlikely for polar spots to be an artifact of Doppler imaging caused by the misinterpretation of chromospheric activity.

Hatzes et al. (1996) investigated the mean spectral line shape of the Ca I 6439 Å line in four RS CVn stars with different stellar inclination (HR 1099, El Eri, AR Lac, V471 Tau). The systems with low inclination and where the polar cap is visible, HR 1099 and El Eri, have a flatter bottom than the two high-inclination stars, AR Lac and V471 Tau. Hatzes et al. (1996) concluded that the presence of large cool polar spots provides a simple explanation for the observed inclination dependence of the flattening of the observed line profiles, that cannot be explained by gravity darkening, differential rotation, limb brightening or other unknown radiative transfer effects in the line flux calculation.

If polar spots were an artifact of the imaging process then it would be expected that all Doppler imaged stars should exhibit polar spots. However, Barnes & Collier Cameron (2001) have reconstructed images of two M dwarfs which do not exhibit polar spots, demonstrating that polar caps are not ubiquitous in all images reconstructed with a given tomography code.

1.4.2 Theoretical models

Additional support for the existence of polar spots is provided by theoretical models. Schüssler & Solanki (1992) concluded that the fast rotation of stars needed for Doppler imaging could be responsible for the high latitude spots due to a strong poleward deflection resulting from Coriolis forces. They also conclude that in this model the Sun ties neatly into a common picture of star spots being the emergence points of magnetic flux tubes rising from the bottom of the convection zone to the photosphere. The strong poleward deflection of magnetic flux tubes can also result in the presence of long-lived and stable polar spots, as has been observed on AB Dor from 1992 to 2002 (Chapter 3 and Donati et al. 2003).

An alternative model for the formation of polar caps is that proposed by Schrijver & Title (2001). In order to produce a polar spot, this flux must emerge a rate 30 times greater than observed on the Sun. In this model there is no discrimination on the grounds of spectral class for the formation of polar spots. The only trend is that polar spots are formed on rapidly rotating stars which are more active than the present Sun.

For the formation of high latitude spots DeLuca, Fan & Saar (1997) suggest that the emergence of flux at high latitudes may be as a result of flux tubes in the overshoot layer being distributed over a wide range of latitudes. They also suggest that low latitude features may constitute evidence of a distributed dynamo in rapid rotators, or that flows may result from flux being redistributed after emergence.

1.5 Evolution of Magnetic Activity

1.5.1 Lifetimes of surface features

A detailed review of star-spot lifetimes on single stars and RS CVn binaries is presented by Hussain (2002). Doppler imaging is better suited than photometry for studying the lifetimes of individual starspots, because it is more sensitive to subtle changes in the starspot distribution (Barnes et al. 2001). The longest lived feature on both binary systems (for example V711 Tau and El Eri) and on main-sequence stars (e.g. AB Dor) is the polar cap. Long term monitoring studies show that polar caps can persist for time scales of up to a decade. In contrast to this, Doppler imaging has shown that on single main-sequence stars, the lifetimes of mid to low latitude features are less than one month, as was observed for the rapidly rotating G-dwarf He 699 (Barnes et al. 2001).

Mid to low latitude features can persist at certain 'active longitudes', on RS CVn subgiants for similarly long periods. Berdyugina & Tuominen (1998) report active-longitude lifetimes of 4.5-8.8 years on the RS CVn system EI Eri and the single star HD 7275 respectively. The single giant star FK Com also shows 'active longitudes' with a lifetime of 3.3 years, resulting in a 'flip-flop' effect (Korhonen et al. 2001), where the strengths of the active longitudes vary with time. The impact of the 'flip-flop ' effect on dynamo theory is not yet clear, but it would indicate the existence of highly non axis-symmetric dynamo modes.

The Mount Wilson survey (which will be described in detail in the following section) has produced an analysis of densely sampled records that suggest the presence of differential rotation, and the existence of stable features for up to time periods of several years for stars of solar mass.

1.5.2 Activity cycles

Mount Wilson survey

Solar magnetic fields provide energy to the chromosphere, and to the outer layers of the solar atmosphere. Some of this energy is then dissipated by Ca II formed in the chromosphere, as previously described for the solar chromosphere. The Mount Wilson photometric survey, has been monitoring the Ca II H & K emission cores of ≈100 stars since 1966 to obtain an insight into the origin and nature of magnetic activity on solar-like stars (Wilson 1968, Baliunas et al. 1995). The stars that have been the targets of this programme show three broad types of variability in their chromospheric fluxes. Cyclic variability is found among lower main-sequence stars with a wide range of ages and masses. Younger stars of solar mass (less than 2 Gyr old) are more active but show irregular cycles or chaotic variability. A few solar type stars show no variability at all in their Ca II emission.

A simple evolutionary picture of surface magnetism can be derived from these results; for younger stars of solar mass, their rapid rotation results in a chaotic variability; for older stars ($> 2 \times 10^9$ years) of solar mass, the magnetic activity shows either a flat or a cyclic record. Looking at the Sun, it is evident that there are variations in its cycle, including periods, such as the Maunder minimum (c1640 to c1720) that would have shown non variable Ca II flux. The Maunder minimum has also been confirmed by cosmogeochemical records of radiocarbon ^{13}C (Cini Castagnoli 2000) and ^{10}Be (Beer, Raisbeck & Yiou 1991), as the solar activity modulates the energy spectrum of the primary galactic rays interacting with the Earth's atmosphere (cf. Eddy 1978). Usoskin et al. (2004) reconstructed the 11-year averaged sunspot number since 850 AD using measurements of ^{10}Be in ice cores from Antarctica and Greenland. The data show evidence for the century scale Gleissberg cycle and some shorter quasi-periodic cycles that have periods of the order of a millennium.

Photometric variations

The photometric variations of active stars have been observed by Oláh & Strassmeier (2002) and Hall & Lockwood (2004). With observations spanning up to 34 years, these data show evidence for a correlation between the rotational period and cycle length at least for the shortest cycle lengths. The calculated cycle length period for LQ Hya of 3.5 years, is in agreement with that as derived from dynamo theory (Kitchatinov, Jardine & Donati 2000).

Variations in photometric and Ca II H&K observations

Radick et al. (1998) examined 35 solar-type stars (F5 to K7, including the Sun) using contemporaneous photometric and chromospheric Ca II H&K observations. They showed that the long-term brightness and magnetic activity levels are correlated for old solar-like stars (as is in the case of the Sun), as they are faculae dominated. For the case of young solar-like stars (20% of the solar age) the inverse correlation is true as the stars are spot dominated. Radick et al. (1998) also showed that these stars show an anti-correlation between their short-term photometric and chromospheric emission variations.

1.6 Summary

In the first section of my thesis I apply the technique of Doppler imaging using least-squares deconvolution to the Alpha Persei G2 dwarf He 699, and the K0 dwarf AB Dor. For He 699 I reconstruct a surface image using spectroscopic and photometric observations. Comparing this data with previous results (also using spectroscopy and photometry) allows me to determine if there is a correlation between the presence of low latitude features and the amplitude of the photometric lightcurve. In Chapter 3, I reconstruct Doppler images of AB Dor using archival data from January 1992 and November 1993. I increase the signal-to-noise of these data sets by using least squares deconvolution. I also determine the differential rotation of AB Dor using the sheared image-method, and compare the results with those obtained using other methods.

The second section of my thesis is on the analysis of the eclipse-mapping of the inner face of the F9V primary of SV Cam. To determine the spot coverage fraction we were awarded 9 HST orbits, using spectrophotometry, over 3 primary eclipses. The signal-to-noise of the data is 5000. The lightcurve was completed using ground based photometric data.

In Chapter 4, I investigate the reliability of stellar images reconstructed via Max-Ent eclipse-mapping from high-precision light-curves. The lightcurves are generated from synthetic stellar images. These images are peppered with many small spots whose sizes were drawn from the log-normal sunspot size distributions published by Solanki (1999). I investigate the effect these spots have on the surface maps reconstructed from these lightcurves. I also show how the stellar temperature and radii are affected by the presence of spots.

In the literature the binary system parameters of SV Cam, i.e. radii, temperature and mass-ration, cover a large range of values. In Chapter 5, I determine the temperature for the primary and secondary stars of SV Cam using PHOENIX model atmospheres to fit the shape of the isolated primary spectra. I extend this result by determining the fractional coverage of spots in the non-eclipsed region of the primary star, and the size of a polar cap. These values are determined from the flux deficit between the best fitting model atmosphere, and the primary star's spectrum.

In Chapter 6, I apply these temperatures and fit for the radii of the binary system using a chi-squared landscape method in conjunction with MaxEnt eclipse mapping. I reconstruct a surface image, where the observed minus computed residuals show strong peaks at the contact points. I show that these peaks are reduced with the presence of a polar cap.

In the final chapter of my thesis, Chapter 7, I model the HST lightcurve using PHOENIX and ATLAS model atmospheres. The smoothness of the change in slope of the light-curve near the contact points is inconsistent with limb-darkening profiles derived from plane-parallel model atmospheres. I show that improved results are obtained using a full spherical model-atmosphere treatment which shows a sharp decrease in specific intensity very close to the stellar limb

Chapter 8 is a brief summary of the work and conclusions in this thesis.

CHAPTER 2

Latitude distribution of star-spots on He 699

This work is published in Jeffers, S. V., Barnes, J. R., Collier Cameron, A. 2002, MNRAS, 331, 66. Barnes assisted with the reduction and Max Ent imaging, while Collier Cameron gave advice and obtained the data.

2.1 Abstract

In this paper, the latitude distributions of star-spots are analysed on the rapidly rotating G dwarf He 699. An image was reconstructed from data taken with the William Herschel Telescope on La Palma on 2000 October 08. The predominant magnetic field structure is a decentred polar spot at high latitude, with smaller low latitude features also present. This result was verified by independent reconstructions using even numbered and odd numbered spectra. This work confirms and extends that of Barnes et al. (2001) and provides further evidence that there is a correlation between the presence of low latitude features and the amplitude of the photometric lightcurve. It is also a further step in the search for activity cycles on young G dwarfs.

2.2 Introduction

Star spots are the most easily observed form of magnetic activity on cool stars with an outer convective zone. Using modern indirect imaging techniques such as Doppler Imaging, combined with high precision optical photometry, it is possible to measure the lifetimes, latitude distributions, local rotation rates and surface brightness of stellar spots, and any changes in these properties as the stellar magnetic cycle progresses. The stars that display such activity are rapidly rotating, young, main-sequence stars. In general their rotational periods are less than one day, and half of the known population are G and K dwarfs in open clusters less than 100 Myr old. For example, in the Pleiades open cluster G and K dwarfs can exhibit up to 15% photometric modulation due to spots implying that up to 30% of the stellar surface is spotted (Stauffer et al. 1994).

The α Persei cluster is a young open cluster around its same named brightest member. The distance to α Per is 180-187pc (O'Dell & Collier Cameron 1993), and from main sequence fitting has an age of $\leq 50\,\mathrm{Myr}$ (Soderblom et al. 1993b). The distance given by the HIPPARCOS parallax is $181.5 \pm 22.1\,\mathrm{pc}$, while Dzervitis, Paupers & Vansevicius (1994) estimate its distance to be $180 \pm 3\,\mathrm{pc}$ by using main-sequence fitting to the photometry in the Vilnius system. As it is a young cluster, it has many late-type stars with high rotation rates typically of the order of 0.5d (Prosser, Stauffer & Kraft 1991). It has been of particular interest in the past for both photometric and spectroscopic observations, showing that the cluster has a large population of rapidly-rotating stars (v sin i = 90 $\mathrm{km\,s^{-1}}$) on its lower main sequence (Stauffer et al. 1985). This rapid rotation is present in α Per in early G to early K dwarfs.

It is only with the advent of multi-line profile cross-correlation techniques, such as least-squares deconvolution, that Doppler Imaging can be used to image such faint stars. Barnes et al. (1998) first applied least-squares deconvolution to the α Per G dwarfs He 699 and He 520. The image reconstructions from this analysis demonstrate that both stars have high latitude and/or polar spots and low latitude features.

In this paper the work of Barnes et al. (1998 & 2001) is extended by studying the starspot distribution on the α Per member He 699, four years after the original observations. He 699 is a rapidly rotating G dwarf with a rotation period of 0.49 days, an equatorial $v \sin i = 93.5\ \mathrm{km\,s^{-1}}$ and an inclination of 52.5^o (Barnes et al. 2001). In section 2, the principles of Doppler Imaging are outlined. In section 3 the spectroscopic and photometric data, that are the basis of the final images (section 4), are presented.

2.3 Observations

2.3.1 Combination of spectroscopy and photometry

To attain the best possible reconstruction of the stellar image it is necessary to combine both spectroscopic and photometric data sets. In general the photometric light curve of a single star can have one or two minima. The implications of these features for spot modelling have been described by Berdyugina & Tuominen (1998). The deepest minimum in the light curve is caused by the largest activity regions on the stellar surface, for example a large group of star spots. If a secondary minimum is present, it indicates that there is another smaller active region separated from the primary minimum by $\sim 180^o$ in longitude.

The main information that can be derived from photometric light curve is the passage of active regions at low latitudes across the visible hemisphere of the star. It is less sensitive to high latitude features that are higher than the inclination of the star as these features will be constantly in view. However, without Doppler imaged spectroscopic data it is impossible to reliably obtain any information on the structure, shape, area of latitude of the star spots. Photometric light curves do not contain high order Fourier components required to resolve such fine stellar features due to the effects of limb darkening (Collier Cameron & Hilditch 1997). Unruh & Collier Cameron (1997) noted that the spectroscopic reconstructions have poor latitude discrimination at latitudes $\leq 30^o$.

Spectroscopy

He 699 was observed on the night of 2000 October 8 with the Utrecht Echelle Spectrograph on the 4.2m William Herschel Telescope at the Roque de los Muchachos Observatory on La Palma. The detector was an array of two EEV CCDs, each with 2048 x 4096 13.5-μm pixels. The CCD was centred at the wavelength 5000 Å in order 27 of the 31.6 g mm^{-1} echelle grating. This enabled 61 orders to be extracted giving a wavelength coverage of 4026-7295 Å. The velocity increment per pixel at the detector is 1.6 $\mathrm{km\,s}^{-1}$, and the full width at half maximum (FWHM) intensity of the thorium-argon arc calibration spectra was 2.93 pixels, giving a resolving power $\mathrm{R} = 63300$.

Table 2.1 shows the record of observations. A total of 47 spectra of He 699 were obtained on this night, each of 600 s duration. The CCD was exposed to a maximum

Object	UT Start	UT End	Exposure Time(s)	No of Frames	Comments
HR 6847	20:03	20:08	300	1	G2V template
HD 1326	20:53	21:04	300	2	M1 template
HR 179	21:08	21:12	200	2	B2V template
He 699	22:21	06:32	600	47	

Table 2.1: Observations of He 699 on 2000 October 8

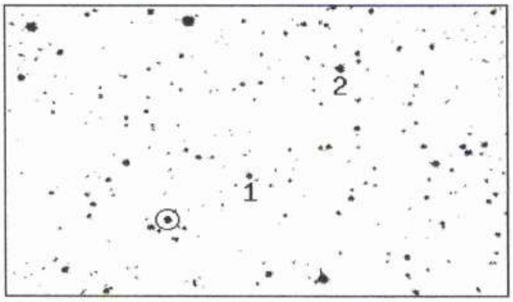

Figure 2.1: Finding chart showing the object and comparison star. Differential photometry was carried out with respect the star marked 1, while the star marked 2 served as a check. The reference stars are the same as those used in Barnes et al. (1998). The field size is approximately 17 x 11 arcmin^2.

count of 6000 ADU per pixel in the brightest parts of the image. The 600s exposure time compares favourably with the 53 s read-out time for the dual EEV CCD in terms of observing efficiency, i.e. the fraction of the time spent collecting photons is above 92%. Following extraction, the S:N in the continuum of the central order, 114, is 14 per pixel.

Photometry

The light curves were obtained in the V-band on the 0.93m James Gregory Telescope at St Andrews using a Wright Instruments CCD camera mounted at the Cassegrain focus. Observations were made on 2000 October 14, with 60s exposures. Light cloud was present towards the end of the night. The field of view of containing the target and reference stars is shown in Figure 2.1.

2.3.2 Data Reduction

The one-dimensional echelle spectra were extracted using the Starlink ECHOMOP (Mills 1994) and FIGARO reduction packages through the automated pipeline routine. Pixel-to-pixel variations were removed using flat-field exposures taken with an internal tungsten reference lamp. Orders were extracted using ECHOMOP's implementation of the extraction algorithm developed by Horne (1986). Wavelength calibration was carried out in ECHOMOP using thorium-argon arc frames, which were treated in a similar manner to the object and standard frames. Error statistics, based on the readout and photon noise, were propagated through the reduction process by ECHOMOP. Due to an integration time of 600s, the raw spectra contain many cosmic ray events. The cosmic ray rejection was efficiently implemented before extraction through the use of the FIGARO 'bclean' command, with the rejection threshold set to 10σ. The occurrence of hot pixels was deemed to be insignificant and those are accounted for in later stages of this analysis, i.e. in the process of deconvolution.

The automated extraction procedure then subtracted the bias from each frame, cropped each frame, determined the form and location of the stellar profile on each image relative to the trace, subtracted a linear fit to the scattered light background across the spatial profile and performed an optimal (profile and inverse variance weighted) extraction of the order across the full spatial extent of the object plus sky region. Sixty one orders were extracted from each exposure. The blue CCD recorded order number 140 at the blue end of the chip to order number 115 at the red end of the chip giving wavelength coverage of 402.6 nm to 501.2 nm with substantial wavelength overlap between orders. On the red chip orders 113 to 79 were recorded covering the wavelength range of 497.5 nm to 7295 nm also with good inter order overlap. Order 114 was positioned on the gap between the two CCDs, but there was no loss in wavelength coverage, due to the inter order overlap, which can be noted from the wavelength coverage of each chip.

The photometric data were reduced using JGTPHOT, a software package developed for use with the James Gregory Telescope at St Andrews (Bell, Hilditch & Edwin 1993). The resulting light curves are plotted as differential magnitude values with respect to the marked stars.

2.4 Image Reconstruction

Careful preparation of the observations is essential to attain the best possible results using Doppler Imaging. The steps that have been employed in this analysis are described in the subsequent text of this section.

2.4.1 Continuum Fitting

The general shape of the continuum in the echelle orders is generally well approximated by the careful selection of the number of spline knots. Following Collier Cameron & Unruh (1994), a continuum was fitted to the spectrum of a slowly rotating star of similar spectral type, in this analysis HR 6847. This approach has the advantage that the lines do not suffer from rotational broadening giving a greater number of continuum windows. For least-squares deconvolution the best possible fit to all orders is required. A spline fit with 11 knots was considered to be the best fit for the selected standard star.

2.4.2 The local specific intensity profiles

The spotted star is considered to comprise two temperatures, one for the cooler spotted stellar surface and one for the non-spotted photospheric part of the stellar surface. Two template stellar spectra were used; an M1 dwarf (HD 1326) with a photospheric temperature $\mathrm{T} = 3500\,\mathrm{K}$ for the spots, and a G2V dwarf (HR 6847) with $\mathrm{T} = 5750\,\mathrm{K}$ for the photosphere. These were deconvolved, using the method of least squares deconvolution, in the same manner using the same scaled continuum frame ensuring correct equivalent width.

2.4.3 Limb-darkening coefficient

The weighted mean wavelength (498.8 nm) was calculated from lines in the line list such that it was weighted with respect to both the line strength and the variance from the standard fit used in SPDECON. SPDECON is a deconvolution program which optimises the fit between a profile scaled by a synthetic model atmosphere list of line depths and an observed spectrum. The technique is a sophisticated cross-correlation, but with the sidelobes due to blending removed. Linear interpolation was used to obtain a value for the limb-darkening from Kurucz (1993) LTE models. The limb-darkening coefficients are 0.6336 and 0.6659 for the respective spot and photospheric temperatures of 3500 K and 5750 K. In this analysis 10 limb angles were used.

2.4.4 Least squares deconvolution

Since He 699 is too faint (m_v=11.5 and S:N=14) to apply the conventional technique of Doppler Imaging, it is necessary to use least-squares deconvolution. The least-squares deconvolution (LSD) method (Donati & Collier Cameron 1997) can be used to combine the information content of many weak and intermediate strength photospheric absorption lines in an optimal way, by computing average profiles from thousands of spectral lines simultaneously.

The least squares deconvolution process can be simplistically described as solving the vector equation

$$\frac{\delta\chi^2}{\delta z_k} = 0, \tag{2.1}$$

where,

$$\chi^2 = \sum_j \frac{(r_j - \sum \alpha_{jk} z_k)^2}{\sigma_j^2} \tag{2.2}$$

Here z_k represents the best fitting composite profile which, when convolved with a pattern of line positions and strengths encoded in the transformation matrix α, yields an optimal fit to the observed spectrum. r_j are the observations, and σ_j the errors on the observations. A more detailed mathematical explanation is given by Donati & Collier Cameron (1997) and Collier Cameron (2001).

A composite profile was deconvolved with a wider wavelength range than the stellar profile. This allows enough continuum in the least-squares profile to allow an empirical measurement of the S:N ratio in the adjacent continuum. The maximum improvement in the signal is proportional to the square root of the number of line images used. In this analysis 3550 lines were used. The gain in this analysis is calculated empirically to be approximately 44, representing a substantial improvement in the S:N.

Telluric (H_2O and O_2) lines are numerous in the red part of the spectrum and can affect some photospheric lines. In order to minimise the influence of the telluric lines on

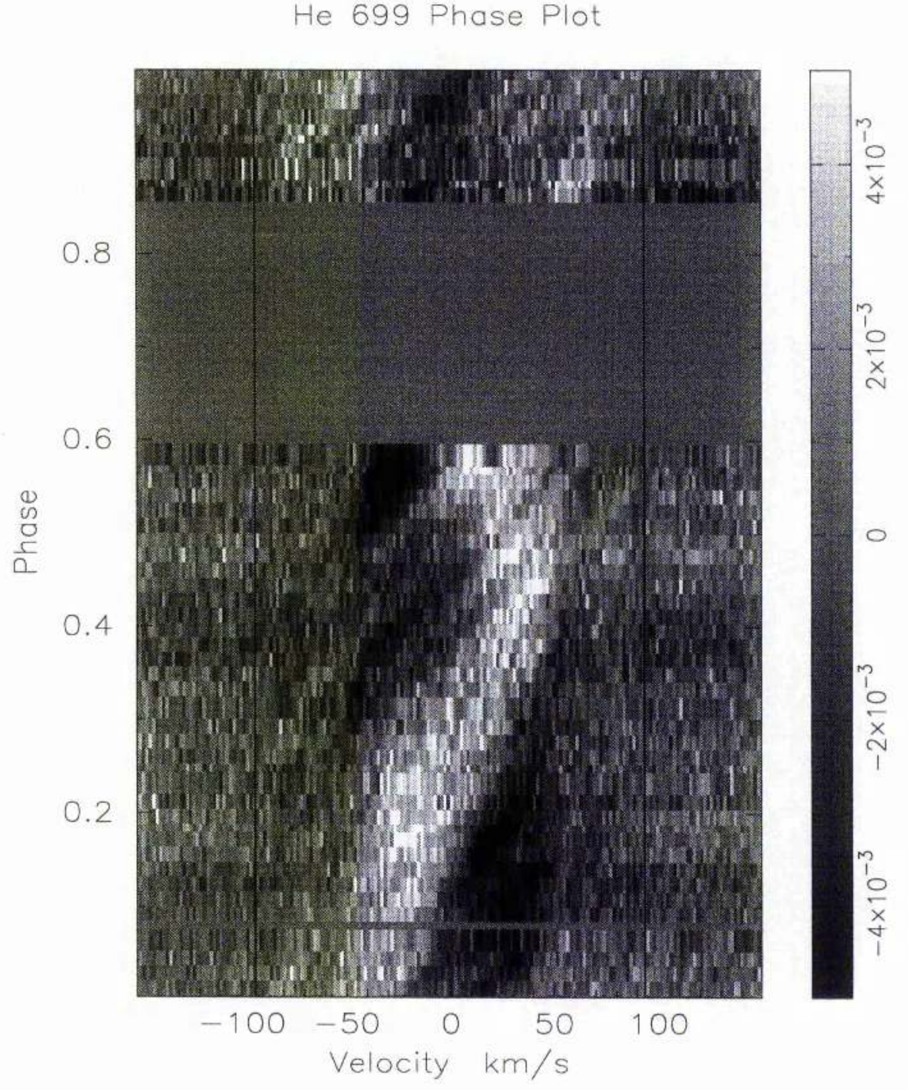

Figure 2.2: Time series spectra for He 699, with the mean profile subtracted. The vertical lines are at the v *sin* i of He 699, 93.5 $\mathrm{km\,s^{-1}}$.

the deconvolved profile, the line list was edited to mask out the worst affected wavelength ranges. Absorption lines close to and including NaI D were also removed, along with lines that were very close to the end of each order to minimise edge effects.

The time series spectra that were produced using least-squares deconvolution are shown in Figure 2.2. In the times series spectra it is possible to identify low latitude spots at phase 0.4 and a more slowly varying asymmetry in the line profile that is indicative of a large, off centred structure at high latitude. This high latitude structure crosses the disc centre at approximately phase 0.25 to 0.3, coinciding closely with the photometric minimum.

2.4.5 Final Image Reconstruction

Surface images of He 699 were recovered from the spectroscopic line profiles and photometric lightcurves using the DoTS surface imaging code (Collier Cameron 1997). DoTS is a maximum entropy code for the Doppler tomography of stellar surfaces that is based on the MEMSYS algorithm of Skilling & Bryan (1984). The stellar surface geometry model and integration scheme are described by Collier Cameron (1997).

In this analysis a restricted form of the entropy is used, combining the entropy of the spot image f_i and of the photospheric image $(1 - f_i)$:

$$S = \sum_i (-f_i \ln \frac{f_i}{m_i} - (1 - fi) \ln \frac{(1 - f_i)}{(1 - m_i)}). \tag{2.3}$$

Here m_i is the default value that a pixel will have when there are no other constraints imposed by the data. To construct the final image, the values for the spot and photospheric f_i are iteratively adjusted to maximise;

$$Q = S - \lambda\chi^2 \tag{2.4}$$

This is equivalent to maximising the entropy S over the surface of a hyper-ellipsoid, of constant χ^2, in image space. This is bounded by the constraint surface at some fixed value of χ^2. The Lagrange multiplier, λ, is set so that the final solution lies on a surface with $\chi^2 \simeq M$, M being the number of measurements in the data set. A more detailed explanation, of this and other methods, are given by Collier Cameron (2001).

As discussed in Collier Cameron & Unruh (1994), an incorrect treatment of fine

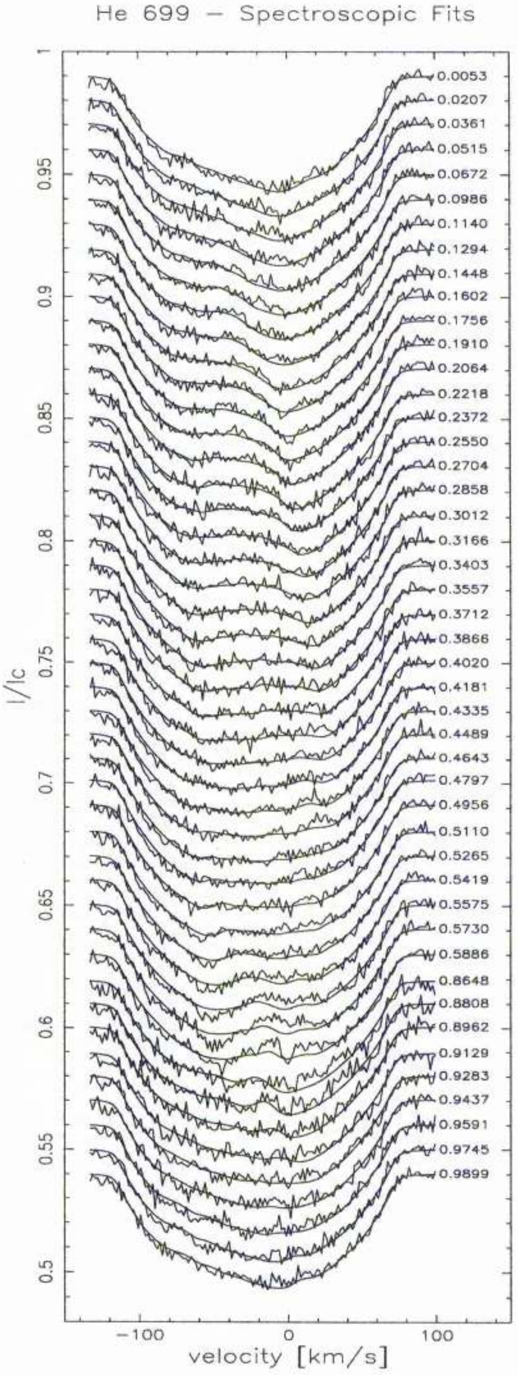

Figure 2.3: Spectroscopic data and maximum entropy fits for He 699, 2000 October 08

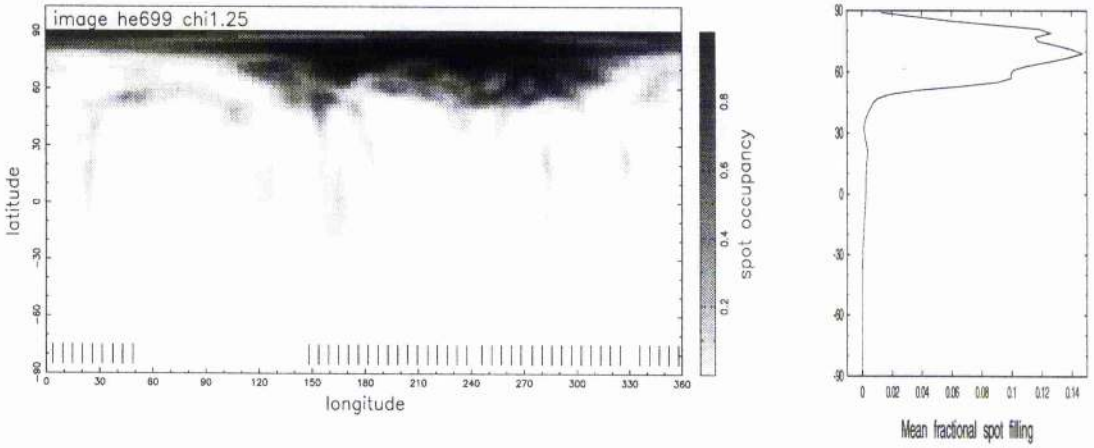

Figure 2.4: Maximum entropy image reconstructions for He 699, 2000 October 08. On the right, the mean fractional spot occupancy of the image as a function of latitude. Note: phase runs in reverse to longitude

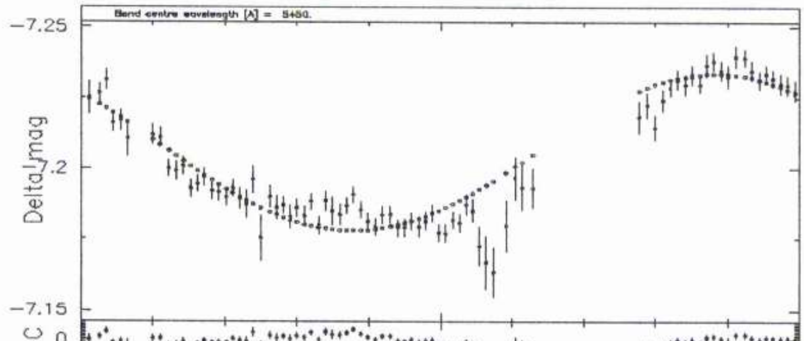

Figure 2.5: Photometric light curve and maximum entropy fit for He 699, 2000 October 08. The drop out of data points is a result of the presence of light cloud towards the end of the night.

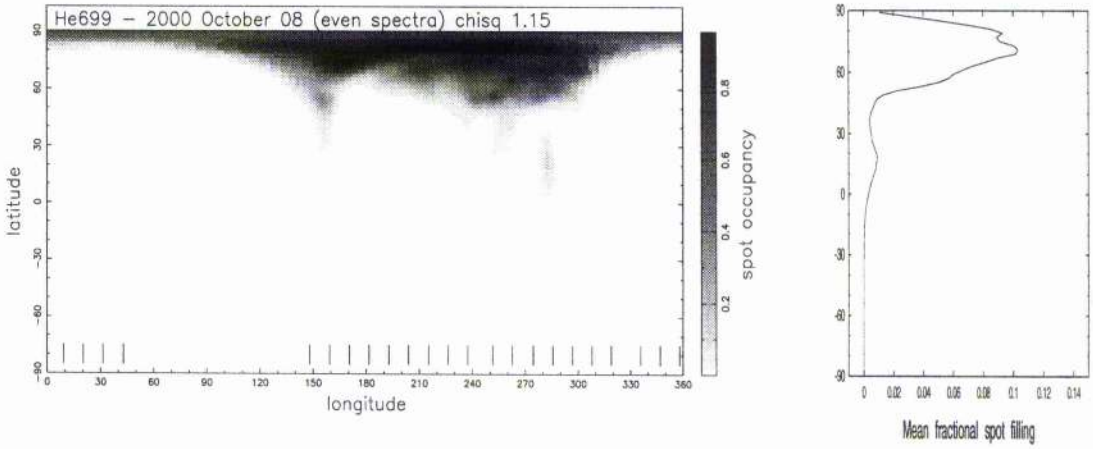

Figure 2.6: Maximum entropy image reconstructions for He 699, 2000 October 08 (even numbered spectra)

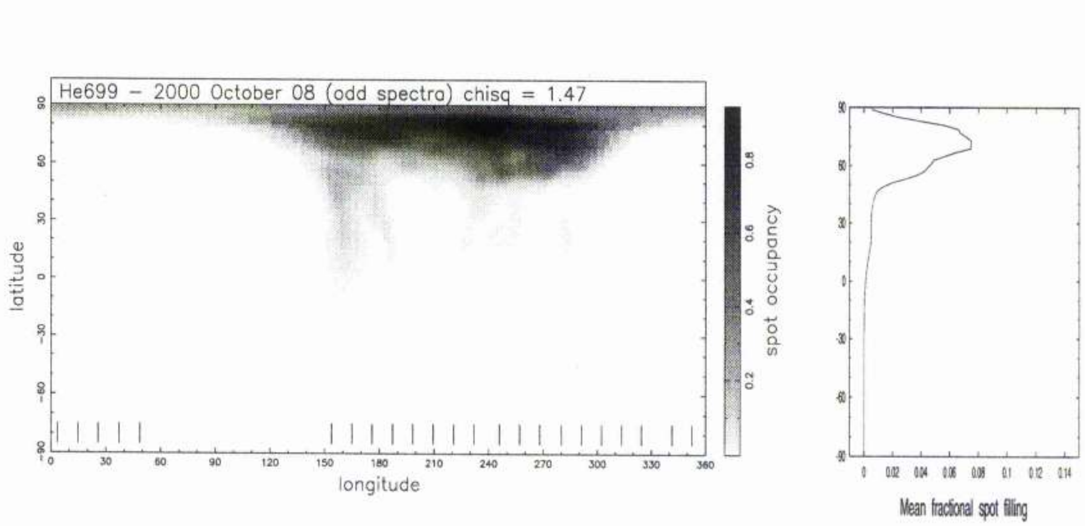

Figure 2.7: Maximum entropy image reconstructions for He 699, 2000 October 08 (odd numbered spectra)

tuning parameters can lead to spurious features. Reconstructions using DoTS were carried out by varying the values of the radial velocity and equivalent width, while keeping previously established values constant, i.e. $v \sin i$ and the rotation period (Barnes et al. 2001), to minimise the goodness of fit (as measured by χ^2) to the data. The parameters $v \sin i$ and equivalent width are correlated and so a grid containing various combinations of these parameters must be examined.

The resulting maximum entropy reconstructed images and the spectroscopic and photometric data sets are respectively plotted in Figures 2.4, 2.3, 2.5. The final image is a combination of the spectroscopic and photometric data sets. Independent reconstructions from the even numbered and the odd numbered spectra are plotted in Figures 2.6 and 2.7. The image reconstructions used a stellar surface grid with 90 latitude bands. Included in DoTS is a weighting factor, β to determine on which data set, spectroscopic or photospheric, the higher emphasis should be placed. This weighting factor can be set to between 0 and 1, where 0 implies 100% photometric data and 1 implies 100% spectroscopic data. The value for β for which the χ^2 of both data sets converges simultaneously was set to 0.97 with a $\chi^2 = 1.25$. As discussed in Unruh et al. (1995) and in Section 3.1 of this analysis the spectroscopic reconstructions have poor latitude discrimination within $\sim 30^o$ of the stellar equator. However, the converse is true for the photometric light curve, which is particularly sensitive to the structure that is present at low latitudes, although at much lower resolution. The value selected for β has the effect on He 699 of emphasising the low latitude structure. The final values for χ^2 are for the spectroscopy, χ^2_s=1.21, and for the photometry, χ^2_p=3.43.

2.5 Results and Discussion

A maximum entropy image reconstruction of the spot distribution on He 699 is shown in Figure 2.4. The mean fractional spot occupancy as a function of latitude is also plotted, clearly showing high latitudes as the main regions of spot coverage.

The lower latitude features are predominantly at a latitude $\leq 30^o$ and are elongated in latitude. The reasoning behind this vertical structure is that $\dot{v} \propto$ cos(latitude) is insensitive to small changes in latitude at the equator. The entropy criterion expresses the uncertainty in latitude by smearing the image north-south at low latitudes. The observed

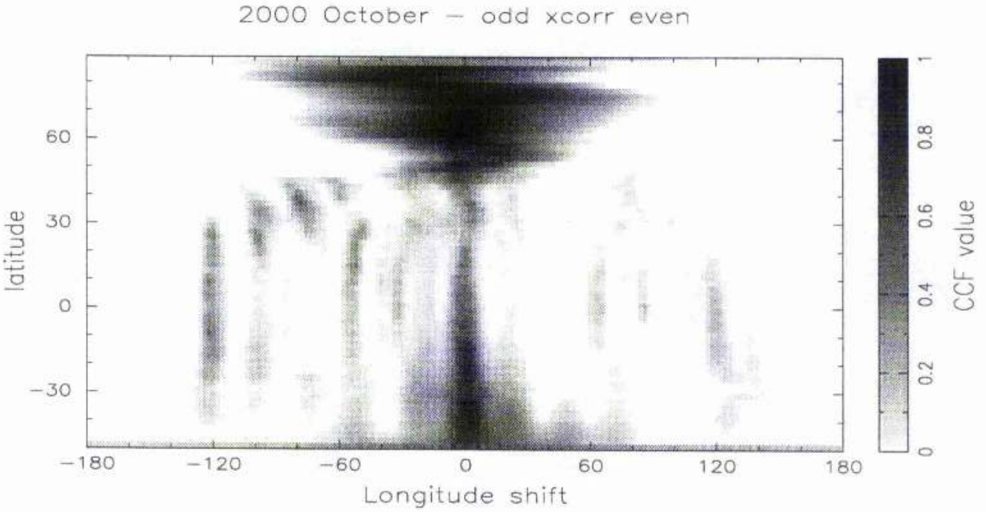

Figure 2.8: Image obtained from the cross correlation of the even and odd numbered spectra

presence of low latitude features is in disagreement with the convective overshoot dynamo models that predict the emergence of the magnetic field to be at intermediate to high latitudes (Granzer et al. 2000). There are also some mid latitude features present on the left hand side of the image at approximately a latitude of 60°. This long horizontal feature is considered to be an artifact of the imaging process, possibly introducing some smearing between two spots at either end of the distribution. The smearing occurs as a result of incomplete observations at this phase range.

The image obtained by the cross correlation of even and odd numbered data sets (Figures 2.6 and 2.7) is shown in Figure 2.8. The central vertical band in this plot signifies that there is correlation between the two data sets. The width of the cross correlation function peak gives the longitude resolution. The cross-correlation plot implies that there is more low latitude structure present on the surface of He 699 than is shown in Figure 2.4. Features that are not in the centre of the image are considered to be spurious features that occur during the incomplete phase coverage of the spectroscopic data.

The image that has been reconstructed in this analysis is in good agreement with previous studies on the same star by Barnes et al. (1998 & 2001). Barnes et al. (2001) reconstructed surface images using the same methods as in this analysis for data obtained in 1996 October and November. These images show a polar spot, and a decentred polar spot respectively for each of the observations, comparing well with the results of this analysis. An interesting point of comparison between the image reconstructions is present in the low latitude spot coverage. Whereas the 1996 data sets have significant low latitude features, there is little present in the current data set. This contrast is also present in the amplitude of the photometric light curve, with the amplitude of the 1996 data set being of a factor of two greater than the amplitude of the current data set. The significance of this further verifies that there is a correlation between the presence of low latitude features and the amplitude of the photometric lightcurve.

CHAPTER 3

Differential Rotation and Latitudinal Distribution of Spots on AB Dor in 1992 and 1993

3.1 Abstract

Surface brightness images for the young K0 dwarf AB Doradus, are reconstructed from archival data observed January 1992, and November 1993. The signal enhancement technique, Least-Squares Deconvolution (LSD) is used to boost the signal-to-noise of these data sets. These data sets show comparable spot features with those reconstructed without LSD, but with a significantly improved signal-to-noise ratio. The data sets do not cover a sufficient time base to allow large spot features to evolve, rendering it impossible to detect differential rotation using the sheared-image method.

3.2 Introduction

Solar-type stars exhibit signatures of magnetic activity that are assumed to be based on dynamo mechanisms operating in the star's outer convective zone. The detailed workings of the generation and amplification mechanisms of the stellar dynamos are still poorly understood as a result of the complex physics involved in theoretical models, and the lack of observational constraints. However, it is widely accepted that differential rotation and convection are essential ingredients of common theoretical amplification models (Parker 1955, Babcock 1965, Leighton 1964,1969)

Differential rotation results from the interplay of rotation and convection, which leads to a redistribution of heat and angular momentum inside the convection zone. The thermal and density profiles of convective motions produce a dependence of differential rotation on both stellar latitude and radius. It is a key process in the cyclic activity of the stellar dynamo being the process through which poloidal-toroidal field conversion occurs. Theoretical models of differential rotation calculated by Rüdiger & Küker (2002) suggest that for very fast rotation, a non-uniform energy leaves the stellar radiative core, that in turn heats the bottom the stellar convective zone non-uniformly (Stepien, Kiraga & Muthsam 1997). This then results in a meridional flow that flows towards the equator at the surface, accelerating the equatorial rotation.

To date there have been numerous observations of differential rotation on rapidly rotating cool stars, for example on AB Dor (Donati & Collier Cameron 1997), PZ Tel (Barnes, Collier Cameron & James 1999), LQ Lup (Donati et al. 2000), HR 1099 (Petit, Donati & Collier Cameron 2002 and Strassmeier & Bartus 2000). Several methods have been used to measure differential rotation. The methods of Bruning (1991) and Reiners & Schmitt (2002) use Fourier analysis to detect differential rotation. This method is however only applicable to stars that do not exhibit cool star spots as the spots themselves would cause a distortion in the absorption profile. Other methods use surface features (i.e. spots) as tracers to ascertain how their rotation periods are dependant on latitude. Examples include the cross-correlation method used by Donati & Collier Cameron (1997) which resulted in the first reliable differential rotation measurement for a star (AB Dor) other than the Sun. This method measures the amount of rotational shear as a function of latitude by cross-correlating belts of equal latitude. A more sophisticated method, that has been developed by Donati, Collier Cameron & Petit (2003) and is the method used in this work, is the sheared-image method where the differential rotation model in incorporated into the image reconstruction process, where the rotation rate is allowed to vary smoothly with latitude on an image grid.

The temporal evolution of differential rotation can be determined by measurements over several epochs. Collier Cameron & Donati (2002) measured the first temporal evolution of differential rotation, by using the spot-tracking method. This method uses matched-filter analysis to track individual spot features in the trailed spectrograms. The temporal evolution of AB Dor differential rotation has also been confirmed by Donati, Collier Cameron & Petit (2003), through the use of the sheared-image method, though not for the same epochs as Collier Cameron & Donati (2002).

In this paper we shall extend the epochs for which differential rotation has been measured using the sheared-image method, by reprocessing archival AB Dor data for epochs January 1992 and November 1993. This is the first time that images have been reconstructed from composite profiles computed from these data sets using LSD. In Section 2 we describe the observations and the method of preprocessing the data, in Section 3 we present a spot map for each epoch of observations, and in Section 4 we measure the differential rotation for each epoch.

3.3 Observations

3.3.1 Instrument set-up

The data that comprises this work are spectroscopic observations collected at the 3.9 m Anglo-Australian Telescope. These observations, including observing logs and observing procedures, have previously been published in Collier Cameron & Unruh (1994) and Unruh, Collier Cameron & Cutispoto (1995), and shall be briefly summarised here. The slit width was 1.2 arcsec and the resolution was ≈51000.

1992 January–AAT: Observations spanned 18-20 January 1992 with the UCL échelle spectrograph. The detector was a 1024 × 1024 element Thomson CCD, centred at 570.8nm in order 99 of the 31.6 line mm^{-1} grating. For most of this observing run, the seeing was 1.4 arcsec.

1993 November–AAT: Observations spanned 23-25 November 1993 at the AAT with the UCL échelle spectrograph. The detector was a 1024 × 1024 Tektronix CCD, centred at wavelength 574.6nm in order 99 of the 31.6 line mm^{-1} grating.

3.3.2 Data reduction

All frames were reprocessed with ESpRIT, a dedicated package for the optimal extraction of echelle spectroscopic observations. A detailed description of this package is given by Donati et al. (2000).

3.3.3 Least-Squares Deconvolution

LSD is a method for combining the rotation profiles of thousands of spectral lines on an optimally weighted fashion Donati et al. (2000). It uses a weighted least squares algorithm to compute the line broadening profile which, when convolved with the known pattern of photospheric absorption lines in a stellar spectrum, optimizes the chi-squared fit to the data. It can be shown that the enhancement in signal to noise is equivalent to either an optimally-weighted stacking of the profiles, or to cross-correlation with the line pattern, scaling as the square root of the number of lines used. It has the advantage, however, that sidelobes caused by blends are automatically eliminated from the composite profile, giving a clean profile surrounded by flat continuum.

3.3.4 Telluric line alignment

Telluric lines are used to correct for small shifts in the spectrograph during the night i.e. from dewar refill and the thermal and mechanical relaxation of spectrograph's components. The procedure is described by Donati, Collier Cameron & Petit (2003). The composite profile of telluric absorption lines in each stellar spectrum was computed using LSD, with a line mask consisting of the wavelengths and relative strengths of known telluric features (mainly of water) in the spectral region used. The instrumental velocity of the composite telluric profile was measured and used to define the zero-point of the velocity scale for the deconvolved stellar rotation profiles, before applying heliocentric velocity corrections.

3.4 Surface Image Reconstruction

The stellar surface imaging code which is used to reconstruct the surface images in this work is the maximum entropy code of Brown et al. (1991) and Donati & Brown (1997). The brightness model that is incorporated in this code is the 'spot occupancy' model of Collier Cameron (1992), as described in the previous chapter. Each point on the stellar surface is quantified by a quantity f that describes the local fraction of the stellar surface occupied by spots. The range of spot occupancy is from 0, where there are no spots present, to 1, where there is maximum spottedness.

The imaging parameters that are used in this work for AB Dor are stellar axial

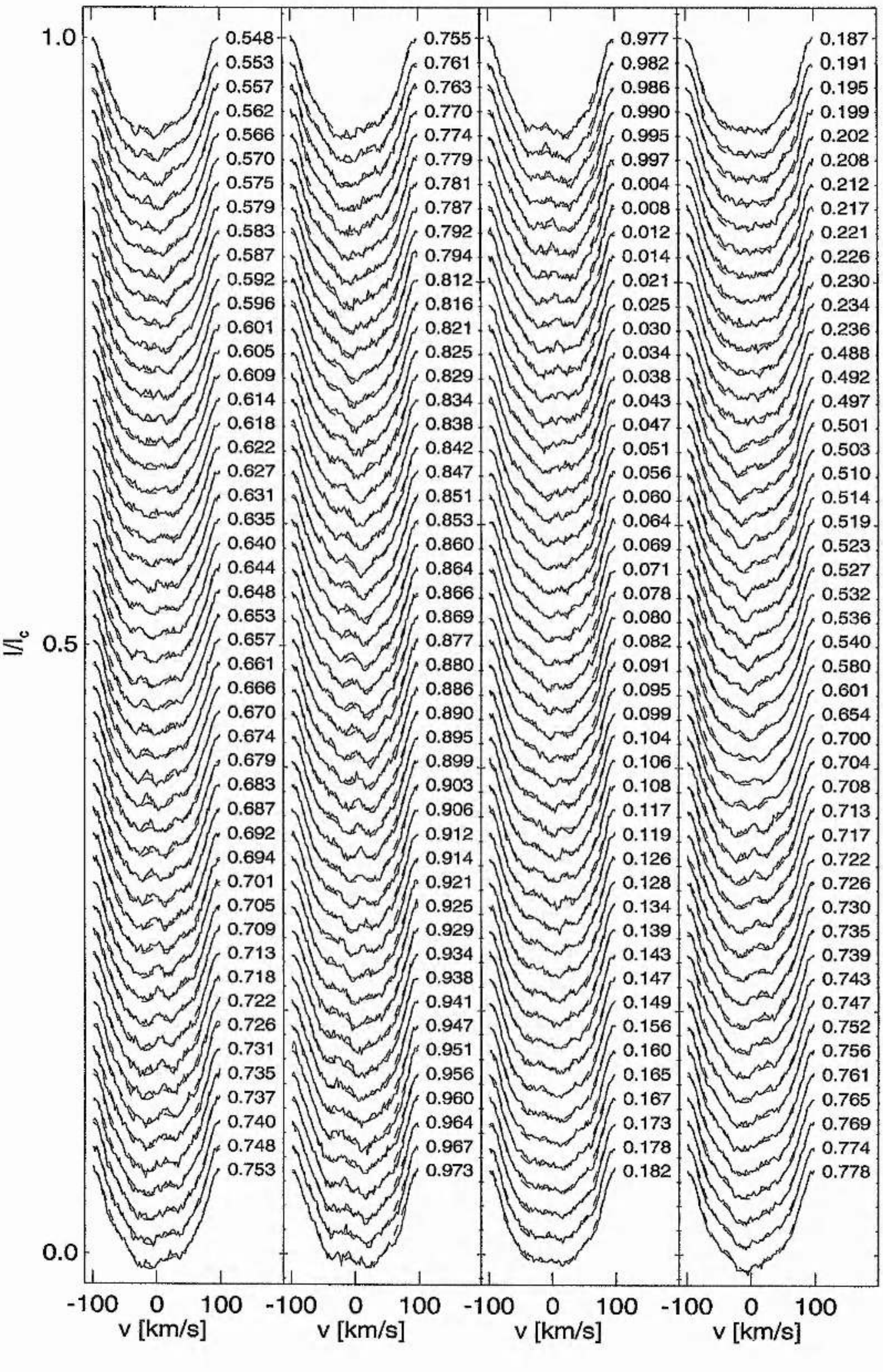

Figure 3.1: Spectroscopic data and MaxEnt fits for January 1992, part I

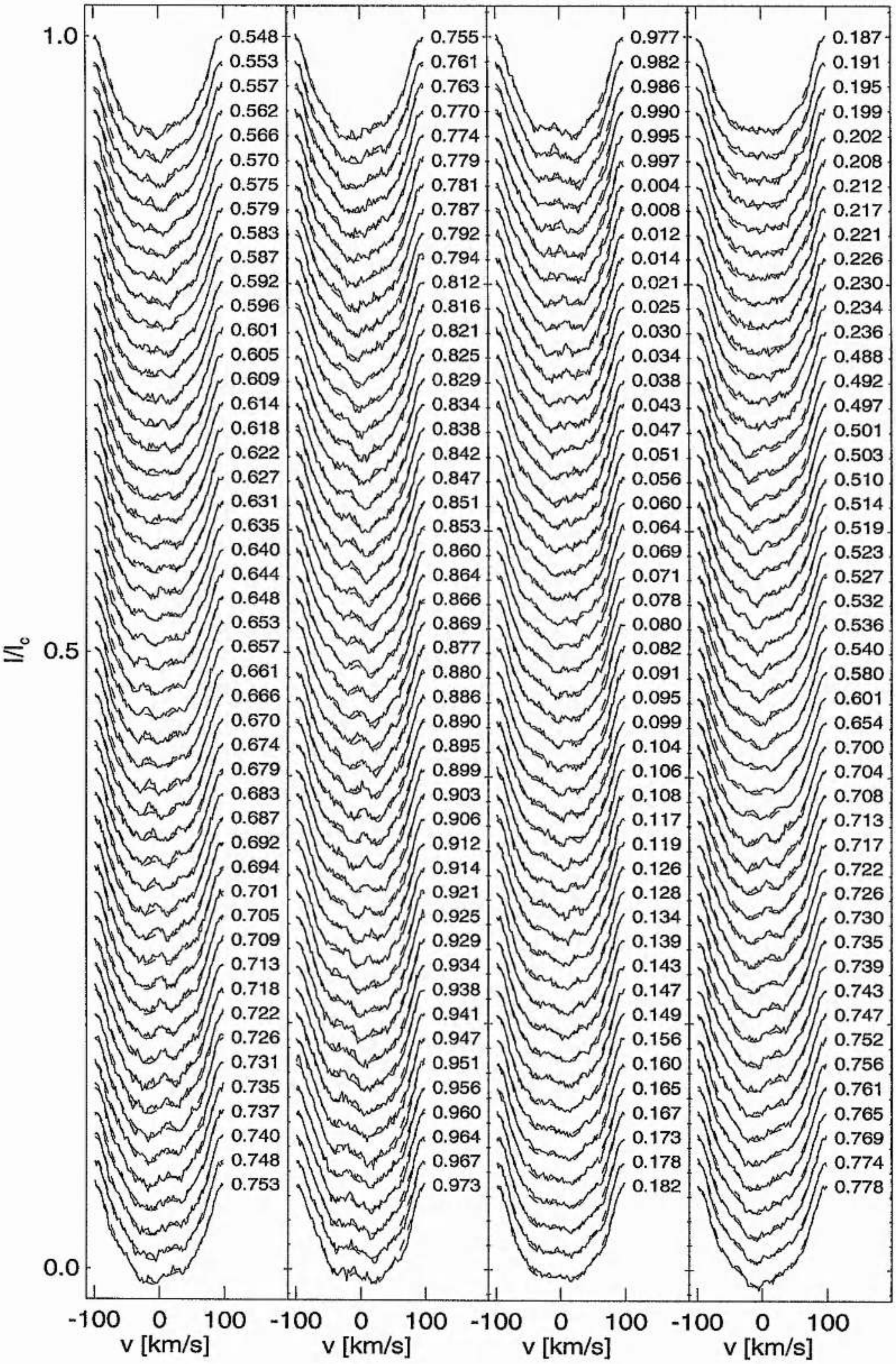

Figure 3.2: Spectroscopic data and MaxEnt fits for January 1992, part II

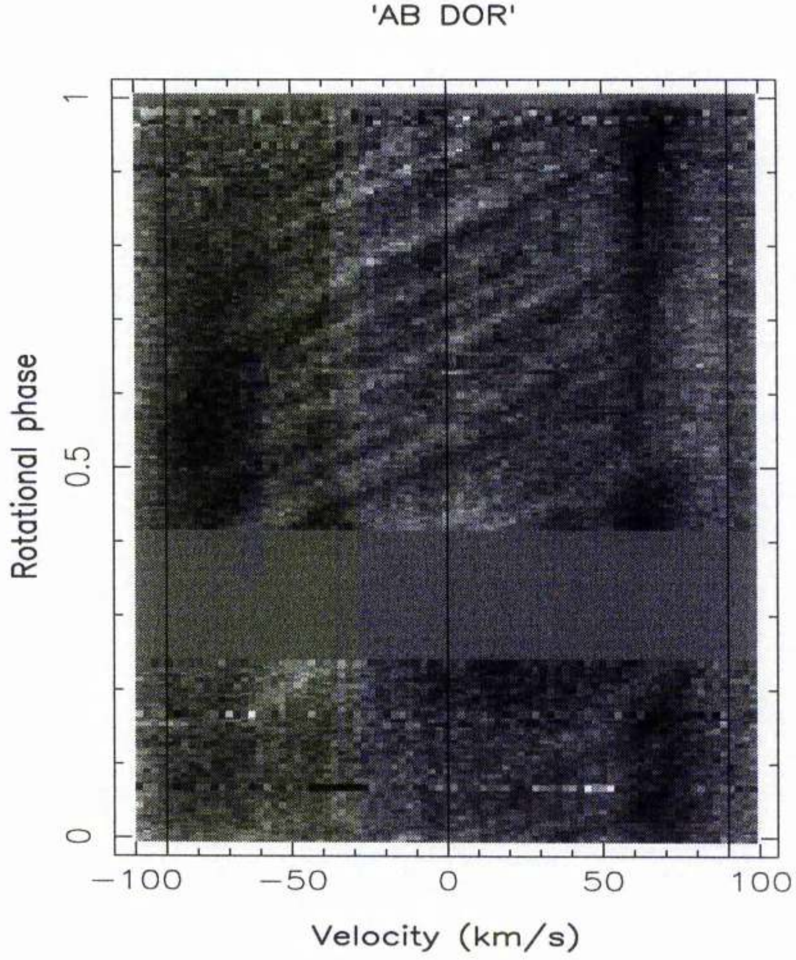

Figure 3.3: Dynamic spectrum of the residuals for January 1992.

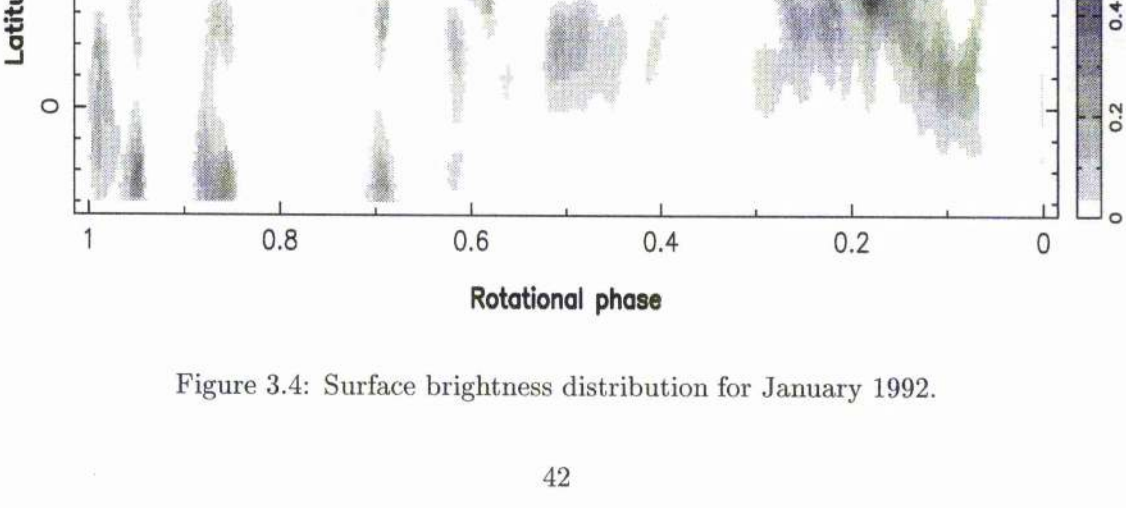

Figure 3.4: Surface brightness distribution for January 1992.

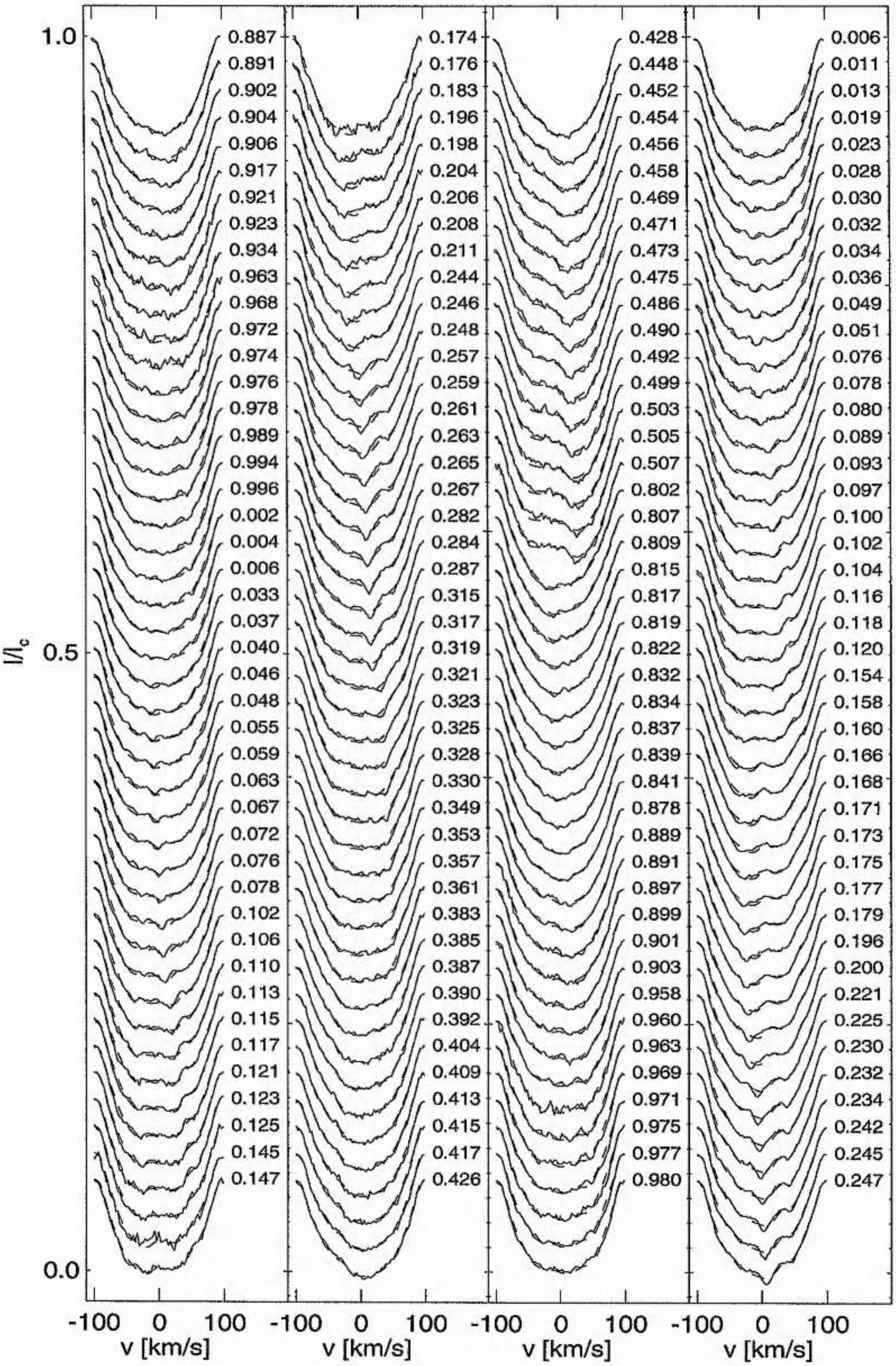

Figure 3.5: Spectroscopic data and MaxEnt fits for November 1993 part I

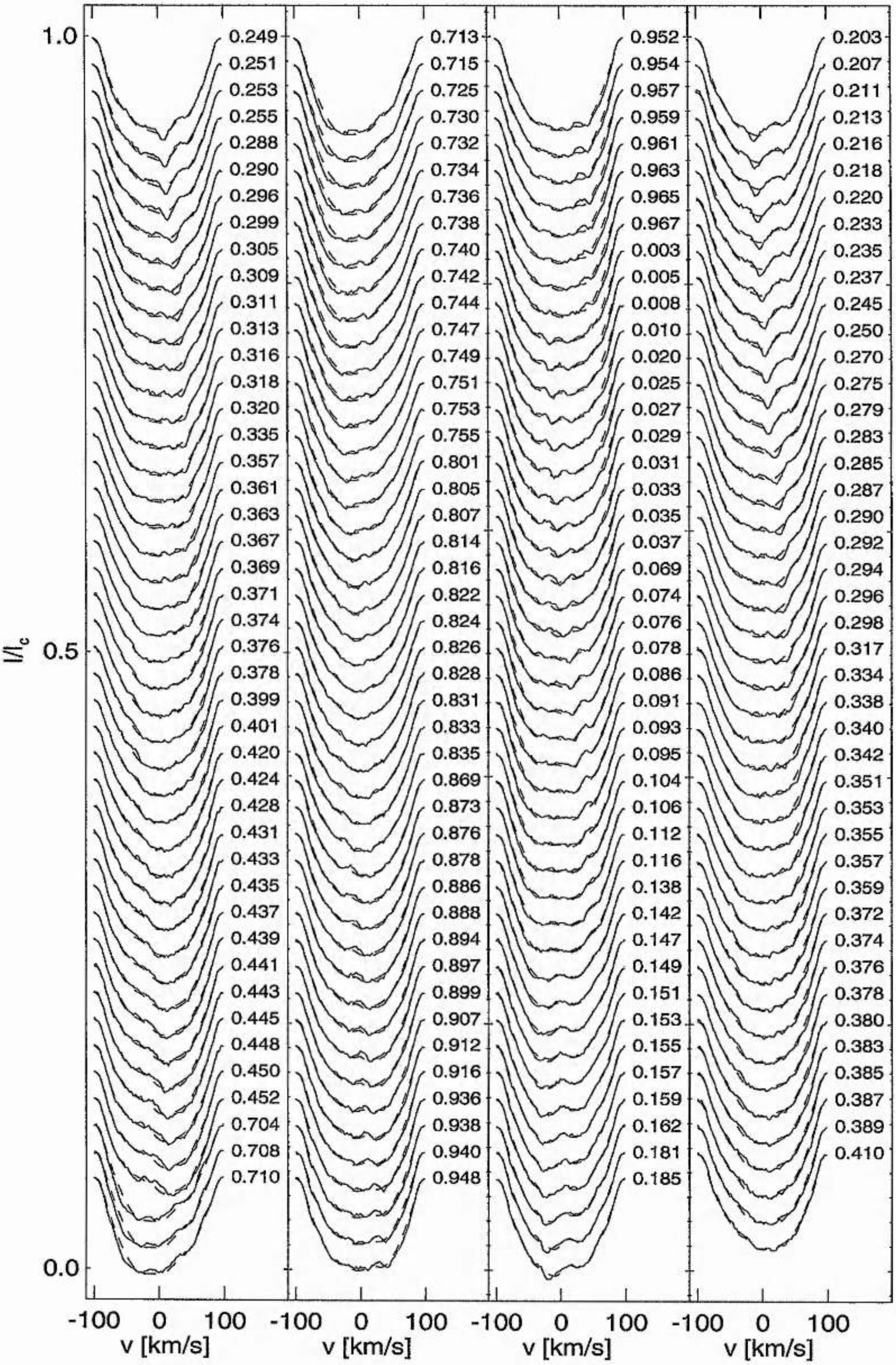

Figure 3.6: Spectroscopic data and MaxEnt fits for November 1993 part II

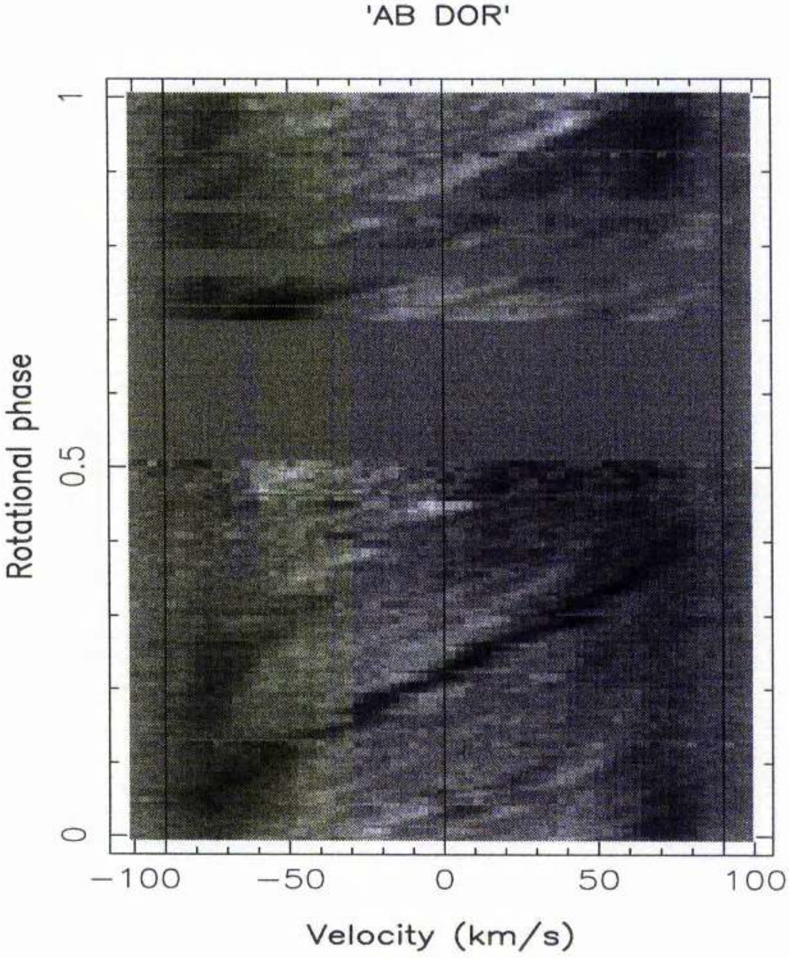

Figure 3.7: Dynamic spectrum of the residuals for November 1993.

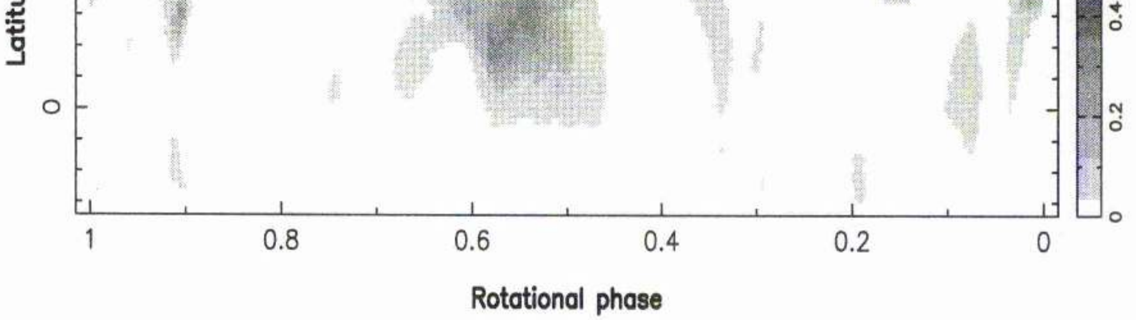

Figure 3.8: Surface brightness distribution for November 1993

inclination, $i = 60^o$ and the projected equatorial rotation velocity, $v \sin i = 89\,\mathrm{km\,s^{-1}}$ (Donati et al. 2003). The heliocentric radial velocity is $31.7\,\mathrm{km\,s^{-1}}$ for January 1992, and $31.6\,\mathrm{km\,s^{-1}}$ for November 1993. The spectroscopic fits and resulting surface brightness images are shown in Figures 3.1, 3.2 and 3.4 for 1992, and Figures 3.5 and 3.6 and 3.5 for 1993. The dynamic spectrum of the residuals is shown in Figure 3.3 and 3.7 respectively for the 1992 and 1993 data sets.

3.5 Differential Rotation

We used the sheared-image method of Donati et al. (2003) to measure the differential rotation of AB Dor at both epochs. The image reconstruction process incorporates a model of the stellar surface whose rotation rate Ω depends on latitude according to the simplified solar-like differential rotation law:

$$\Omega(\theta) = \Omega_{eq} \; - \; \Delta\Omega cos^2\theta \tag{3.1}$$

We performed a large set of of image reconstructions, using a two-dimensional grid of values for the parameters Ω_{eq},$\Delta\Omega$. For each set of model parameters, the image reconstruction was driven until it reached a fixed value of chi-squared. The spot filling factors of the resulting images form a "landscape" on this grid, and should show a global minimum whose location yields the optimal differential rotation parameters. The optimal value of differential rotation is then the model that corresponds to the minimum in the spot-area landscape, as models with the wrong shear give poor fits to the data as it is necessary to add more structure to the images to compensate for this. Using this it is then possible to obtain an estimate of the error bars on the differential rotation parameters (Petit, Donati & Collier Cameron 2002).

The validity of this method has been confirmed by Petit, Donati & Collier Cameron (2002) through extensive sets of simulations, provided that the spectroscopic data samples the variability of the surface distribution of cool spots. It is ideal for differential rotation measurements to have a time gap of several rotation periods between observations to allow surface features to evolve. AB Dor is a good candidate as its rotation period is short

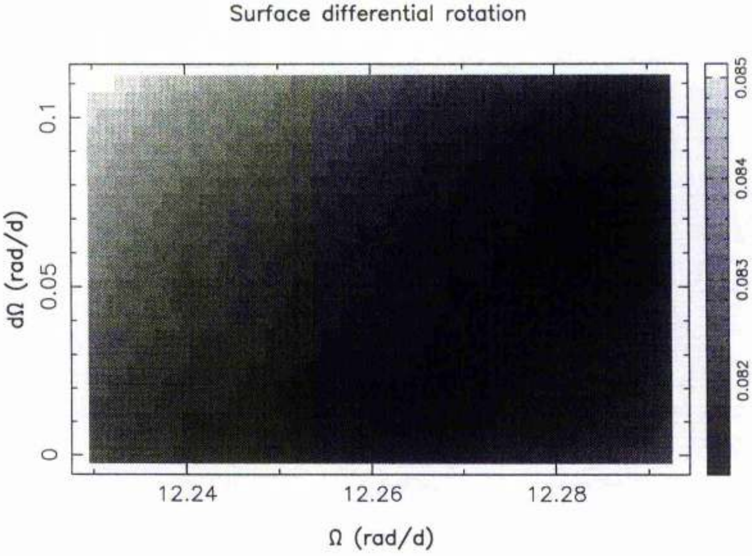

Figure 3.9: χ^2 landscape of differential rotation for January 1992

enough (0.51749d) that up to two thirds of the stellar surface may be observed in a single night.

3.6 Discussion and Conclusion

Both surface brightness images show a strong polar cap. The January 1992 surface image shows significantly more intermediate to low latitude spot features than the November 1993 image, where most of the spot coverage is confined to high latitudes.

The reconstructed surface-brightness image for January 1992 (Figure 3.4) compares well with previous images processed without LSD (Collier Cameron & Unruh 1994) using the Ca I 643.9nm and Ca 671.8 nm photospheric lines. It is not possible to compare exact features, but to a first approximation they contain similar spot features and groupings of spots. Examples of this are the spot grouping at phase 0.1, the gap in low latitude features at phase 0.8, and the spot features at phase 1.0. Collier Cameron & Unruh (1994) also reconstructed a surface brightness image using the photospheric line Fe I 666.3nm. The spot features and groupings in this image don't show the same degree of correlation to the image reconstructed in this work.

The images for November 1993 were previously reconstructed using the the combined lines of Ca I 643.9 nm, Fe I 666.3 nm and Ca I 671.8 nm. As there are fewer intermediate

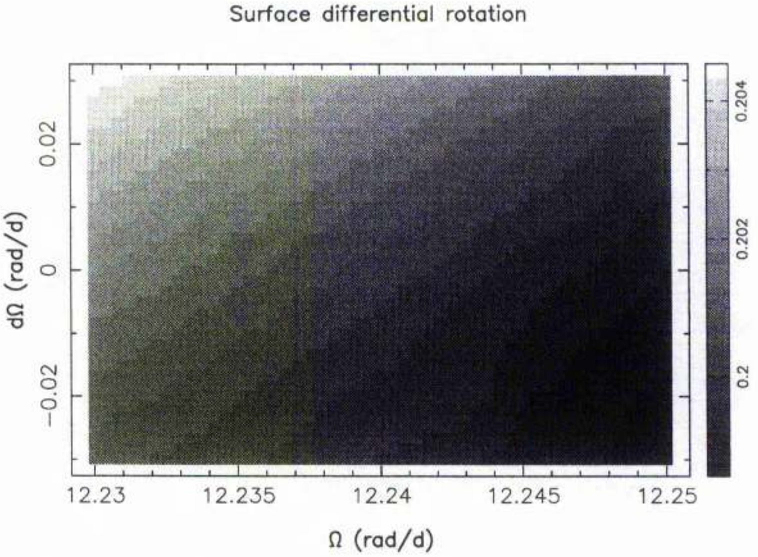

Figure 3.10: χ^2 landscape of differential rotation for November 1993

and low latitude spot features in the work of Unruh, Collier Cameron & Cutispoto (1995) than in this work Figure 3.8, a comparison of the results is not as straight forward as for the 1992 data set. However, there are comparable spot features at phases 0.17 and 0, and a comparable spot grouping at phase 0.55, though as indicated by the tick marks above the plot, this is a region where there is no phase coverage.

It was not possible to detect differential rotation using the sheared-image method for either data set. In January 1992, Figure 3.9, shows a clear χ^2 valley with no minimum. In November 1993, one could be misled into thinking that the χ^2 minimum lies to the bottom right of the plot, implying that AB Dor has anti-solar differential rotation.

The inability to track differential rotation could result from insufficient phase coverage, and insufficient time between observations for the spots to evolve. However, Collier Cameron & Donati (2002) detected differential rotation for both of these data sets using matched-filter analysis. Matched-filter analysis has the ability to track individual spots in the dynamical spectrum as they cross AB Dor's rotation profile. This sensitivity to smaller spots could explain the difference in the results, if small spots rotate at a systematically different rate from the larger spots to which the sheared-image method is sensitive.

We must consider the possibility that the MaxEnt image reconstruction method itself suppresses fine structure in the images to too great an extent. If so, the detailed spot features in the data that delineate the differential rotation pattern may not be fitted properly. More investigation is needed, by applying the spot-tracking method to data sets where differential rotation has been determined using the sheared-image method. It would then be possible to see if there is a discrepancy between the two methods. Also further testing using synthetic distributions of spots should be carried out to determine the reliability of the two methods.

CHAPTER 4

The Deceptive Presence of ‘Active Longitudes’ and ‘Two-spots’ on Binary Stars

This chapter has been submitted to MNRAS as a single author letter without the section on the noneclipsing binary system.

4.1 Abstract

In this paper, size distributions of different degrees of spottedness, that are extrapolated from the case of the Sun, are applied to the eclipsing binary SV Cam. These spot distributions pepper the primary's surface with spots, many of which are below the resolution capabilities of eclipse mapping and Doppler imaging techniques. The lightcurves resulting from these modelled distributions are used to determine the limitations of image reconstruction from photometric data. Surface brightness distributions reconstructed from these lightcurves show distinctive spots on the primary star at its quadrature points. It is concluded that while the concept of ‘active longitudes’ and the ‘two spot’ model can be used to fit the lightcurve, the spot distribution is incorrectly modelled if the surface of the star is peppered with small unresolvable spots.

4.2 Introduction

Doppler imaging has shown that rapidly rotating RS CVn binary systems, such as SV Cam (F9 V + K4 V, P_{rot}=0.59 d) frequently show spots at high and polar latitudes. Theoretical models of the formation of polar spots assume that magnetic flux from decaying active

Solar:	min	max					
Set	1	2	3	4	5	6	7
		0.3%	1.8%	6.1%	18%	48%	100%
σ_A	3.8	5.0	6.8	9.2	12.2	15.8	20.0
$(\mathrm{dN/dA})_{max}$	5	25	65	125	205	305	425
A_{tot}	80	760	4000	15170	46410	121110	250000
$A_{spot,tot}$	320	3000	16000	61000	186000	484000	10^6
A_{tot}/N_{tot}	5.0	7.4	11.6	18.0	27.3	39.7	55.7
A_{DI}/A_{tot}	0.0002	0.003	0.02	0.06	0.14	0.23	0.33
N_{tot}	16	103	345	843	1700	3051	4488
A_{max} ($A_\odot$)	200	400	1000	3000	6000	10000	10000

Table 4.1: Tabulation of the input parameters to the log-normal size distribution of star spots, equation 4.1. The parameters derived by Bogdan et al. (1988) for the Sun are data sets 1&2, and those calculated by Solanki (1999) for active stars are data sets 3-7.

regions is swept towards the poles by meridional flows (Schrijver & Title 2001). They found that in order to produce polar spots bipolar active regions have to emerge at a rate approximately 30 times faster than in the case of the Sun, implying that the photospheres of active stars should be peppered with a large number of small spots.

Jeffers et al. (2004c) (Chapter 6) used spectrophotometric data from STIS onboard the Hubble Space Telescope to eclipse map the inner face of the primary of SV Cam. To determine the temperature of the primary star, Jeffers et al. (2004a) (Chapter 5) fitted PHOENIX model atmospheres to the spectral energy distribution of eclipsed flux. The best fitting PHOENIX model atmosphere shows 30% higher flux than the surface flux in the eclipsed low-latitude region of the primary star. This flux deficit can only be accounted for if approximately 30% of the primary's surface is peppered with dark spots too small to be resolved through eclipse-mapping techniques.

In this chapter I apply the extrapolated solar spot size distribution of Solanki (1999) to a hypothetically immaculate primary star of SV Cam. We determine how different degrees of spot coverage influence the shape of the binary system's lightcurve, and how accurately these lightcurves are reconstructed into surface brightness distributions using the Maximum Entropy eclipse mapping technique.

4.3 Modelled Data

4.3.1 Size distribution of spots on active stars

The variable nature of the spot coverage of active stars makes the quantification of their spot size distribution an intriguing problem. In the case of the Sun, the spot size distribution has been determined by Bogdan et al. (1988) from direct observations taken from the Mount Wilson white-light plate collection covering the period 1917-1982. When plotted on a log-log scale the size distribution of sunspots is parabolic, implying a two-parameter log-normal distribution, which cannot be represented by a single parameter distribution such as a power law. Following Bogdan et al. (1988) the number of sunspots, N, as a function of the solar surface area, A, is equated as,

$$\frac{dN}{dA} = \left(\frac{dN}{dA}\right)_{max} \exp\left(-\frac{(\ln A - \ln\langle A\rangle)^2}{2\ln\sigma_A}\right) \tag{4.1}$$

where the constants ⟨A⟩ and σ_A are the mean and geometric standard deviation of the log-normal distribution, and $\left(\frac{dN}{dA}\right)_{max}$ the maximum value reached by the distribution. For the case of the Sun, these values are tabulated in Table 4.1 where set 1 is for an inactive Sun and set 2 is for an active Sun.

Solanki (1999) has extended the solar spot size distribution of Bogdan et al. (1988) to active stars by analysing how the observable parameters of the log normal distribution, $(\mathrm{dN/dA})_{max}$, ⟨A⟩, and σ_A, change with increasing magnetic activity. The size distributions cover a range of degrees of spottedness, from the one at solar minimum to a completely spotted star. The penumbral diameter is included in the spot area, in the umbral to penumbral area ratio of 1:3 which is assumed to be independent of spot size. In all cases the minimum spot area is $1.5\times10^{-6}\mathrm{A}_\odot$, where $\mathrm{A}_\odot$ is the surface area of the visible solar hemisphere. The input parameters for the log-normal distributions of Bogdan et al. (1988) and Solanki (1999) are tabulated in Table 4.1: sets 1 and 2 are for the inactive and active Sun, and sets 3 to 7 correspond to active stars with a spot coverage of 1.8%, 6.1%, 18%, 48% and 100% of their surface.

4.3.2 Generation of randomly distributed spots

The binary eclipse mapping code DoTS (Collier Cameron 1997) was used to synthesise spot maps which follow a log-normal size distributions on the surface of an immaculate SV Cam's primary (primary: R_1=1.24$R_\odot$, T_{eff}=6038 K, secondary: R_2=0.79$R_\odot$, T_{eff}=4804 K) to incorporate the surface geometry and radial velocity variations of tidally distorted close binary stars. The input parameters to DoTS for modelling spots are;

(i) **longitude:** randomly distributed between 0° & 360°

(ii) **latitude:** randomly distributed following $\frac{1}{2}(\sin\theta + 1)$ over the range $-\frac{\pi}{2} < \theta < \frac{\pi}{2}$ to eliminate an artificial concentration of spots at the pole

(iii) **spot radius:** computed using the previously described log-normal distribution as tabulated in Table 4.1

(iv) **spot brightness & spot sharpness:** distributed values subject to imposed limits to achieve the desired umbral to penumbral ratio.

4.3.3 Spot distributions

The spot distributions resulting from the size distributions given in Table 4.1 are shown on the left hand side of Figure 4.1 (sets 1 to 3) and in Figure 4.2 (sets 4 to 7). The degree of spottedness increases from the set at solar minimum (top of Figure 4.1) to the set with 100% spot coverage (bottom of Figure 4.2). These modelled spot distributions were used to generate a synthetic lightcurve, comprising 500 points with uniform sampling and with random Gaussian noise (0.0004) added to match the photometric precision of our HST data. The central lightcurve wavelength, 4670Å, was also chosen to match that of our HST data.

4.4 Surface Brightness Image Reconstruction

The resulting lightcurve from the modelled distributions of spots, as described in the previous section, is used as input to DoTS to reconstruct the surface brightness distribution using the maximum entropy χ^2 minimisation method (Collier Cameron 1997).

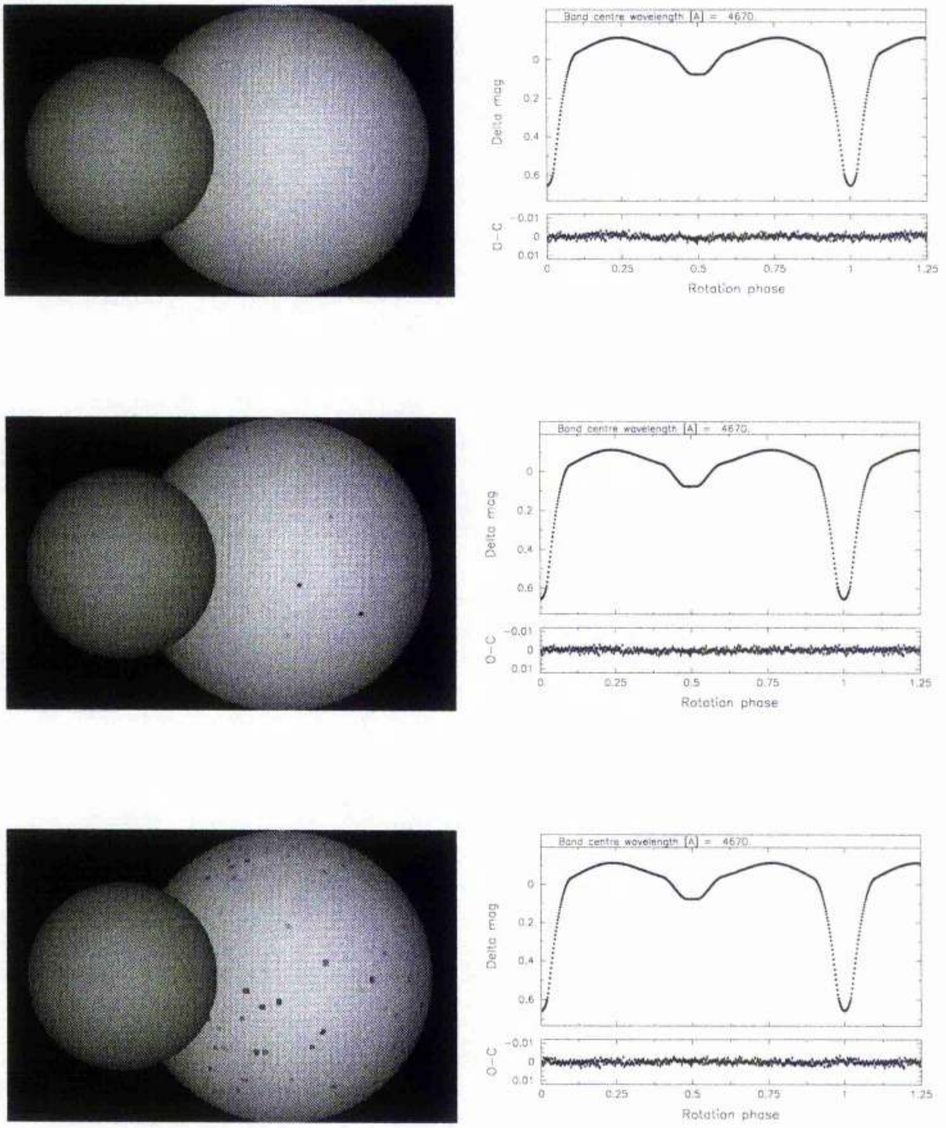

Figure 4.1: (left) The distribution of spot size distributions for sets 1 to 3. (right) The photometric lightcurve resulting from these spot distributions and the Maximum Entropy fit to these lightcurves. It was not possible to reconstruct surface brightness distributions for these three sets as the spot coverage is too low to be recovered using eclipse-mapping.

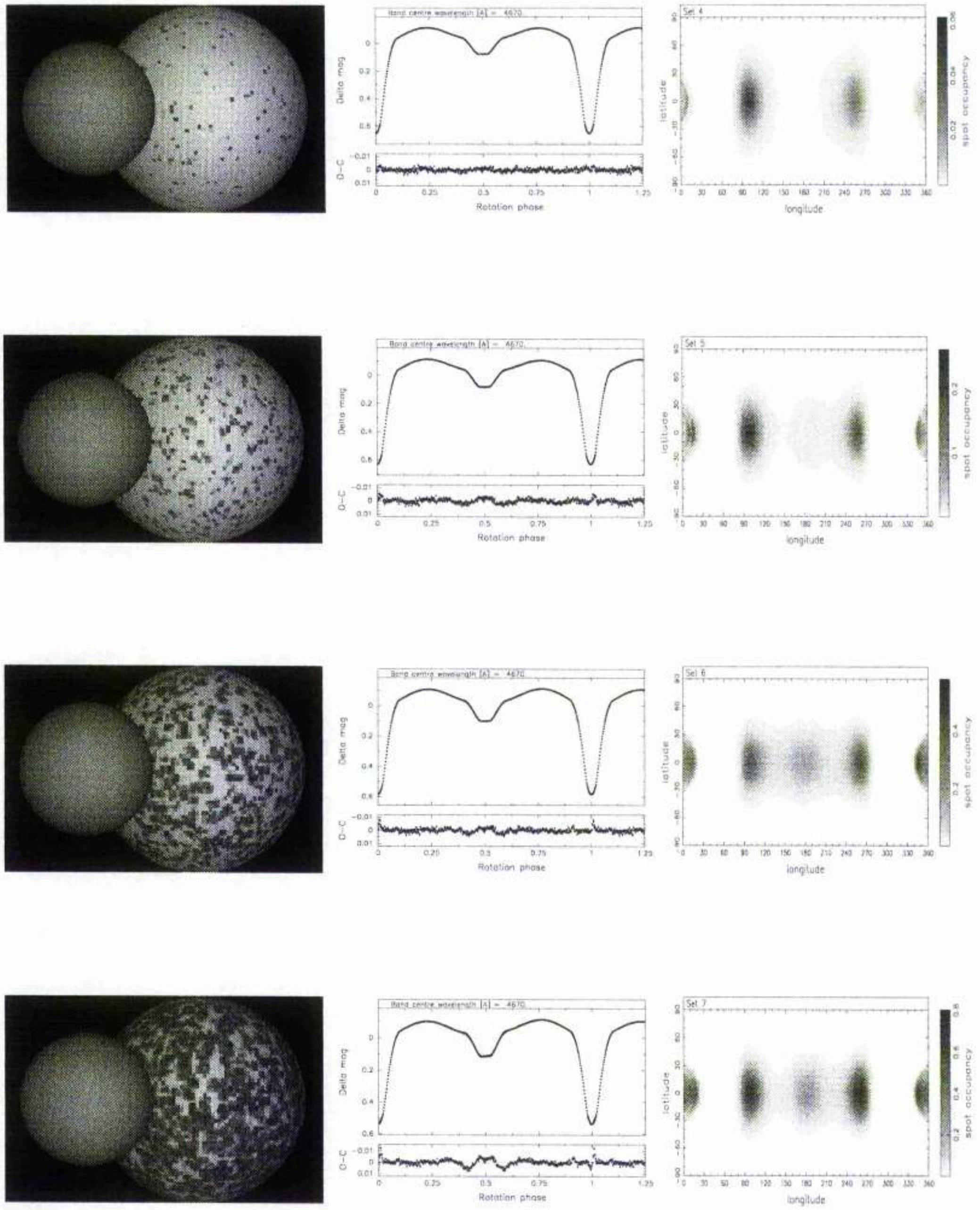

Figure 4.2: (left) The modelled distribution of spots for sets 4 (top) to 7 (bottom). (centre) The photometric lightcurve resulting from these spot distributions and the Max Ent fit to these lightcurves. (right) The surface brightness distribution that are reconstructed using the Max Ent eclipse-mapping technique. Note that phase runs in reverse to longitude.

4.4.1 Photospheric temperature

In the reconstruction of a surface brightness distribution of a binary star, it is imperative that the correct binary system parameters are used (Vincent, Piskunov & Tuominen 1993). Incorrect binary system parameters lead to a poor fit of the photometric lightcurve and to the appearance of spurious spot features on the surface brightness image to compensate for this. In this work, the assumed spot temperature used is approximately 1500 K cooler than the star's photospheric temperature. As the spot coverage increases, the surface brightness of the star will decrease compared to the star's photospheric temperature. This is particularly relevant for sets 4 to 7. In reconstructing the surface brightness distributions for each of these sets the photospheric temperature is treated as an unknown parameter, which is determined using a 'grid search' method. This method uses a grid of photospheric temperatures as input to DoTS ranging from 5500 K to 6100 K at 25 K intervals. For each set, the resulting χ^2 values are plotted as a function of temperature. The lowest χ^2 value is determined by the minimum of a quadratic fit to these values. The resulting best-fitting temperatures are 6024 K for set 4, 5981 K for set 5, 5860 K for set 6 and 5713 K for set 7. These values are used as the photospheric temperature for the reconstruction of the primary's surface brightness distribution.

4.4.2 Final image reconstruction

The images reconstructed for sets 4 to 7 are shown in Figure 4.2, however, the over-all spot coverage for sets 1 to 3 in Figure 4.1 was too small to be reconstructed. The photometric lightcurves for sets 1 to 3 are shown in the right-hand side of Figure 4.1. For sets 4 to 7, the fit to the photometric lightcurve and reconstructed surface brightness images are shown respectively in the centre and the right-hand side of Figure 4.2.

However what is distinctive about these plots are the spot features at the quadrature points (90° and 270°). These spot features are not artifacts of the maximum entropy reconstruction, but occur as a consequence of the χ^2 minimisation technique. If a star is peppered with small unresolved spots, the effect on the star's lightcurve will be to reduce the depth of the primary eclipse. To fit this with χ^2 minimisation it is necessary to increase the level of the whole computed lightcurve to fit the reduced primary eclipse depth. The difference in light at the quadrature points can only be accounted for by placing large

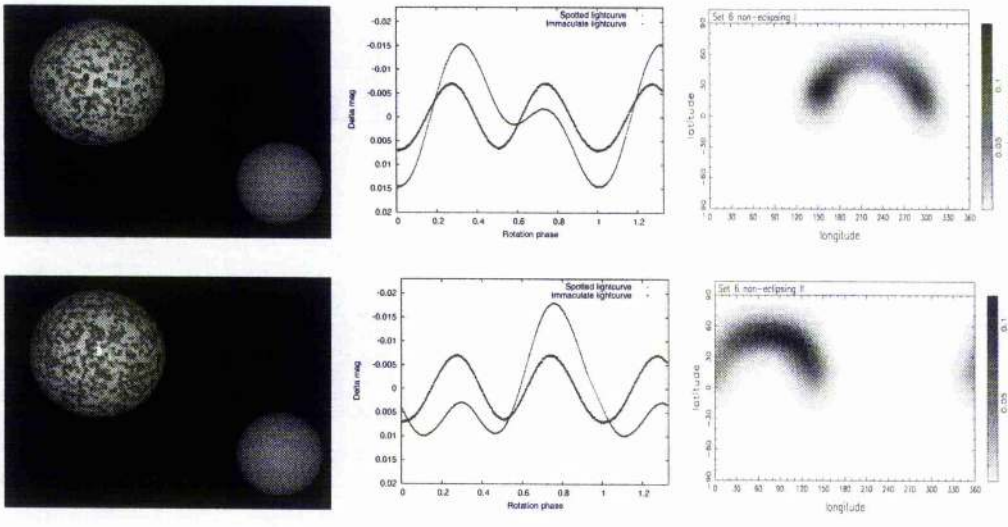

Figure 4.3: (left) The spot size distribution of set 6 applied to a non-eclipsing binary (inclination=45°). (centre) The Max Ent fit to the photometric lightcurve (thin line) with the lightcurve for an immaculate primary star (thick line) also shown for comparison. (right) The reconstructed surface brightness distribution image. Note that phase runs in reverse to longitude.

spots at these longitude points.

For sets 4 and 5, the spot feature at 270° longitude is fainter than the spot feature at 90° longitude as there is a higher degree of spot coverage at the first quadrature than at the second. In the reconstructed surface brightness distributions, the spots at 0° longitude result from the total spot coverage between second and third contact, i.e. during primary eclipse, while the spots at 180° longitude result from spots on the primary star visible during secondary eclipse.

4.4.3 Non-eclipsing binary system

In non-eclipsing binary systems the information content available in the lightcurve is less than for eclipsing binary systems. To illustrate this, the inclination of our eclipsing binary system was changed to 45°, making it non-eclipsing. The spot distribution of set 6 is applied to the primary's surface, and the surface brightness distribution is reconstructed in the same manner as previously described, and are shown in the upper panel of Figure 4.3. To test the reliability of these reconstructions we changed the random seed of the program that generates the input spot distribution. The reconstructed surface brightness distribution and photometric lightcurve resulting from these models is shown in the lower panel of Figure 4.3. For comparison the lightcurve of an immaculate non-eclipsing binary system is shown in these plots, illustrating how the tidally distorted surface geometry alone affects the binary system's lightcurve.

4.5 Discussion

This work has modelled the solar size distributions (Solanki 1999) extrapolated to active stars. In these distributions there are many spots that are too small to be resolved using Doppler imaging or eclipse-mapping techniques. The lightcurves resulting from these spot distributions were used as input to the Max Ent eclipse-mapping code DoTS. The resulting surface brightness distributions, with large spot features at the quadrature points (90° and 270°), bear little resemblance to the input distribution of spots. The reconstruction of spots at the quadrature points (90° and 270°) are not artifacts of the eclipse mapping technique, but a consequence of the χ^2 minimisation method.

The presence of spots over a large fraction of the stellar surface influences the shape of the lightcurve and consequently the derived stellar parameters. The peppering of a star's surface with small spots decreases the depth of the primary eclipse, resulting in a lower photospheric temperature of the primary star. To obtain a satisfactory fit to the photometric lightcurve it was necessary to reduce the temperature of the primary star from 6038 K to 6024 K (set 4, 6.1% spot coverage), 5981 K (set 5, 18% spot coverage), 5860 K (set 6, 48% spot coverage) and 5713 K (set 7, 100% spot coverage). This result shows how the degree of spottedness affects the determination of the correct photospheric temperature when using only photometric observations.

The unreliability of non-eclipsing lightcurve reconstruction is shown in Figure 4.3. As noted by (Spruit 1994), and reconfirmed by the results of this paper; the reconstruction of the input image from a photometric lightcurve requires a significant amount of a priori information about the object.

Spot features occurring at 90° and 270° are commonly reconstructed features of RS CVn binaries and are typically called 'active longitudes'. These features have been observed on numerous short-period active RS CVn binary stars such as EI Eri, II Peg,

σ Gem, HR 7275, AR Lac, SZ Psc, HK Lac (Berdyugina & Tuominen 1998; Lanza et al. 1998; Lanza et al. 2001; Jetsu 1996; Henry et al. 1995; Olah, Hall & Henry 1991). While the assumption of spots at preferred longitudes leads to acceptable fits to the lightcurve, it is not possible to distinguish whether the reconstructed spot features are single large spots or clusters of small spots. Active longitudes are interpreted as being the preferred longitude of emergence of magnetic flux. To determine if active longitudes are a reality it is necessary to determine the longitude of first emergence for each spot (Hall 1996), which is further complicated by the presence of differential rotation. Despite the differential rotation being lower on binary stars than on single stars for the same spectral type and vsini (Petit, Donati & Collier Cameron 2002), it will have the effect of displacing the spots from their emergence point.

Another approach for the reconstruction of a surface brightness distribution is the 'two-spot' model. This method can only account for gross asymmetries in the lightcurve by the assumption of two large spots. It cannot provide an accurate indication of the detailed spot properties on the stellar surface. The results shown in Figure 4.2 confirm Eaton, Henry & Fekel (1996) and show that 'two-spot' models do not model spot distributions accurately in terms of location, distribution and size. Examples of such rudimentary two-spot models for SV Cam include, Zboril & Djurašević (2003), Albayrak et al. (2001), Kjurkchieva, Marchev & Ogloza (2000), Djurasevic (1998), Patkos & Hempelmann (1994), Budding & Zeilik (1987) and Zeilik et al. (1988).

It is concluded from this work that while 'active longitudes' and the 'two spot model' can be used to fit the flux deficit of the photometric lightcurve caused by spots, they can give a misleading picture of the spatial distribution of spots if the surface of the star is peppered with a large number of small unresolvable spots.

CHAPTER 5

First Direct Evidence for a Polar Cap on SV Cam

This chapter has been submitted to Astrophysical Journal with authors Jeffers, Collier Cameron, Barnes, Aufdenberg and Hussain. Barnes & Collier Cameron made suggestions about the data analysis, while Aufdenberg provided the PHOENIX models. Hussain contributed by arranging a visit to CfA to work with Aufdenberg.

5.1 Abstract

We have used spectrophotometric data from the Hubble Space Telescope to eclipse-map the primary component of the RS CVn binary SV Cam over 9 HST orbits. We find from these observations and the HIPPARCOS parallax that the surface flux in the eclipsed low-latitude region of the primary is about 30% lower than computed from a PHOENIX model atmosphere at the effective temperature that best fits the spectral energy distribution of the eclipsed flux. This can only be accounted for if about a third of the primary's surface is covered with unresolved dark star-spots. Extending this to the full surface of the primary, we find that even taking into account this spot filling factor there is an additional flux deficit on the primary star. This can only be explained if there is a large polar spot on the primary star extending from the pole to latitude 48±6°.

5.2 Introduction

Over the last 20 years, Doppler imaging studies have revealed that rapidly rotating RS CVn binary systems frequently show long-lived polar caps. These features have been shown to be quite stable over extended time-scales of up to several years. Examples include HR 1099

(Vogt et al. 1999; Petit, Donati & Collier Cameron 2002), EI Eri (Hatzes & Vogt 1992; Washuettl, Strassmeier & Collier-Cameron 2001), UZ Lib (Oláh, Strassmeier & Weber 2002), HU Vir (Strassmeier 1994; Hatzes 1998), V1355 Ori (Strassmeier 2000) and IL Hya (Weber & Strassmeier 1998). Theoretical efforts to understand this phenomenon are currently focused on the role of meridional flows in sweeping magnetic flux from decaying active regions up towards the poles (Schrijver & Title 2001). In order to produce a polar spot in these simulations, however, bipolar active regions have to emerge at a rate 30 times faster than solar, implying that the photospheres of active stars should be peppered with many small spots.

In order to test this idea by measuring this filling factor, we were awarded 9 orbits of HST/STIS time in 2001 November to eclipse-map the starspot distribution on the F9V primary of SV Cam. We obtained spectrophotometric light-curves through three primary eclipses with a photometric signal-to-noise ratio of 5000. At this unprecedented precision, we discovered that using conventional limb-darkening models based on plane-parallel atmospheres gave very poor fits to the primary eclipse profile, particularly around the contact points (Jeffers et al. 2004c) (Chapter 6). We concluded that the spiked pattern of residuals could only be accounted for by either (i) an anomalous value of the limb darkening co-efficient, (ii) incorrect binary system parameters, or (iii) the assumed presence of a polar cap on the primary star or a combination of these effects.

SV Cam has been the target for numerous spectroscopic and photometric observations. Despite this, there are no established values for the two principal stellar parameters that define the shape of the photometric lightcurve i.e. the temperatures and radii of the primary and secondary stars. As discussed in Jeffers et al. (2004c) (Chapter 6), the determination of these parameters is essential for a correct modelling of the binary system light-curve. If the system parameters are wrong a satisfactory fit to the lightcurve will only be obtained by placing a greater total spot area than is present when the correct parameters are used. In Jeffers et al. (2004c) (Chapter 6) we have determined the radii of the two stars through lightcurve fitting, but it was not possible to model the depth of the eclipse correctly, i.e. without artificial spot features appearing on the final image. Owing to the high inclination of SV Cam, the poles of the primary star remain uneclipsed, so it is not possible to reconstruct an image at all latitudes.

In this paper we empirically determine the temperatures for both primary and

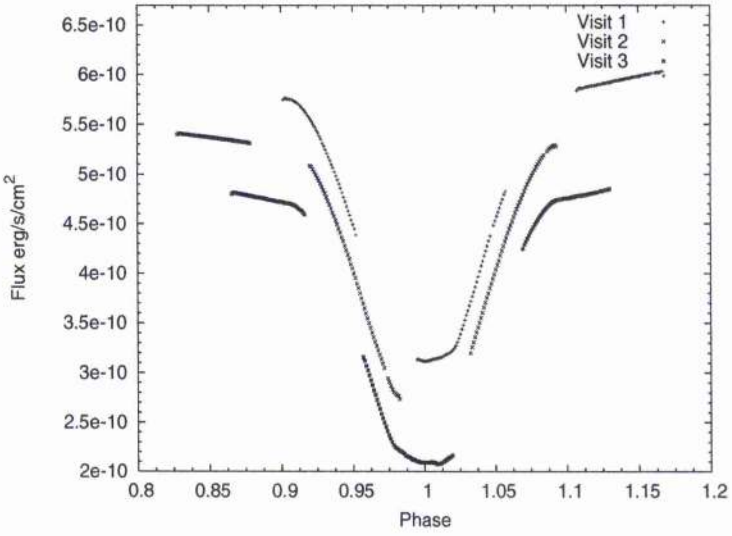

Figure 5.1: The 9 spacecraft orbits that comprise the 3 primary eclipses of SV Cam. An offset of 5×10^{-11} ergs/s/cm^2 has been included for clarity.

secondary components by fitting PHOENIX spherical model atmospheres to our spectra. As our HST data are calibrated in absolute flux we determine how much light is missing due to the surface of SV Cam's primary being covered with small star-spots. Finally we show that there are two polar caps on the primary star and determine their size.

5.3 Observational Details

Three primary eclipses of SV Cam were observed by the HST, using the Space Telescope Imaging Spectrograph with the G430L grating. The observations comprised 9 spacecraft orbits and spanned 5 days at 2 day intervals from 1-5 November 2001 as shown in Table 5.1. Summing the recorded counts over the observed wavelength range 2900 Å to 5700 Å results in a photometric lightcurve. A plot showing the 9 spacecraft orbits and the 3 primary eclipses that comprise the photometric lightcurve is shown in Figure 5.1. The observations have a cadence of 40s and a photometric precision of 0.0002 magnitudes (S:N 5000) per 30 s exposure. These observations and the data reduction method are explained in greater detail in Jeffers et al. (2004c) (Chapter 6).

Visit	Obs. Date	UT Start	UT End	Exposure Time(s)	No of Frames
1	01 November 2001	20:55:56	01:00:17	30	165
2	03 November 2001	14:34:29	18:38:21	30	165
3	05 November 2001	09:49:17	13:52:22	30	165

Table 5.1: HST Observations of SV Cam

5.4 Phoenix Model Atmospheres

The synthetic spectra we use in this paper are based on an extension of the grid of PHOENIX model atmospheres described by Allard, Hauschildt & Schweitzer (2000). This extended grid includes surface gravities larger than $\log(g) > 3.0$ needed for main sequences stars. These models are as described by Hauschildt et al. (1999), but include an updated molecular line list. The models are computed in spherical geometry with full atomic and molecular line blanketing using solar elemental abundances. In these models, the stellar mass is 0.5 $M_\odot$ and the convection treatment assumes a mixing-length to pressure scale height ratio of 2. There are 117 synthetic spectra in total. The effective temperature runs from 2700K to 6500 K in 100K steps at three surface gravities: $\log(g) = 4.0$, 4.5, and 5.0. The wavelength resolution of these synthetic spectra is 1Å.

The PHOENIX spectra were converted to the same resolution scale as the HST spectra by convolving them with a Gaussian profile of width equal to the instrumental resolution, 2.73Å. Each spectrum was then trimmed to the wavelength range 3000Å - 5700Å.

5.5 Temperature Fitting using HIPPARCOS Distance

In this section we determine the temperature for both the primary and secondary components of SV Cam using PHOENIX model atmospheres. For consistency we shall denote the flux at the Earth by f, and the flux at the star by F.

5.5.1 Primary star + secondary star

In Jeffers et al. (2004c) (Chapter 6) we accurately determined the radii of the primary and secondary components through lightcurve fitting to be as shown in Table 5.2 for the

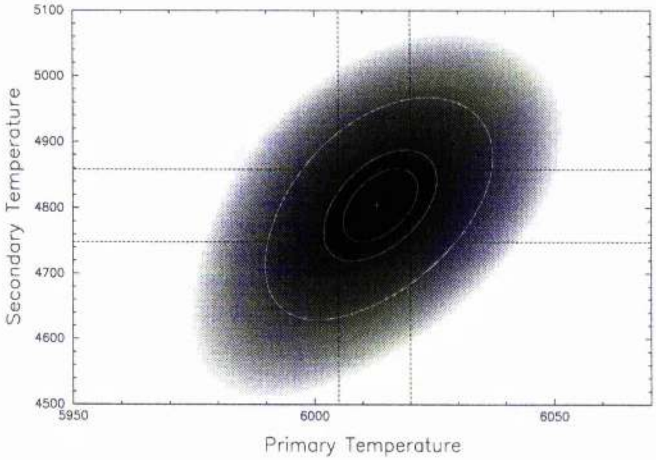

Figure 5.2: Contour plot of the χ^2 landscape of the combined primary and secondary stars. The minimum χ^2 value occurs at $6013 \pm 19\,\mathrm{K}$, and $4804 \pm 143\,\mathrm{K}$, for the primary and secondary stars respectively. From the centre of the plot the first contour ellipse represents the 1 parameter $1\,\sigma$ confidence limit at 63.8%, the second ellipse represents the 2 parameter $1\,\sigma$ confidence limit at 63.8% whilst the third elipse represents the 2 parameter $2.6\,\sigma$ 99% confidence limit.

	Primary Star	Secondary Star
Radius	$1.24\pm0.04\,\mathrm{R}_\odot$	$0.79\pm0.03\,\mathrm{R}_\odot$
Mass	$1.14\pm0.03\,\mathrm{M}_\odot$	$0.73\pm0.02\,\mathrm{M}_\odot$
log g	4.31 ± 0.04	4.5 ± 0.03

Table 5.2: Stellar Parameters of SV Cam

primary and secondary stars respectively. Knowing these radii we can evaluate the flux contribution from the secondary star relative to that of the primary star. The PHOENIX spectra are scaled by r^2/d^2_{HIPP} to give flux at the Earth rather than at the stellar surface. The PHOENIX flux received at the Earth outside of eclipse can be expressed as;

$$f_{ptotal} = \frac{r^2_{pri}}{d^2_{HIPP}}(F_{pri} + \frac{r^2_{sec}}{r^2_{pri}}F_{sec}) \tag{5.1}$$

where F_{pri} and F_{sec} are the PHOENIX model atmosphere fluxes for the primary and secondary stars respectively; r_{pri} and r_{sec} are the primary and secondary radii, d_{HIPP} is the HIPPARCOS distance (84.96 ± 8.5 pc). We fitted this equation for each permutation of primary temperature in the range $T_{pri} = 4500$ K to 6500 K, and secondary temperature $T_{sec} = 2800$ K to 5500. The best fitting pair of temperatures was determined using χ^2 minimisation;

$$\chi^2 = \sum_{\lambda(i)=1}^{N} \left(\frac{f_{out}(i) - \gamma_{total} * f_{ptotal}(i)}{\sigma(i)} \right)^2 \tag{5.2}$$

where f_{out} is an averaged spectrum outside of primary eclipse, and γ_{total} is a scaling factor. A scaling factor is included so that the shape of the spectrum is fitted rather than the absolute flux levels. This scaling factor is defined as;

$$\gamma_{total} = \frac{\sum f_{out} f_{ptotal}/\sigma^2(i)}{\sum (f_{ptotal})^2/\sigma^2(i)} \tag{5.3}$$

The results for the χ^2 minimisation are shown in Figure 5.2 in the form of a contour plot. The minimum χ^2 value occurs at 6013 ± 19 K, and 4804 ± 143 K, for the primary and secondary stars respectively. As is evident from the shape of the contour plot and the size of the errors for each temperature, the primary temperature is very sensitive, in contrast to the secondary temperature, to small temperature changes (i.e. the secondary places a lower constraint on the solution). The best fitting PHOENIX model atmospheres, 6000 K and 4800 K, and an observed spectrum outside of eclipse are shown in Figure 5.3. We neglect any reddening correction due to the proximity of SV Cam.

5.5.2 Primary star

The first step in determining the temperature of the primary star in isolation is to remove its spectrum from that of the secondary star. To achieve this we simply subtracted an average spectrum inside the primary eclipse, f_{ecl}, from an average spectrum outside of

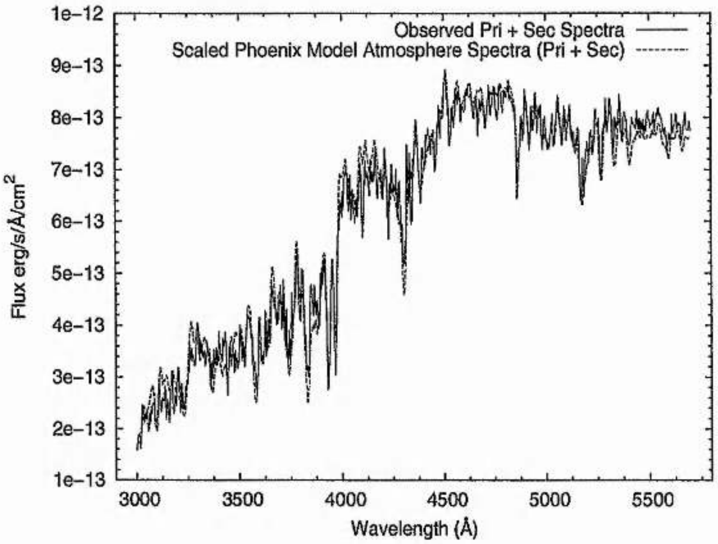

Figure 5.3: Plot showing the combined primary and secondary stars outside of eclipse, f_{out}, and the best fitting PHOENIX spectrum (6000 K and 4800 K for the primary and secondary stars respectively).

eclipse, f_{out} to elimate limb darkening effects. The spectrum that results is the spectrum of the primary star, but with a reduced flux level that is equivalent to the primary star having a radius of the secondary star. This missing light will be referred to as f_{mis} in the rest of this paper.

The contribution to the total PHOENIX flux is from only the primary star, so equation (5.1) becomes;

$$f_{ptotal(pri)} = \frac{r_{pri}^2}{d_{HIPP}^2}(F_{pri}) \tag{5.4}$$

As before, the optimal value of the primary temperature is determined through χ^2 minimisation. The scaling factor is then equal to;

$$\gamma_{pri} = \frac{\sum f_{mis} f_{ptotal(pri)}/\sigma(i)^2}{\sum (f_{ptotal(pri)})^2/\sigma(i)^2} \tag{5.5}$$

Figure 5.4 shows how the reduced χ^2 varies with primary temperature. A parabolic fit results in a minimum temperature of 6038 ± 8 K. The errors were calculated by setting $\Delta\chi^2 = 1$ on the full χ^2 value.

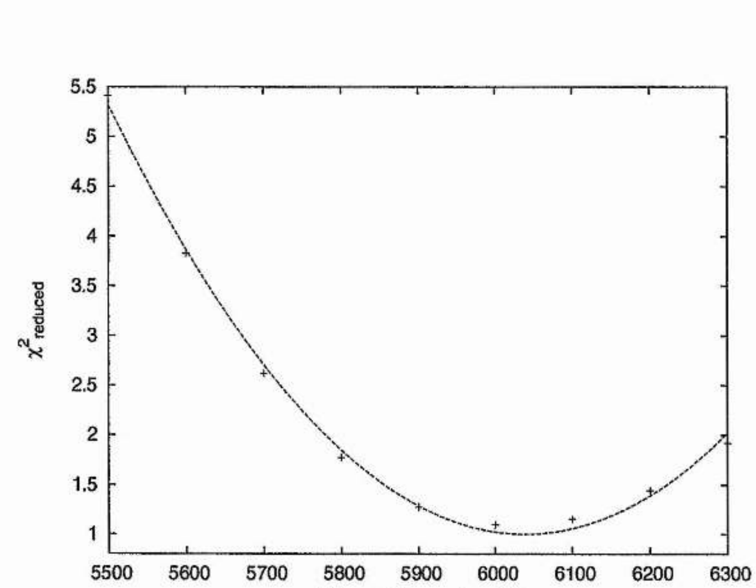

Figure 5.4: The parabolic fit that determines the temperature minimum to be 6038 ± 8 K

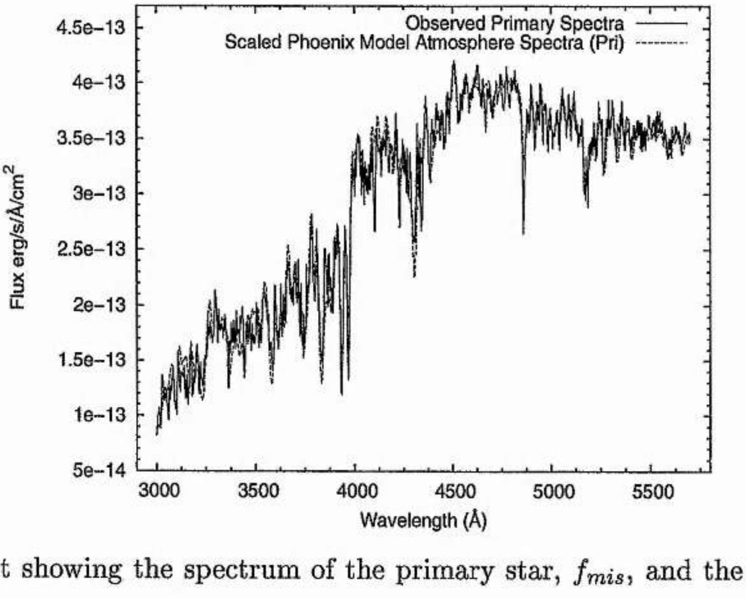

Figure 5.5: Plot showing the spectrum of the primary star, f_{mis}, and the closest match PHOENIX model atmosphere (6000 K)

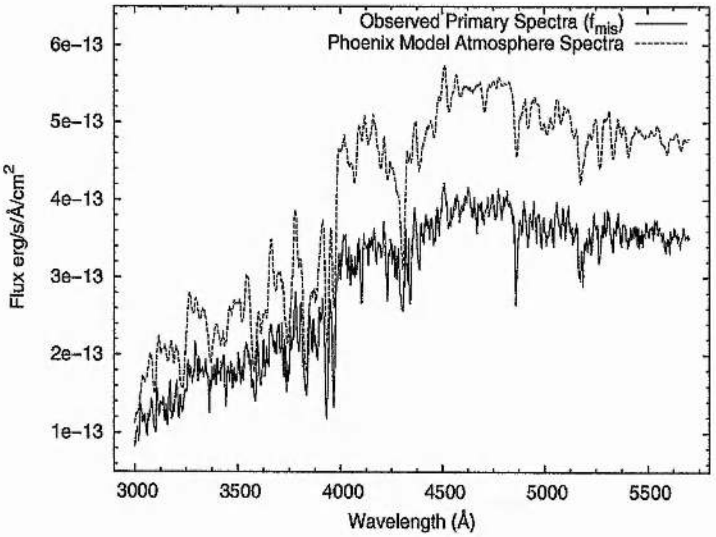

Figure 5.6: As per Figure 5.5 but without using a scaling factor.This plot illustrates the flux deficit due to the presence of dark star-spots on the surface of the primary.

5.6 Star-spot coverage

In Figure 5.5 we show the best fitting PHOENIX spectrum to the primary spectrum, which includes a scaling factor. The advantage of using HST spectro-photometric observations is that for each point on our photometric lightcurve we have a value for its absolute flux (i.e. the flux integrated over 3000Å - 5700Å in each spectrum). Replotting Figure 5.5 without the scaling factor in Figure 5.6, clearly shows that there is a flux deficit on the surface of the primary star, when compared with the flux computed from a PHOENIX model atmosphere at the effective temperature that best fits the spectral energy distribution of the eclipsed flux.

Using the eclipse mapping technique Jeffers et al. (2004c) (Chapter 6), have already verified the existence of several dark spots at low latitudes on the primary star, but these are insufficient to account for the flux deficit. The total missing flux can only be accounted for if the primary's surface is peppered with unresolved dark star-spots. The dark star-spot filling factor is given by:

$$\alpha = 1 - \gamma \tag{5.6}$$

where α is the fractional star-spot coverage, and γ is the scaling factor as defined in equation 5.5. This results in the fractional coverage of dark star-spots on SV Cam to be 28%. Taking into account the error on the HIPPARCOS distance this translates to if d$_{HIP}$=93.46 pc then the spot coverage will be 14%, whilst if d$_{HIP}$=76.46 pc then the spot coverage will be 41%.

5.7 Polar Spot

Our determination of the spot coverage factor only accounts for the equatorial latitudes of the primary that are eclipsed by the secondary. However, due to the near 90° inclination of the binary system it is not possible to recover high-latitude spots or polar caps through the eclipse mapping method. In this section we will firstly show that there is a polar cap on SV Cam and then we will determine its size.

5.7.1 Extent of a polar cap on SV Cam

If there is a polar cap on SV Cam, then total flux on the two stars can be expressed as (following from equation(5.1));

$$f_{ptotal} = \frac{r_{pri}^2}{d_{HIPP}^2}(F_{pri}(1 - A_{pc}) + \frac{r_{sec}^2}{r_{pri}^2}F_{sec}) \tag{5.7}$$

where A$_{pc}$ is the area of the polar cap. To obtain a full view of the primary star's surface we used an averaged spectrum out of eclipse, but with the secondary's contribution subtracted. It is valid to subtract the PHOENIX spectrum as we assume that the secondary is not spotted or is faint enough that the additional flux deficit from star-spots on the secondary is negligible. Following from equation(5.3) the scaling factor γ now becomes:

$$\gamma_{pc} = \frac{f_{out} - \frac{r_{sec}^2}{d_{HIPP}^2}F_{sec}}{\frac{r_{pri}^2}{d_{HIPP}^2}(1 - A_{pc})F_{pri}} \tag{5.8}$$

If there are no polar caps on SV Cam, A$_{pc}$ will be zero and the flux deficit should equal the previously determined flux deficit in the primary spectrum, i.e.$\gamma_{pc} = \gamma_{pri}$. We assume that the previously calculated spot coverage area for the missing light of the primary is valid for the whole primary star, where equation(5.5) is extended to use r$_{pri}$ rather than r$_{sec}$. Equivalently we can set γ_{pc} equal to γ_{pri} to solve for A$_{pc}$, e.g.;

$$(1 - A_{pc}) = \frac{f_{out} - \frac{r_{sec}^2}{d_{HIPP}^2}F_{sec}}{f_{mis}} \tag{5.9}$$

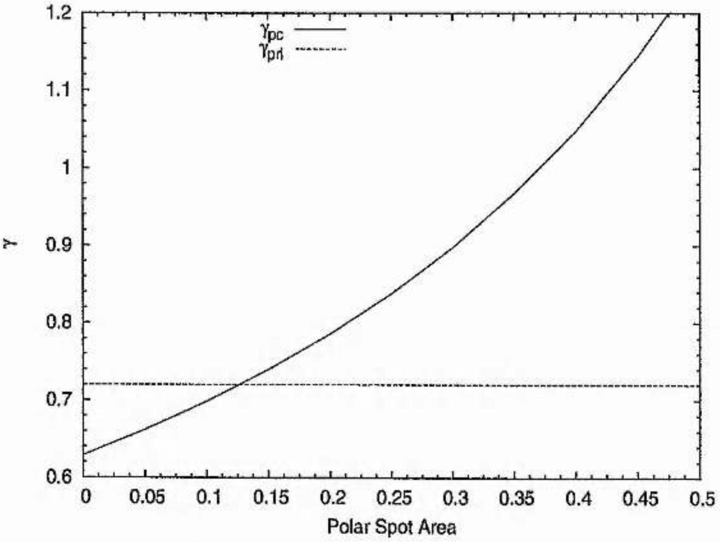

Figure 5.7: Graphical representation of equation 5.9, where γ_{pc} (equation 5.8) is plotted as a function of polar spot area along with γ_{pri}. The area of the polar cap is where the two lines intersect at Spot Area 0.125.

This equation is illustrated by Figure 5.7, where the γ_{pc} and γ_{pri} are plotted as a function of polar spot area. The intersection point (0.142) indicates the fractional area of the projected disc that is covered by polar caps on SV Cam.

5.7.2 Reconstruction of a theoretical polar cap on SV Cam

The value for A_{pc} is only a fractional value by which the polar cap has decreased the light of the star. It does not take into account that the star is a sphere, rather than a disc, any limb or gravity darkening, or any spherical oblateness. To account for these parameters, the binary eclipse-mapping tomography code DoTs (Collier Cameron 1997) was used to model theoretical polar spots on the surface of SV Cam. The input to DoTs is in the form of (i) longitude, set to 0°; (ii) latitude, set to 90°; (iii) radius set to 10°, 20°, 30°,40°,50° and 60°; (iv) brightness and (v) sharpness, which were both set to make the spot as uniformly dark as possible. An example of no polar cap, and with a 40° and 60° polar spot are shown in Figure 5.8. We assume that the polar cap does not contribute to the total flux of the star.

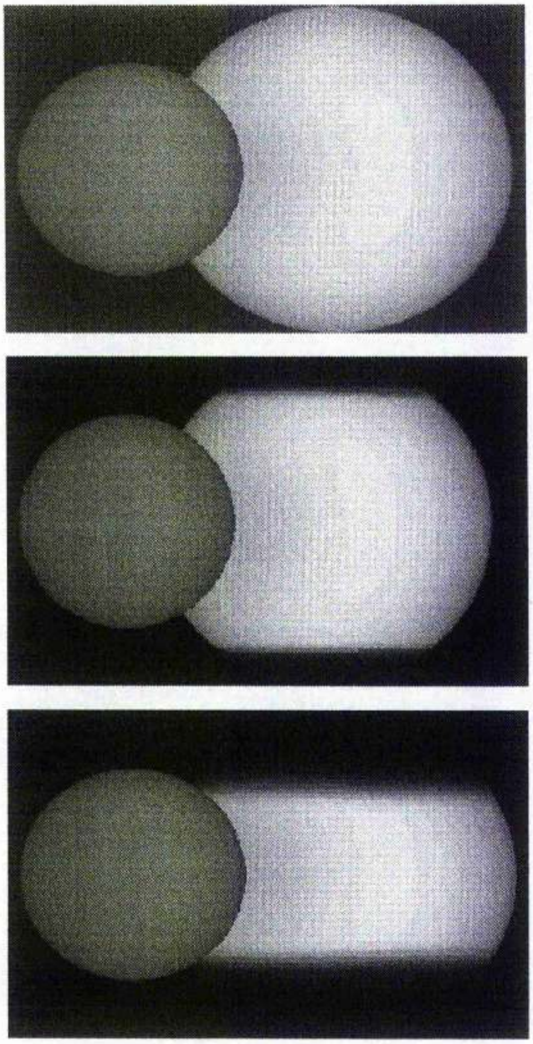

Figure 5.8: Pictorial representation of the polar spots of SV Cam, with no polar cap, a 40° polar cap and a 60° polar cap.

5.7.3 Effect of a polar cap on the primary eclipse

The effect of the polar cap on the primary eclipse will be to increase the depth of the eclipse. The presence of a polar cap effectively reduces the area of the primary star. When the primary star is then eclipsed the secondary obscures a larger fraction of the primary's surface area than when there was no polar spot. This is illustrated in Figure 5.9, where there is an obvious difference in the eclipse depth for a star with no polar cap and one with a 60° polar cap.

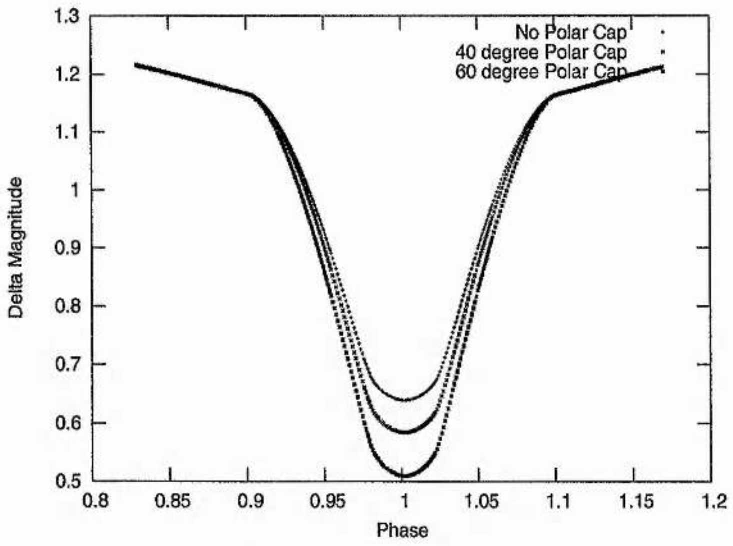

Figure 5.9: Variation of a theoretical primary eclipse lightcurve due to the presence of a polar spot of radius of 40° and 60° (deepest lightcurve). For comparison the primary eclipse lightcurve without a polar spot is also plotted. We show the only the primary eclipse as this is the part of the lightcurve that is most affected by the presence of a polar cap.

5.7.4 Size of the polar cap on SV Cam

The fractional decrease in stellar flux as a function of theoretical polar spot size is shown in Figure 5.10, where we assume that the polar cap contributes negligible flux. Also plotted in Figure 5.10 is the fractional area of a polar-spot as deduced in the previous section. We conclude that the polar spot on SV Cam is $42 \pm 6\,^{\circ}$.

5.7.5 Lightcurve of SV Cam

As shown in Figure 5.9 the presence of a polar spot will increase the depth of the primary eclipse. Figure 5.11 shows how a 42° polar cap will influence the lightcurve of SV Cam. Contrasting this, the peppering of small star-spots will decrease the depth of the eclipse as shown in Figure 5.12. In a complimentary paper, Jeffers et al. (2004c) (Chapter 6), we show how to obtain the best fits to the data.

The combination of 42° polar caps and 28% surface coverage of small star-spots is shown in Figure 5.14. This translates to the lightcurve shown in Figure 5.13. For clarity the lightcurve of SV Cam is also shown without any spot features.

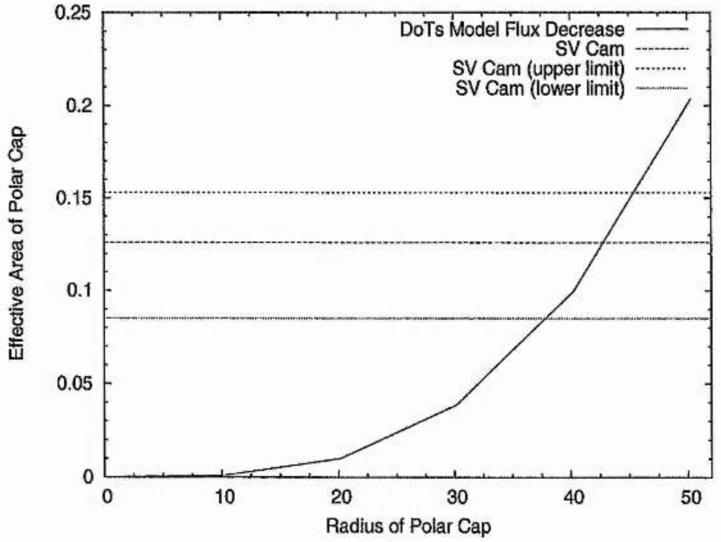

Figure 5.10: Plot of the fractional decrease in the stellar flux of SV Cam as a function of theoretical polar spot size. Also plotted is the fractional missing light for SV Cam as determined in the previous section.

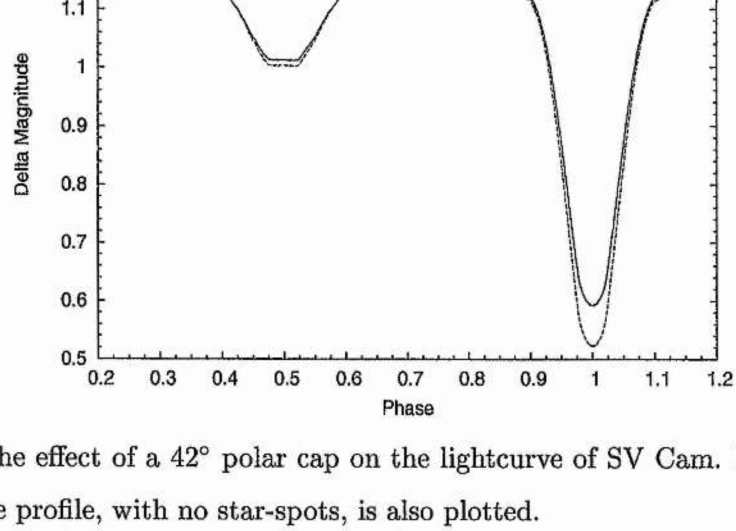

Figure 5.11: The effect of a 42° polar cap on the lightcurve of SV Cam. For comparison the immaculate profile, with no star-spots, is also plotted.

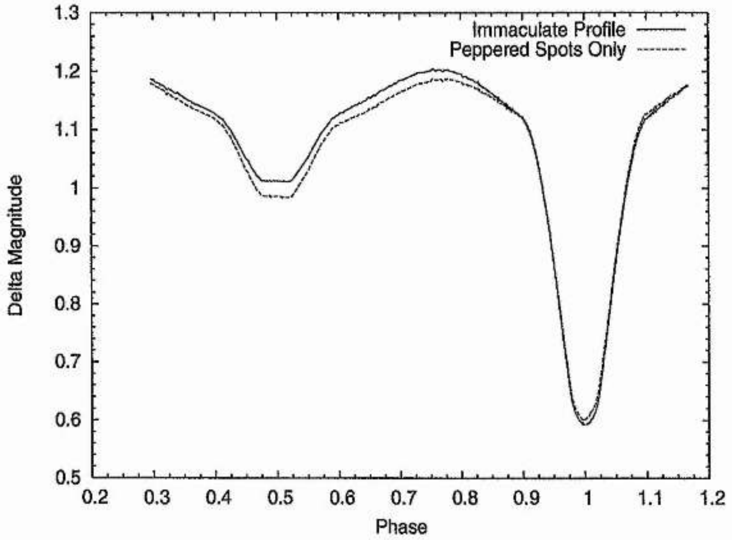

Figure 5.12: The effect of 28% small star-spot coverage on SV Cam. For comparison the immaculate profile, with no star-spots, is also plotted.

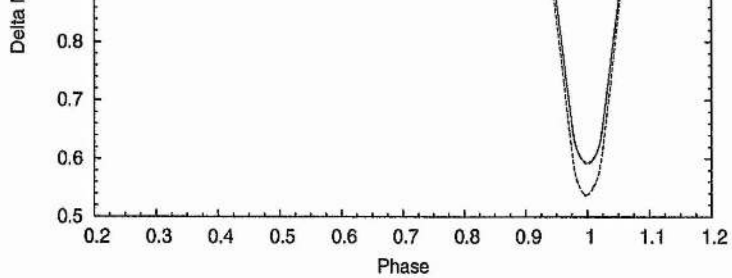

Figure 5.13: The effect of a combination of 42° polar cap and 28% spot coverage on the lightcurve of SV Cam. For comparison and immaculate profile, with no star-spots, is also plotted.

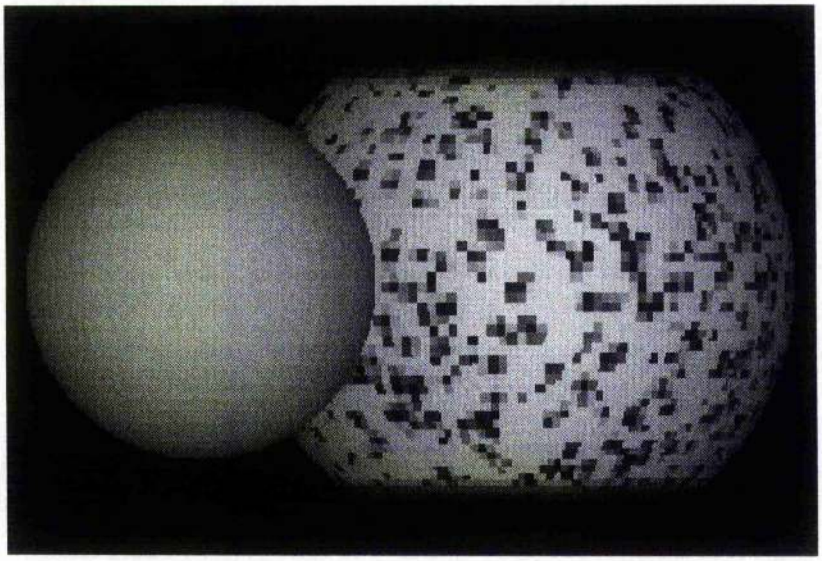

Figure 5.14: A model of SV Cam showing 28 % spot coverage and a 42° polar cap.

5.8 Discussion

The best fitting temperature of the primary star, 6013 K, is in good agreement with the value of 6000 K of Lehmann, Hempelmann & Wolter (2002), whilst the secondary temperature, 4804 K, is in best agreement with the value of 4700 K of Rainger, Hilditch & Edwin (1991). The temperatures that other investigators have observed range from 5700 K (Patkos & Hempelmann 1994) to 6440 K (Albayrak et al. 2001) for the primary star and 4140 K (Hilditch, McLean & Harland 1979) to 5600 K (Popper 1996) for the secondary star. The range in values extends from poor data quality, incomplete lightcurves and the inability to solve simultaneously for the binary system parameters and the spot coverage. However, the advantage that we have is that we have spectrophotometric HST observations i.e. a photometric lightcurve with absolute fluxes which can be directly compared with PHOENIX model atmospheres to fit for the temperatures of the two stars.

There are two important results from this paper concerning the spot coverage of SV Cam. The first is that the surface of SV Cam is peppered by 28% star-spots. Jeffers et al. (2004c) (Chapter 6) reconstructed an image of SV Cam using the HST and ground based photometric data using the eclipse mapping technique. Our final image showed the presence of large dark star-spots at equatorial latitudes but they were not large enough to account for 28% of the eclipsed part of the primary's surface being covered with star-spots.

The second important result of this paper is that there is certainly a dark polar cap on SV Cam. The existence of polar caps on magnetically active stars has always been a controversial issue. The spectroscopic signature of a polar cap is a line profile with a flat-bottomed core. In some stars with low *vsini* this could conceivably be caused by chromospheric in-filling of the cores of strong photospheric lines (Byrne 1992; Byrne 1996). This result independently confirms that the polar cap is a reality and is not just an artifact of the imaging process. The high resolution spectroscopic observations of Lehmann, Hempelmann & Wolter (2002) showed that SV Cam had no polar cap, but only high latitude spots. The surface area of the primary star that has a polar cap in this work is far greater than in these observations. If our flux deficit is due to only the presence of high latitude spots then their structure would be of a very abnormal nature compared to other RS CVn binaries that have been Doppler imaged.

In Chapter 6 (Jeffers et al. 2004c) we showed that lightcurve models without a polar cap were not sufficient to correctly fit the primary eclipse profile particularly at the contact points. As shown in figure 5.9, the presence of a the polar cap will increase the depth of the primary eclipse, and if it is not taken into account when fitting the lightcurve, it will not be possible to solve the binary system parameters correctly. Jeffers et al. (2004c) (Chapter 6) further solved for the radii and polar cap size using χ^2 minimisation. The optimally fitting polar cap size of $46\pm8^\circ$ is in good agreement with the value independently determined in this paper.

TiO-band monitoring (O'Neal, Neff & Saar 1998) has indicated that between 30% and 50% of a star's surface may be covered in starpots at all times. Our result of 28% spot coverage for the eclipsed equatorial regions in addition to a 14% polar cap are a further confirmation of this degree of spot coverage. Conventional Doppler images show that up to 20% of the star's surface is spotted, mainly in the form of high latitude structure and a polar cap. This discrepancy can be accounted for if the star's surface is peppered with dark star-spots, too small to be resolved with Doppler imaging.

The high total spot coverage on the primary star can have important implications for the overall structure of the star. Spruit & Weiss (1986) investigated this and concluded that over thermal timescales the star will readjust its structure to compensate in radius and temperature. Also standard colour-surface brightness relation will break down if star-spots cover a large fraction of the stellar surface, but contribute little to the stellar optical flux. To illustrate this point, it is possible to determine the stellar radius, R, using standard colour-surface brightness relation to obtain the angular diameter and the distance from the HIPPARCOS parallax. Using the relation $Rsini = (P_{rot}/2\pi)vsini$ (O'Dell, Hendry & Collier Cameron 1994), in a survey of axial inclination of G dwarfs on the α Per and Pleiades clusters, found that $sini > 1$ for several stars. In the context of our results this can be understood if the high spot coverage causes R to be underestimated, and would account for the large variance of binary system parameters for SV Cam.

This work provides strong evidence, independently of Doppler Imaging, that the poles of SV Cam's primary star are darkened by extensive polar caps, and that at lower latitudes the photosphere is peppered with small star-spots as has been suggested by TiO band monitoring. It is important to establish that these stars are in fact peppered by small star-spots in addition to a polar cap, as this can significantly impact theoretical interpretations of the spot distributions on these stars.

CHAPTER 6

Eclipse Mapping of the Star-spot Distributions on SV Cam using the Hubble Space Telescope

This paper has been submitted to MNRAS with the following author list: Jeffers, Barnes, Collier Cameron, Donati. Barnes contributed to the data analysis, Collier Cameron applied for the data, and with Donati made suggestions in the data analysis.

6.1 Abstract

We have used maximum entropy eclipse mapping to recover images of the visual surface brightness distribution of the primary component of the RS CVn eclipsing binary SV Cam, using high-precision photometry data obtained during three primary eclipses with STIS aboard the Hubble Space Telescope. These were augmented by contemporaneous ground-based photometry secured around the rest of the orbit. The information content of the final image and the fit to the data were optimised with respect to various system parameters using the χ^2 landscape method. We found that dark spots are recovered on the image of the primary at first and second quadrature (phases 0.25 and 0.75), resulted in observed minus computed residuals showing strong spurious peaks at the quadrature points. It was only possible to reduce these peaks with the addition of a polar cap, and the reduction of the primary star's temperature to account for the star being peppered with spots below the resolution limits of eclipse mapping.

6.2 Introduction

Star-spots and other forms of magnetic activity are prevalent on rapidly rotating stars with temperatures low enough to have outer convective zones. The extreme dynamo activity in these rapidly rotating cool stars leads to the suppression of convection over large areas of the stellar photosphere. These giant starspots can modulate the light of such an active star as it rotates by up to tens of percent. In general, stars that exhibit this type of activity are solar-type stars with spin periods of less than one day. This rapid rotation is seen in half the G and K dwarfs in open clusters younger than 100 Myr, and may also persist into middle age through tidal locking in a close binary systems such as RS CVns.

Doppler imaging is a powerful tool for determining where spots congregate on the stellar surface, but it is less successful at determining how much overall spot activity is present. Other methods such as TiO-band monitoring studies (O'Neal, Neff & Saar 1998) indicate that up to 40% of the stellar surface is spotted, compared to 10% from Doppler imaging. The discrepancy in these methods can be accounted for if the stellar surface is heavily covered by spots that are too small to be resolved through Doppler imaging (radius$\leq$ 40,000 km). To resolve this, we have used the exquisite photometric capabilities of the HST to eclipse-map the inner face of the G0V primary of the eclipsing binary SV Cam.

SV Cam is a short period (0.59 days) rapidly rotating (vsini=$102\,\mathrm{km\,s^{-1}}$) RS CVn totally eclipsing binary system. It has been extensively observed since its discovery by Guthnick (1929). It was chosen as a target, from the Strassmeier et al.(1993) catalogue of chromospherically-active binary stars, because; (i) its period is less than a day, to ensure that the activity levels are comparable to single ultra-rapid rotators found in young clusters, (ii) its out-of-eclipse lightcurve is established to show variations of at least 0.1 mag, (iii) the equator and mid latitudes are eclipsed, (iv) the contrast between its components (G0V / K5V) is such that the cool secondary acts as a dark occulting disc during primary eclipse.

By using eclipse mapping it is possible to determine the detailed locations of low latitude spots on the stellar surface. If spots are present on the inner surface of the primary, that is occulted by the cooler secondary star, jagged discontinuities will be produced on the eclipse profile as the primary is occulted by the secondary. The timescales and amplitudes

Visit	Obs. Date	UT Start	UT End	Exposure Time(s)	No of Frames
1	01 November 2001	20:55:56	01:00:17	30	165
2	03 November 2001	14:34:29	18:38:21	30	165
3	05 November 2001	09:49:17	13:52:22	30	165

Table 6.1: HST Observations of SV Cam

of these discontinuities will reflect the distribution of spot sizes on the inner surface of the primary. Eclipse mapping can determine the locations of these spots more precisely than is possible with conventional spectroscopic Doppler imaging, or lightcurve modelling techniques.

Using the MaxEnt eclipse-mapping code DoTS (Collier Cameron 1997; Collier Cameron & Hilditch 1997) we shall solve the HST and ground based lightcurve for the stellar parameters of the stars, and to recover spatial information about the spot locations.

6.3 Observations

Contemporaneous HST and ground based observations were obtained to eclipse map SV Cam. The primary eclipse is annular, so that the K6 secondary provides a dark occulting disc as it scans the primary at a relative transverse speed of $296\,\mathrm{km\,s^{-1}}$.

The ground based photometric observations were obtained to complete the light curve outside primary eclipse making it possible to account for any global asymmetry in the lightcurve due to the presence of any uneclipsed spots.

6.3.1 HST observations

We observed three primary eclipses of SV Cam during three HST visits at intervals of 2 days between 2001 November 1 to 5. A total of 9 spacecraft orbits were devoted to the observations. The G430L grating of STIS was used to disperse starlight over 2048 CCD elements. The observations cover a wavelength range from 2900 Å to 5700 Å, with a cadence of 40 s. The choice of 30 s as an optimal exposure was set as a trade-off between maximising signal-to-noise per exposure and minimising the time interval between

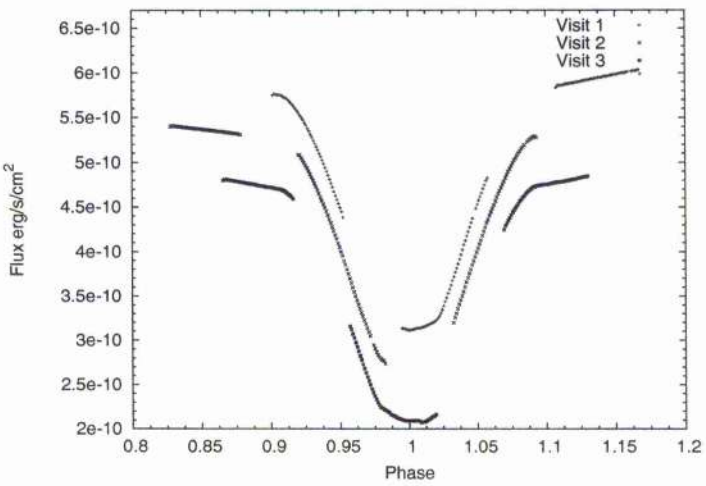

Figure 6.1: The comprising sections of the primary eclipse from each of the 3 HST visits, with an off-set of 5×10^{-11} ergs/s/cm^2 for clarity.

observations.

The total count over the entire detector is 9.4×10^7 electrons per 30 s exposure. The photometric precision is calculated to be 0.0002 magnitudes (S:N = 5000) per 30 s exposure. The main source of systematic error due to the subtle motion of the satellite was removed by cross-correlating each frame with respect to a template spectrum, and then adding or subtracting a scaled number of counts. After correcting for this 'jitter' the RMS scatter was consistent with the error expected from photon noise. A summary of observations is tabulated in 6.1, and illustrated in Figure 6.1.

Given that SV Cam has a high declination (82°), it was visible to the HST for 59 minutes per orbit. Of the 59 minutes available per orbit, 6 were spent on guide-star acquisition, 6 on ACQ, and 3 on GO wavecal (as auto-wavecal was disabled), on the first orbit of each visit leaving 45 minutes for exposures. Subsequent orbits just required guide star reacquisition, and GO wavecals, leaving 51 minutes for exposures. In total, 495 spectra were taken of SV Cam.

6.3.2 Ground based photometry

The ground based photometric observations were obtained with the 0.93-m James Gregory Telescope (JGT) at the University of St Andrews, using a Wright Instruments CCD camera mounted at the Cassegrain focus. The observations were made with a narrow-

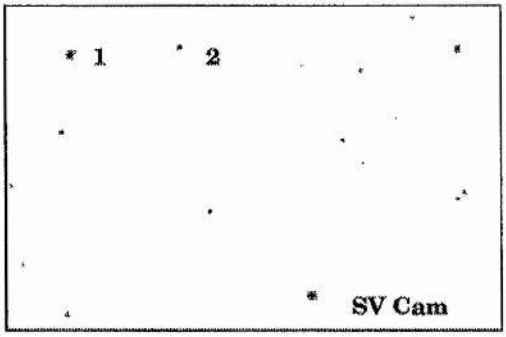

Figure 6.2: Finding charts, showing object and comparison positions for SV Cam. Differential magnitudes were computed with respect to the first comparison star, while the second star served as a check. The field size is approximately $11\times17\,\mathrm{arcmin}^2$.

band filter whose 85 Å (FWHM) bandpass is centred at 5300 Å, close to the V band. Using an exposure time of 60 s we obtained a photometric precision of ±0.003 mag in good photometric conditions. The overhead for the chip readout between 60 s observations is typically 15 s, giving an overall sampling interval of 75 s. Observations were made over a two week period centred at the time of the HST observations. The weather permitted the observation of four full primary eclipses and three full secondary eclipses over this period. The field of view containing the target and reference stars is shown in Figure 6.2.

6.4 Data Processing

6.4.1 Data reduction

Reduction of the HST data comprised calibrating the two dimensional CCD images and extracting one dimensional spectra using the standard STIS data reduction pipeline. A detailed description of this procedure is contained in the STIS handbook. This pipeline routine produces bias and dark subtracted, flat-fielded wavelength calibrated images. The auto-wavecal was disabled for these images, but instead two GO wavecals were taken per orbit. Cosmic rays were removed using an algorithm that identifies and rejects cosmic rays and other non repeatable defects by comparing successive frames. A HST spectrum of SV Cam is shown in Figure 6.3.

The ground-based photometric data were reduced using JGTPHOT, a software package developed for use with the James Gregory Telescope at St Andrews (Bell, Hilditch &

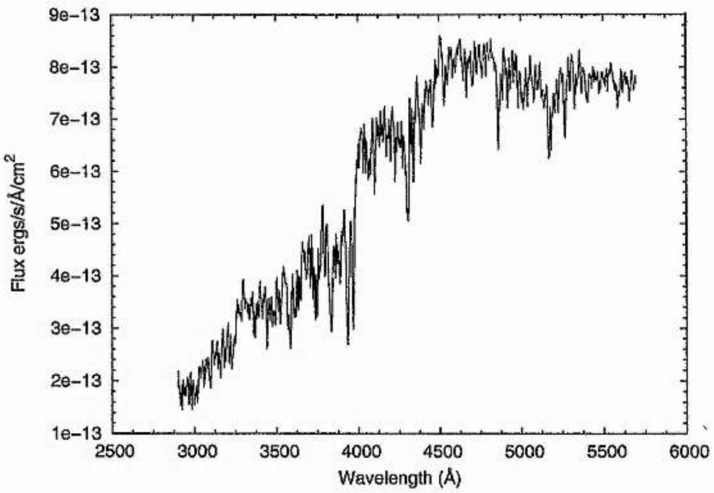

Figure 6.3: An example wavelength calibrated STIS spectrum, taken outside of the primary eclipse

Edwin 1993). The resulting in light curves are plotted as differential magnitude values with respect to the marked comparison and check stars.

6.4.2 Time Correction of HST data set

As the time of the extracted one-dimensional spectra, that is output from the standard STIS data reduction pipeline (calstis), is in UT, it is necessary to apply a further time correction to this value. The heliocentric correction due to the motion of the Earth around the Sun, and due to the orbital motion of the satellite was determined through use of the 'odelaytime' routine. To convert UT into atomic time 32 leap seconds were added, and to convert atomic time into terrestrial time 32.184 seconds were added, resulting in the correct terrestrial time value. Absolute precision in HST time is required as it is necessary to have the primary eclipse of the HST and of the ground-based observations exactly aligned.

6.4.3 Interpolation of data sets

In order to analyse the absolute spectrophotometry from STIS together with the ground-based differential photometry, it was necessary to place the magnitudes derived from the two instruments on a common magnitude scale. We constructed a synthetic filter, V_{hst}, with a bandpass and effective wavelength matching those of the filter used for the JGT

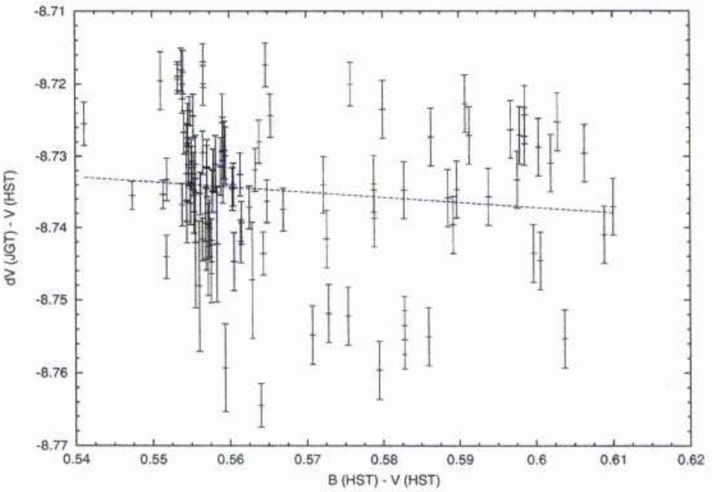

Figure 6.4: Colour-colour plot for interpolation of the HST and ground-based data sets

observations, (bandpass of 80Å and effective wavelength 5300Å) and applied it to the HST observations. Similarly we constructed a digital version of the Johnson B filter, B_{hst}.

At the time of each JGT flux measurement during primary eclipse we interpolated the V_{hst} magnitude and the $(B_{hst} - V_{hst})$ colour index from the two nearest points bracketing the same phase. The colour equation relating the two magnitude systems was then derived by a linear least-squares fit to the plot of $\delta V_{jgt} - V_{hst}$ versus $(B_{hst} - V_{hst})$, as shown in Fig. 6.5. This yielded the colour equation

$$\delta V_{jgt} - V_{hst} = \alpha(B_{hst} - V_{hst}) + \beta, \tag{6.1}$$

where the coefficient of the colour term $\alpha = -0.07 \pm 0.06$ and the zero-point $\beta = -8.694 \pm 0.033$ magnitudes. The fit is shown in Figure 6.4.

Using this linear calibration, all of the V_{hst} magnitudes were converted to the JGT system. This procedure takes account of the zero point off-set, the effect of the V_{hst} and the JGT observations having slightly different effective wavelengths, and the different spectral responses of the two filter sets and the two CCDs. The interpolated HST data set is shown in Figure 6.5 along with the JGT data.

6.5 Eclipse Mapping

The maximum entropy code DOTS was used to reconstruct the spot locations from the lightcurve of SV Cam. Included in DOTS is the ability to incorporate the surface geometry

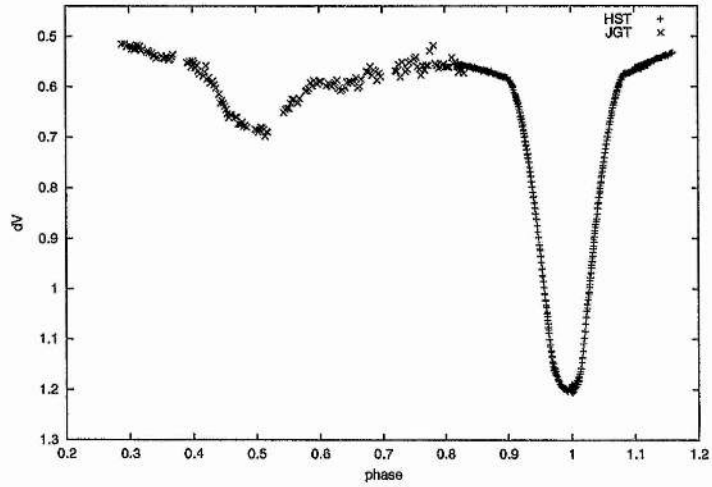

Figure 6.5: Interpolated HST data (primary eclipse) set plotted with JGT data set (secondary eclipse).

and radial velocity variations of tidally distorted close binary components (Collier Cameron 1997).

6.5.1 Image space

The maximum entropy method allows us to determine the simplest image of the primary's surface (in terms of its information content as quantified by the Shannon-Jaynes image entropy), that can reproduce, at a specified goodness of fit, the perturbations to the primary eclipse. A more detailed description is given in Section 2.4.5 and by Collier Cameron (2001).

Reference	T_p	T_s	R_p	R_s	i	q	K_1	P	γ	S/P	Spectral Type
Lehmann, Hempelmann & Wolter (2002)	6000	4400	1.18(2)	0.76	90.0	0.642	120.5	0.5930718	-13.9	S	G0V+K6V
Rucinski et al. (2002)					90.0	0.641	121.86	0.593073	-9.13	S	G2V(pri+sec)
Kjurkchieva, Marchev & Zola (2002)	6440	5386	1.38(5)	0.94(6)		0.593	123.1			S	F5V+G8V
Albayrak et al. (2001) (a)	6440	4467	1.38(2)	0.87(2)	89.6	0.56	118.5	0.593071		P	F8V+K6V
(b)	6200	4377	"	"	"	"	"	"	"	"	F5V+K6V
Pojmanski (1998)	6440	5270	1.25	0.8	90.0	0.56(4)	118(2).5	0.593071	-13.7 (1.5)	S	F5V+K0V
Zeilik et al. (1988)	5800	4300	1.17	0.74	89.5					P	G3V
Budding & Zeilik (1987)	5750	4500	1.16	0.77	90.0	0.72		0.593		P	G3V+K4
Popper (1996)	5700	5600				0.59				S	G3V+G5V
Patkos & Hempelmann (1994)	5750	4500	1.18	0.75				0.59		P	G2/3V+K4/5
Rainger, Hilditch & Edwin (1991)	5800	4700			90.	0.7	122(1.5).3		-11.2	S	G2/3V+K4V
Hilditch, McLean & Harland (1979)	5800	4140	1.224	0.864	80.0	0.7		0.59307155		P	G3V+K4V

Table 6.2: Summary of observed stellar parameters for SV Cam from the literature.

6.5.2 Image reconstruction

It is important not to overfit χ^2 during the reconstruction, as this can result in an ill-fitting photometric fit and artifacts on the final spot map. The number of iterations was set to 25, as through rigorous testing we found this to be the value where the final image did not contain any distortions due to ill fitting.

6.6 Geometric Parameters

The success of a surface image reconstruction depends largely on a correct determination of the geometric parameters of the binary system (Vincent et al 1993). Independent reconstructions for the starspot parameters and the geometric parameters of the system, are susceptible to the distortions in the lightcurve yielding the wrong system parameters or vice versa. If the system parameters are wrong, in general a satisfactory fit to the data is only obtained by increasing the amount of structure in the stellar surface brightness distribution, usually leading to a greater total spot area than is present when the correct geometric parameters are used.

The principal parameters that affect the shape of the light-curve of an unspotted star are the relative temperatures, the radii of the two stars and the system inclination. The relative surface brightnesses of the two components determine the relative depths of the primary and secondary eclipses. The radii of the two stars and the binary system inclination are related to each other by the orbital phases at which the four contact points occur. These relations are further complicated by the presence of starspots which in general have the affect of altering the depth of the eclipses and making the contact points asymmetrical.

SV Cam has been the subject of numerous photometric and spectroscopic studies. Despite this, there still does not yet exist a established and reliable set of stellar parameters. The various published permutations of stellar parameters that can be found for SV Cam in the literature are summarised in Table 6.2. A discussion of the individual merits of each set of binary system parameters is beyond the scope of this paper. Given the wide range of geometric parameters available for SV Cam, it was necessary to refine a set of parameters that would give an optimal fit to our data. We assumed that the mass ratio

Ephemeris	52214.34475 (MJD)
T_{pri}	6038 ±8 K
T_{sec}	4804 ±143 K
R_{pri}	1.238 ±0.001 $R_\odot$
R_{sec}	0.794 ±0.001 $R_\odot$
q	0.64 ±0.03
i	90 ±3°

Table 6.3: Geometric binary system parameters computed for SV Cam. The primary and secondary temperatures are taken from Jeffers et al. (2004b) (Chapter 5), and the mass ratio, q, is from Rucinski et al. (2002).

is known, and adopted the the value $q = 0.641$ determined by Rucinski et al. (2002).

6.6.1 Temperature

Jeffers et al. (2004b) (Chapter 5) determined the temperature of the primary and secondary components of SV Cam using PHOENIX model atmosphere spectra. Model atmospheres, ranging in temperature from 5600 K to 6500 K in 100 K steps, were fitted to the spectrum of the primary using χ^2 minimisation. The minimum χ^2 value corresponds to a temperature of 6038±8 K and 4804±143 K for the primary and secondary stars respectively.

6.6.2 Radii

The radii for the primary and secondary stars were determined using the robust grid search method. This method uses a grid of radii as input to DoTS ranging from 1.17 $R_\odot$ to 1.26 $R_\odot$ for the primary star, and 0.73 $R_\odot$ to 0.82 $R_\odot$ for the secondary star in 0.005 $R_\odot$ intervals.

For each grid point a model with the specified set of geometric parameters was iterated 25 times to obtain the lowest value of the reduced χ^2. The inclination was not included as it scales as $\sin^{-1}$, implying a negligible difference between inclinations of 90° and 85°.

The results for the χ^2 minimisation are shown in Figure 6.6 in the form of a contour plot. The minimum χ^2 value occurs at 1.238 ± 0.001 $R_\odot$ and 0.794 ± 0.001 $R_\odot$ for the

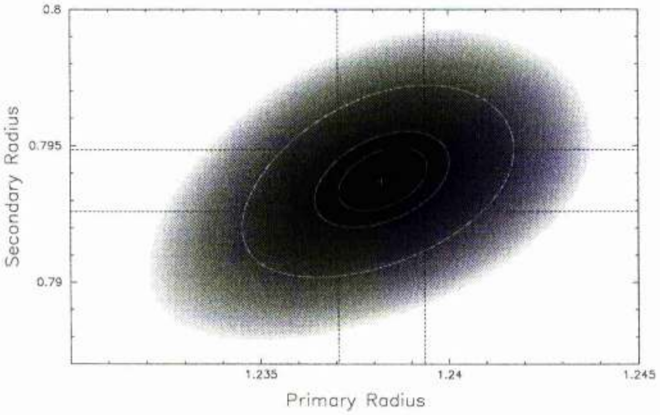

Figure 6.6: Contour plot of the χ^2 landscape for the primary and secondary radii. From the centre of the plot, the first contour ellipse is the 1 parameter 1σ confidence limit at 63.8%, the second contour ellipse is the 2 paramter 1σ confidence limit at 63.8%, and the third contour ellipse is the 2 parameter 2.6σ confidence limit at 99%.

primary and secondary stars respectively. The best fitting stellar parameters for the combined JGT and HST data sets are summarised in Table 6.3.

6.7 Eclipse Maps of SV Cam

The primary star dominates the light of the binary system, and shows strong rotational modulation attributed to the presence of starspots. The cooler secondary acts as a dark occulting disc scanning across the equatorial region of the primary during primary eclipse.

A first visual analysis of the photometric lightcurve (from both the JGT and the HST data sets) shows that there are large spots present at the quadratures, and that there is time variable structure present in the base of the eclipse. It is this time variable structure that contains the information regarding the sizes and the locations of spots on the surface of the primary.

The resulting Maximum Entropy fit to the lightcurve, using the stellar parameters as previously defined are shown in Figure 6.7. The stellar surface image that results from these fits is shown in Figure 6.8. The observed data minus computed lightcurve residuals are shown in Figure 6.9 in enlarged form covering just the HST primary eclipse data.

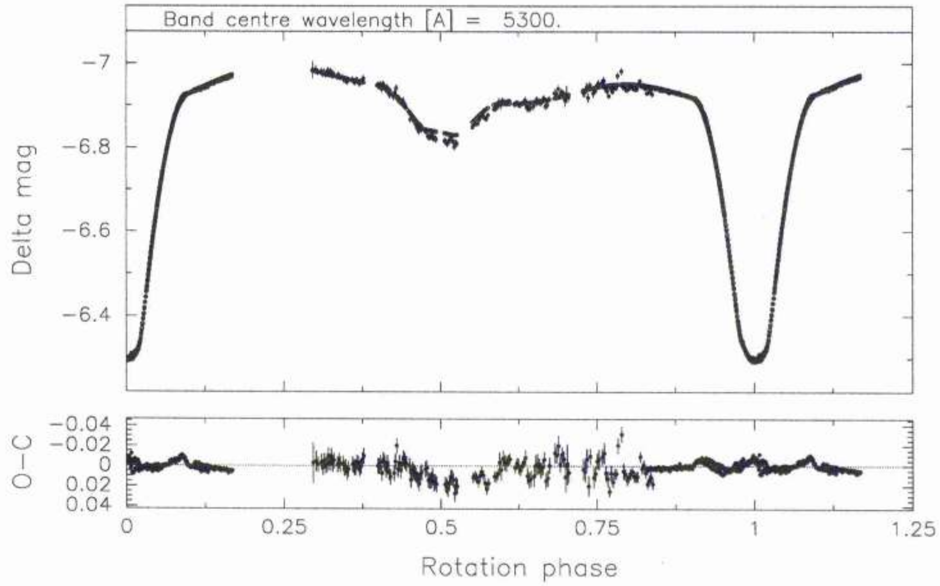

Figure 6.7: Combined HST and JGT lightcurves, with a Maximum Entropy fit.

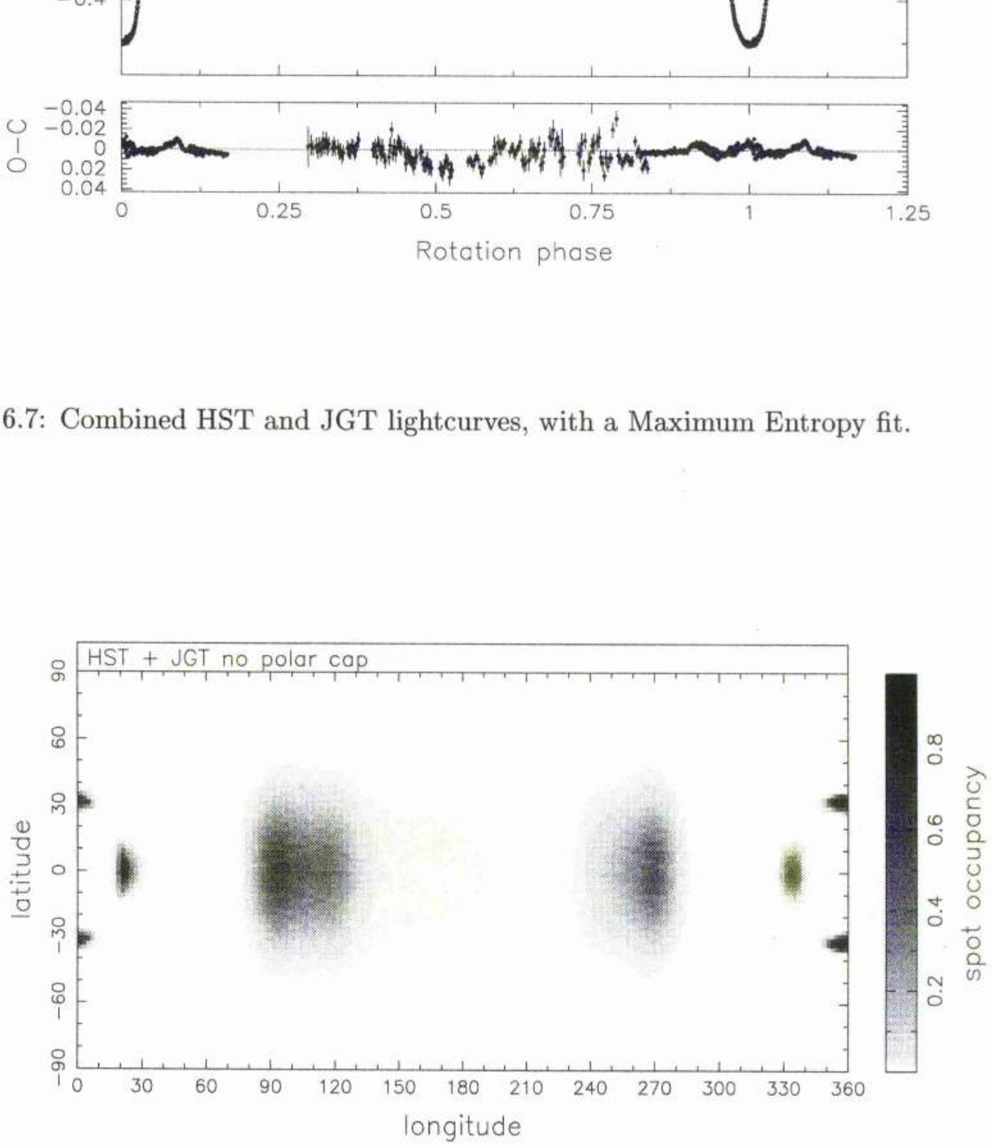

Figure 6.8: The final spot map of SV Cam (HST + JGT data). Note that phase runs in reverse to longitude.

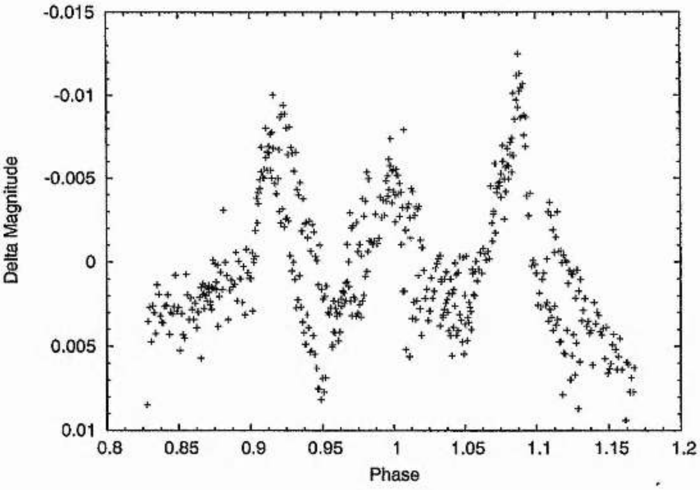

Figure 6.9: Observed minus Computed residuals with no polar cap (HST data only).

6.7.1 Residual profiles

The final model lightcurve of the system parameters gives a close fit to the data. When the modelled light-curve is subtracted from the observed data the residuals are symmetric about phase 1, and have two large peaks that occur at the first and fourth contact points either side of the primary eclipse (Figure 6.9). Given the location of these peaks, an obvious explanation would be that the radius of either of the two stars has been incorrectly determined so that it is necessary for the Max Ent reconstructions to place additional structure on the primary to compensate for this. However, through a meticulous determination of the stellar parameters, as described in section 6.2.2 this can be eliminated. The presence of a polar cap on the surface of SV Cam would have the effect of increasing the depth of the primary eclipse and hence distorting the fit to the lightcurve.

6.8 Polar Spot

As previously described in section 5.5, Jeffers et al. (2004b) (Chapter 5) determined the temperatures of the two stars using best-fitting PHOENIX model atmospheres. Jeffers et al. (2004b) (Chapter 5) found that the primary's surface flux is approx 28% lower than predicted by a PHOENIX model atmosphere at the best fitting effective temperature. Even taking into account the spot distributions as shown in Figure 6.8, this flux deficit can only be accounted for if the primary star's surface is peppered with unresolved spots. As these spots are not resolvable using the eclipse-mapping technique they will influence the

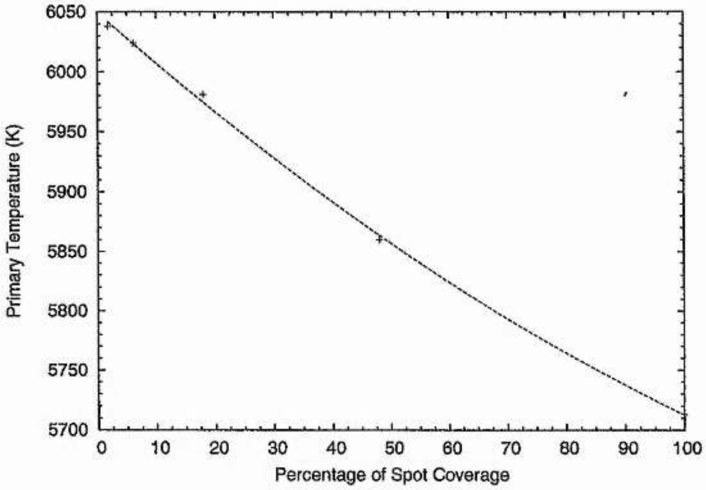

Figure 6.10: The decrease of primary star's photospheric temperature as a function of percentage of spot coverage on its surface.

Ephemeris	52214.34475 (MJD)
T_{pri}	5935 ±38 K
T_{sec}	4804 ±143 K
R_{pri}	1.235 ±0.003 $R_{\odot}$
R_{sec}	0.727 ±0.003 $R_{\odot}$
q	0.64 ±0.03
i	90 ±3°
Polar Spot	46±8°

Table 6.4: Geometric binary system parameters computed for SV Cam with a reduced photospheric temperature due to the star being peppered with small spots, and increased radii due to the presence of a polar cap.

apparent photospheric temperature of the star. The presence of many small spots decreases the flux deficit during the eclipse at all wavelengths, and can lead to a underestimate of the photospheric temperature.

To determine the reduced photospheric temperature, we extend the work of Jeffers (2004) (Chapter 4). In this work an extrapolated solar spot size distribution is applied to an immaculate SV Cam, for 1.8%, 6.1%, 18%, 48% and 100% area filling factors of spots. Each of these spot distributions are modelled as a photometric lightcurve and are reconstructed using eclipse mapping. To obtain a satisfactory fit to the lightcurve it was necessary to reduce the photospheric temperature to values as shown in Figure 6.10. A quadratic fit to these points gives a temperature for 28% spottedness of 5935 K.

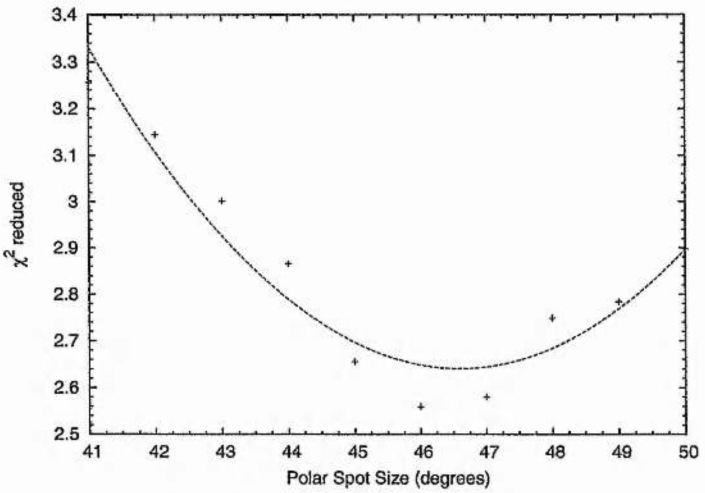

Figure 6.11: Quadratic fit to the variation of χ^2 as a function of polar spot size.

Jeffers et al. (2004b) (Chapter 5) also found that when the 28% spot coverage is applied to the whole star there is an additional 12.5% flux deficit, which can only be explained if there is a dark polar spot on the primary star. We include this in our analysis by extending the 2-dimensional grid search in section 6.2.2 to a 3-dimensional grid search including the polar spot size from 35° to 50°. For each polar spot size the minimum primary and secondary radii are determined using a χ^2 contour map. These minimum χ^2 values are plotted as a function of polar spot size in Figure 6.11. The best fitting polar cap size, 46.49° was determined from the minimum of a quadratic function fitted to these points. The grid search of radii is repeated using a fixed value for the polar spot size. The results for the χ^2 minimisation are shown as a contour map in Figure 6.12.

These stellar parameters are used to create a Maximum Entropy image (Figure 6.14 and 6.13), which is similar to that shown in Figure 6.8. The spot feature at 0° and 360° is not an artifact as it is in the eclipse path of the secondary, but results from time variable structure in the base of the primary eclipse. The spot feature at 25° and 335° in Figure 6.8 has disappeared due to the correct determination of the stellar radii.

The observed data minus computed lightcurve residuals, as shown in Figure 6.15, are significantly flatter than those shown in Figure 6.9. The reduced χ^2 value after 25 iterations was 2.55, which is slightly reduced from the value of 3.55 obtained without a polar spot. This shows that the presence of a polar cap has a significant influence on the O-C residuals.

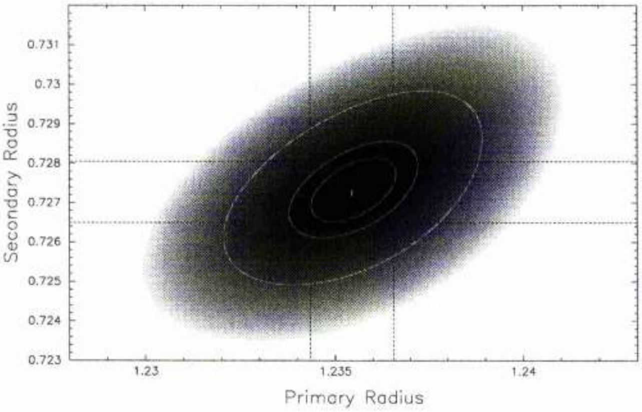

Figure 6.12: Contour plot of the χ^2 landscape for the primary and secondary radii with a 46.69° polar spot. From the centre of the plot, the first contour ellipse is the 1 parameter 1σ confidence limit at 63.8%, the second contour ellipse is the 2 paramter 1σ confidence limit at 63.8%, and the third contour ellipse is the 2 parameter 2.6σ confidence limit at 99%.

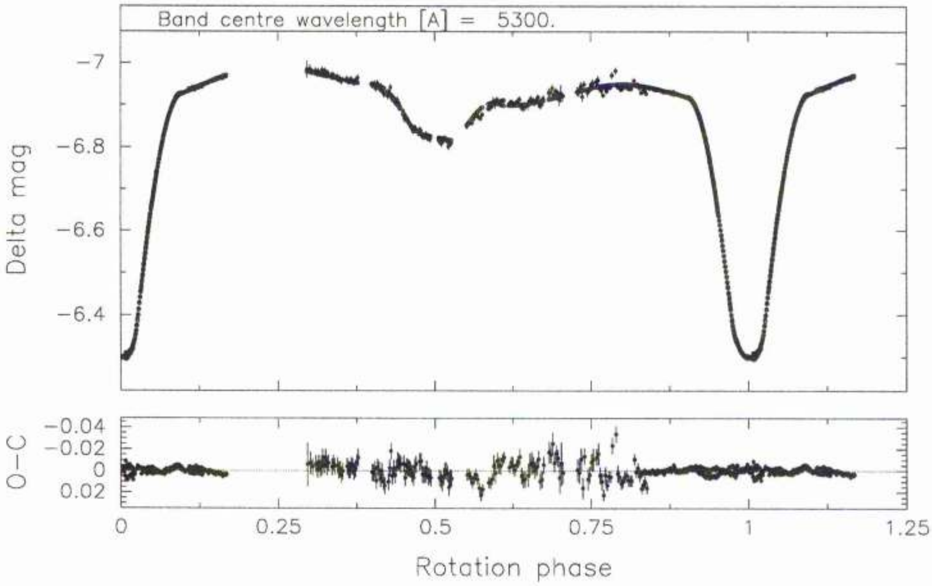

Figure 6.13: Combined HST and JGT lightcurves, with a Maximum Entropy fit with a polar cap and reduced photospheric temperature included.

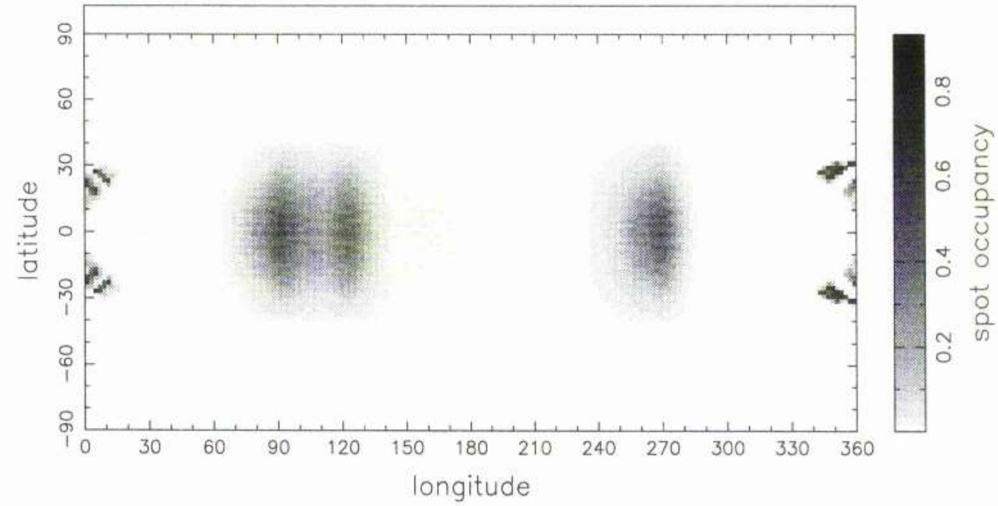

Figure 6.14: The final spot map of SV Cam (HST + JGT data) with a polar cap and reduced photospheric temperature. Note that phase runs in reverse to longitude, and that the polar cap extends to 46°, even though it is not shown on this image.

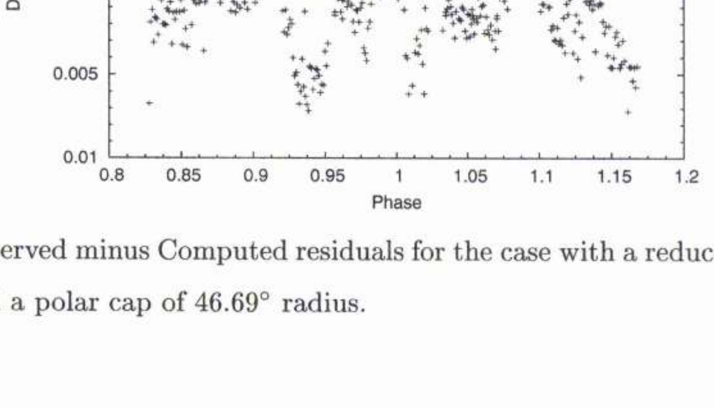

Figure 6.15: Observed minus Computed residuals for the case with a reduced photospheric temperature and a polar cap of 46.69° radius.

6.9 Discussion and Conclusions

We have used eclipse mapping, based on the maximum entropy method to recover images of the visual surface brightness distribution of the primary component of the RS CVn eclipsing binary SV Cam. The O-C residuals of the fit to the lightcurve show strong peaks at the four contact points. These features can be removed from the O-C lightcurve by the reduction of the photospheric temperature and the presence of a polar spot.

Previous work by Jeffers et al. (2004b) (Chapter 5) has shown that the eclipsed surface of SV Cam is peppered with 28% spots that are too small to be resolved using eclipse mapping. The presence of many spots will have the effect of decreasing the depth of the primary eclipse, giving the appearance of a lower photospheric temperature of 5935 K as opposed to 6038 K for an immaculate primary star. In addition to the 28% spot coverage, Jeffers et al. (2004b) (Chapter 5) showed that the uneclipsed regions have an additional 12.5% spot coverage that can only be accounted for by the presence of high latitude or polar spots. As polar spots are common and long-lived features on RS CVns, (examples include, HR 1099 (Vogt et al. 1999; Petit, Donati & Collier Cameron 2002), EI Eri (Hatzes & Vogt 1992; Washuettl, Strassmeier & Collier-Cameron 2001), UZ Lib (Oláh, Strassmeier & Weber 2002), HU Vir (Strassmeier 1994; Hatzes 1998), V1355 Ori (Strassmeier 2000) and IL Hya (Weber & Strassmeier 1998)) we deduce that the uneclipsed flux deficit results from a polar spot. Jeffers et al. (2004b) (Chapter 5) concluded that the polar spot is of 42±6° radius, which is in good agreement with the independently calculated value of this work, 46±8° radius. Both of these values assume a uniform polar spot which is possibly an over simplification.

The reliability of eclipse-mapping techniques has been discussed by Jeffers (2004), where an extrapolated solar size distribution, that comprises many small spots, is applied to a non-spotted SV Cam. Photometric lightcurves are modelled from these data and used as input to the DoTS eclipse mapping code. The surface brightness distribution reconstructed from these lightcurves showed distinctive spots on the primary star at its quadrature points. This may cast some doubt on the reliability of the surface brightness image presented here (Figure 6.8). However, the photometric lightcurve shows an asymmetry in the lightcurve as shown in Figure 6.7 which is consistent with the Max Ent image in Figure 6.8. The asymmetry in the lightcurve could also be explained by one half of the primary star possessing a greater concentration of spots than the other half of the star.

As described above, Jeffers et al. (2004b) (Chapter 5) determined the surface fraction of spot coverage on SV Cam to be 28%. Comparing this spot filling area with that in Figure 6.8, shows that there are a large number of spots that remain unresolved. This could result from the eclipse mapping routine interpreting small scale variations in the lightcurve as noise. Unfitted spots would then be responsible for the remaining fluctuations in the O-C residual lightcurve as shown in Figure 6.15. A 0.005 change in magnitude as shown in Figure 6.15 would result in 14% of the area of the annulus around the secondary being spotted. However, the remaining structure in the O-C residual could result from an incorrect value of the limb darkening or the presence of plage on the primary star's surface, which required further investigation.

The high total spot coverage on SV Cam's primary star has important structural implications. As investigated by Spruit & Weiss (1986), a star with high spot coverage will, over thermal timescales, readjust its structure to compensate in radius and temperature. For example the primary star's radius is 10% larger than expected for its spectral type, and provides an explanation as to the variation in binary system parameters as shown in Table 6.2.

The addition of a polar spot and the reduction of the photospheric temperature has a negligible influence on the empirically determined radius of the primary star, but a more significant influence on the secondary, decreasing it from $0.794\pm0.003\ R_\odot$ to $0.727\pm0.003\ R_\odot$. The presence of a polar spot will increase the depth of the lightcurve. The binary system compensates for this by making the secondary star smaller, and consequently it eclipses less light. The surface brightness image reconstructed with the refined binary system parameters has reduced surface structure compared to the image reconstructed with the original parameters. This is noticeable at longitudes 25° and 335°, where the small spots have disappeared with the refined binary system parameters. The structures at longitudes 0° and 360° are not artifacts of the eclipse mapping technique as they are in the eclipse path of the secondary, but result from time variable structure in the base of the primary eclipse.

CHAPTER 7

Modelling of HST eclipsing-binary lightcurves using PHOENIX and ATLAS model atmospheres

7.1 Abstract

The variation of the specific intensity across the stellar disc has an important influence in determining the contact points of a binary system lightcurve. We use the PHOENIX and ATLAS model atmospheres to model lightcurves derived from high precision (S:N 5000) HST data of the eclipsing binary SV Cam. The observations span 5 days in November 2001, and comprise 3 primary eclipses over 9 HST orbits. The fit is determined using the first derivative of the lightcurve, which we show to be sensitive to the limb-darkening profile very close to the limb of the primary star. The wavelength dependence of the limb darkening is determined by splitting the observed and model lightcurves into 10 wavelength bands. Between second and third contact, the PHOENIX atmosphere gives a better fit at shorter and longer wavelengths, while the ATLAS atmosphere gives the better fit to the eclipse profile at central wavelengths. At partial phases of the eclipse the PHOENIX atmosphere gives a better fit overall. We investigate the usefulness of the second derivative of the light-curve for measuring the sharpness of the primary's limb, but find that the data are too noisy to permit a quantitative analysis.

7.2 Introduction

Limb darkening effects in stellar atmospheres have important implications throughout stellar astrophysics where a determination of the surface brightness distribution is important.

Recent work using Doppler imaging and micro-lensing events has shown that commonly-used limb darkening laws fail to match stellar observations at the limb of the star (Barnes et al. 2004, Thurl, Sackett & Hauschildt 2004). The problem is that the specific intensity appears to drop smoothly to zero near the stellar limb. High inclination eclipsing binary systems can also be used as a probe to determine the variation of specific intensity at the stellar limb. If limb darkening showed a smooth transition in specific intensity at the limb of the star, the contact points of eclipses would appear less abrupt and slightly displaced in phase relative to models with limb darkening laws derived from plane-parallel atmospheres, where the cutoff is very sharp. The sharp cutoff in plane parallel atmospheres results from the optical depth of the rays being infinite at the limb.

In November 2001 we were awarded 9 orbits of HST/STIS time to eclipse-map the inner face of the F9V primary of the totally eclipsing binary SV Cam. SV Cam is a rapidly rotating RSCVn binary with a period of 0.59d. We obtained spectrophotometric lightcurves of 3 primary eclipses with a signal-to-noise ratio of 5000. The first analysis of this data, by Jeffers et al. (2004a), determined the radii of the primary and secondary stars. When the resulting lightcurve was subtracted from the observed data, the residual lightcurve showed strong peaks at phases of contact. Jeffers et al. (2004a) then showed that these mismatches are reduced significantly, but not eliminated, when a polar cap is imposed on the image. The phases of the contact points on the modelled lightcurve depend strongly on the variation of specific intensity at the limb of the star and hence whether the model atmosphere used to generate these lightcurves uses spherical or plane-parallel atmospheres.

As there is a significant temperature difference between the primary and secondary stars, the secondary star acts as a dark occulting disc as it eclipses the primary star. The variation of brightness as a function of phase reflects the degree of limb darkening on the primary star. In this paper we determine the best fitting model atmosphere by fitting the models to the brightness variations as the secondary scans the inner face of the primary star, using the first and second derivatives of the HST in 10 wavelength bands.

7.3 Model Atmospheres

In this paper, two well established stellar atmosphere codes are used; the PHOENIX model atmosphere code (Hauschildt et al. 1999) that uses spherical atmospheres and the ATLAS model atmosphere code (Kurucz 1993) that uses plane parallel atmospheres.

7.3.1 ATLAS

We use the plane-parallel ATLAS9 model atmospheres from the Kurucz CD-ROMS (Kurucz 1993). We integrate the intensity values over the wavelength range of our observations 2900Å to 5700Å. We use temperature models from 3500 K to 6500 K, with 250 K interval, across 17 limb angles. The limb angle μ is defined by $\mu = \cos\theta$, where θ is the angle between the line of sight and the emergent flux. The treatment of convection is based on the mixing length theory. The variation of specific intensity, i.e. at μ=1, as a function of wavelength and limb angle with respect to the disc, is shown in Figure 7.1.

7.3.2 PHOENIX

The general input physics set-up of the PHOENIX model atmosphere code is discussed in Hauschildt et al. (1999). The main advantage of using this code is that it is based on spherical geometry (spherical radiative transfer) LTE rather than traditional plane-parallel structure.

The synthetic spectra are based on an extension of the grid of PHOENIX model atmospheres described by Allard, Hauschildt & Schweitzer (2000). This extended grid includes surface gravities larger than $\log(g) > 3.0$ needed for main sequence stars. These models are as described by Hauschildt et al. (1999), but include an updated molecular line list. The models are computed in spherical geometry with full atomic and molecular line blanketing using solar elemental abundances. In these models, the stellar mass is 0.5 $M_\odot$ and the convection treatment assumes a mixing-length to pressure scale height ratio of 2. There are 117 synthetic spectra in total. The effective temperature runs from 2700 K to 6500 K in 100 K steps at three surface gravities: $\log(g) = 4.0$, 4.5, and 5.0. The wavelength resolution of these synthetic spectra is 1Å.

The variation of specific intensity as a function of limb angle is shown in Figure 7.1.

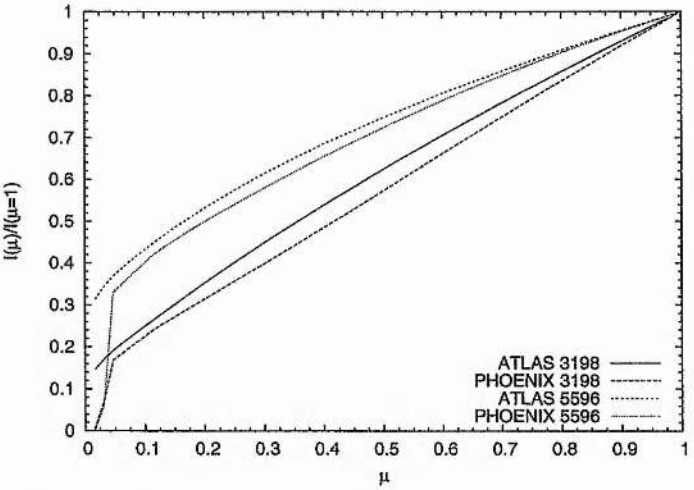

Figure 7.1: The variation of continuum specific intensity across the stellar disc as a function of wavelength for the longest (5596Å) and the shortest (3198Å) wavelengths in this analysis.

The dramatic difference between the PHOENIX and the ATLAS model atmospheres at the limb of the star results primarily from the effects of spherical geometry of the PHOENIX model. In models using spherical geometry, there is a finite optical depth for rays close to the limb, while with plane parallel models the optical depth of the rays is infinite at the limb providing significant intensities down to μ=0.

7.3.3 Model lightcurves

We use the eclipse-mapping code DoTS (Collier Cameron 1997) to model the primary eclipse lightcurve for each model atmosphere, and to determine which model atmosphere best fits the complete HST lightcurve. The input data to each model comprises: the variation of the continuum specific intensity as a function of limb angle, as shown in Figure 7.1 for both model atmospheres considered; the primary and secondary radii; a reduced primary photospheric temperature and polar spot.

We include a reduced photospheric temperature to account for a stellar surface that is peppered with small spots which are too small to be resolved through eclipse mapping. Following the results of Jeffers et al. (2004a) we include a polar cap in the modelled lightcurve to optimise the fit of the lightcurve to the data. The binary system parameters are summarised in Table 7.2.

Visit	Obs. Date	UT Start	UT End	Exposure Time(s)	No of Frames
1	01 November 2001	20:55:56	01:00:17	30	165
2	03 November 2001	14:34:29	18:38:21	30	165
3	05 November 2001	09:49:17	13:52:22	30	165

Table 7.1: HST Observations of SV Cam

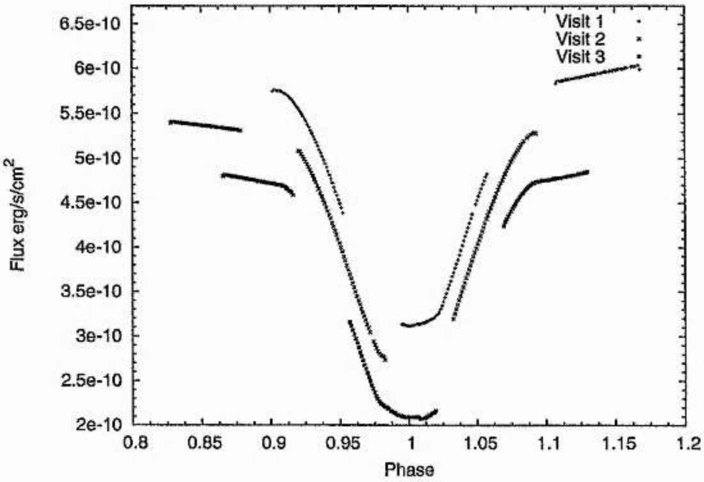

Figure 7.2: The comprising sections of the primary eclipse from each of the 3 HST visits, with an off-set of 5 $\times 10^{-11}$ ergs/s/cm^2 for clarity.

7.4 HST Observations

Three primary eclipses of SV Cam were observed by the HST, using the Space Telescope Imaging Spectrograph with the G430L grating. The observations used 9 spacecraft orbits and spanned 5 days at 2 day intervals from 1-5 November 2001 as shown in Table 7.1. Summing the recorded counts over the observed wavelength range 2900 Å to 5700 Å yields a photometric lightcurve. Figure 7.2 shows the photometry of the 3 eclipses observed during the 9 orbits. The observations have a cadence of 40s and a photometric precision of 0.0002 magnitudes (S:N 5000) per 30 s exposure. The observations and the data reduction method are explained in greater detail in Jeffers et al. (2004a).

7.5 Wavelength Dependence of Limb Darkening

The variation of the HST lightcurve with wavelength was determined by phasing the three primary eclipses together and dividing each spectrum into 10 bands of equal flux, as shown

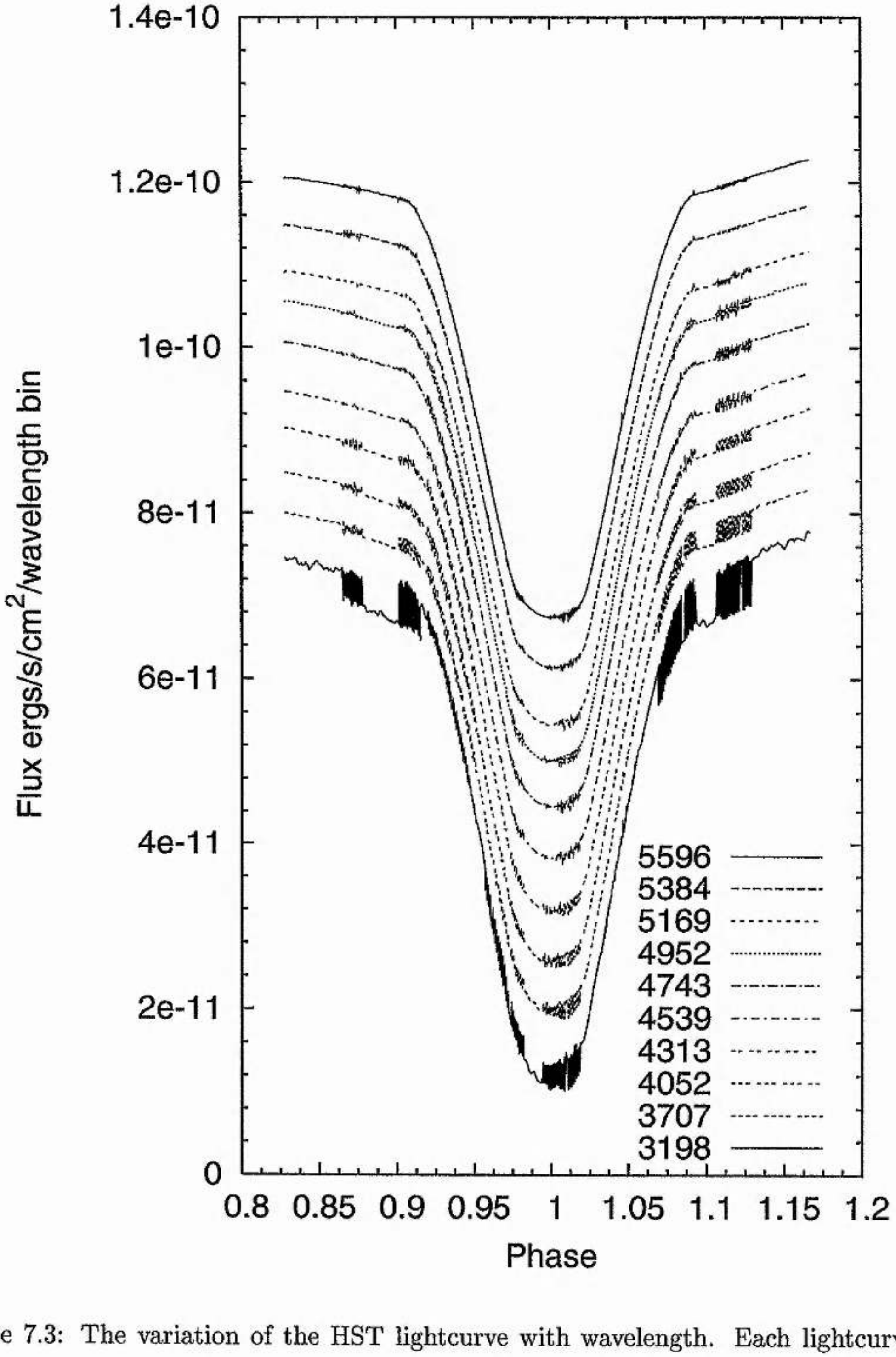

Figure 7.3: The variation of the HST lightcurve with wavelength. Each lightcurve has been plotted with an offset of 5×10^{-12} ergs/s/Å/cm^2 from the lightcurve at the top of the plot (5596 Å).

Law/Model	Temperature (K)	Primary Radius ($r_\odot$)	Secondary Radius ($r_\odot$)	Polar Spot Size (degrees)
PHOENIX	5935 ±28 K	1.235 ± 0.003	0.727 ± 0.003	46.49 ± 8
ATLAS	5927 ±31 K	1.236 ± 0.003	0.727 ± 0.002	46.66 ± 8

Table 7.2: Geometric binary system parameters computed for SV Cam with a reduced photospheric temperature due to the star being peppered with small spots, and increased radii due to the presence of a polar cap.

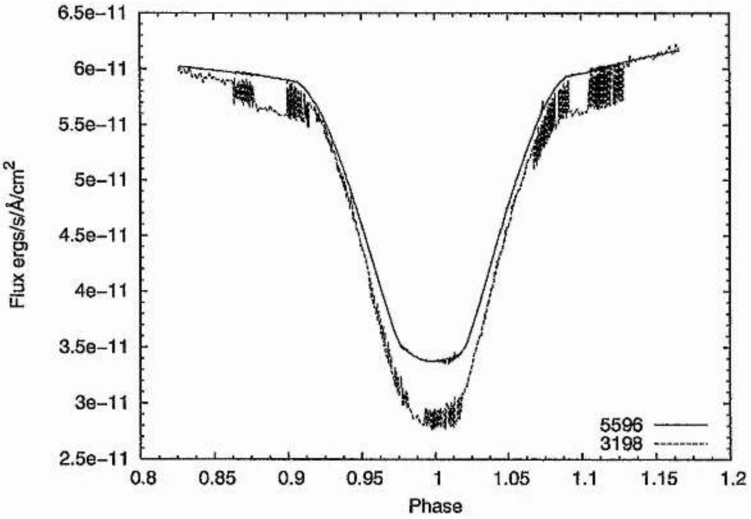

Figure 7.4: HST lightcurves with the longest (5596 Å) and shortest wavelengths (3198 Å), showing the variation of limb darkening with wavelength and the temporal evolution of bright magnetic features over the 5 day timespan our observations. The variation is of the order of 5%.

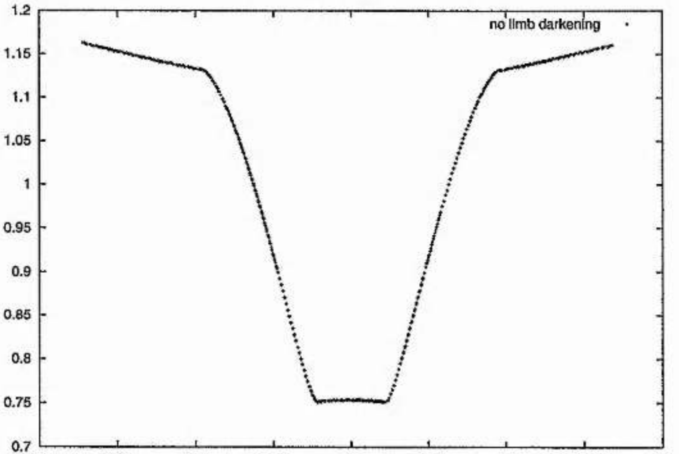

Figure 7.5: Modelled primary eclipse lightcurves, constructed with the same stellar parameters as in Figure 7.4, but with no limb darkening.

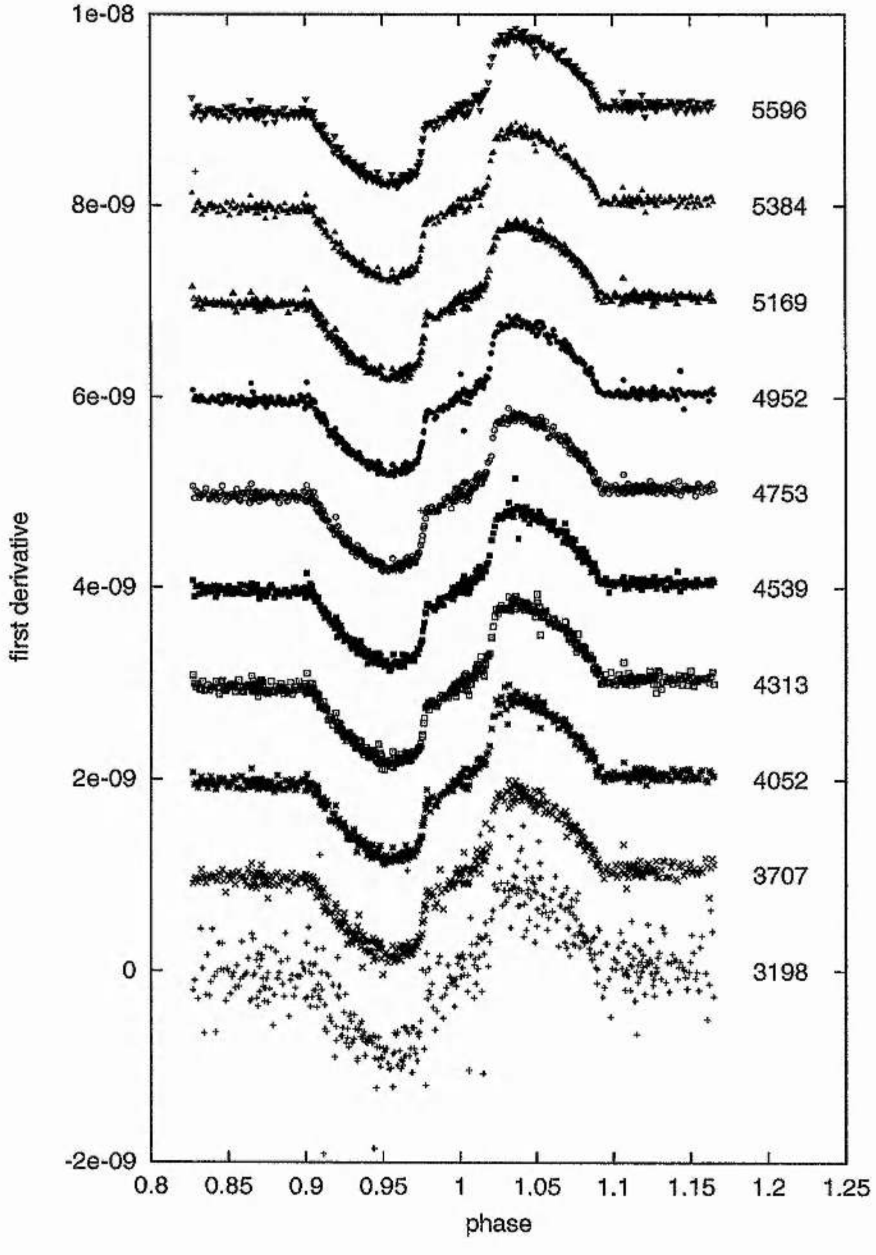

Figure 7.6: First derivative profiles for each of the 10 HST lightcurves as plotted in Figure 7.3. The presence of a bright magnetic feature is the cause of the variation in waveband 3198Å.

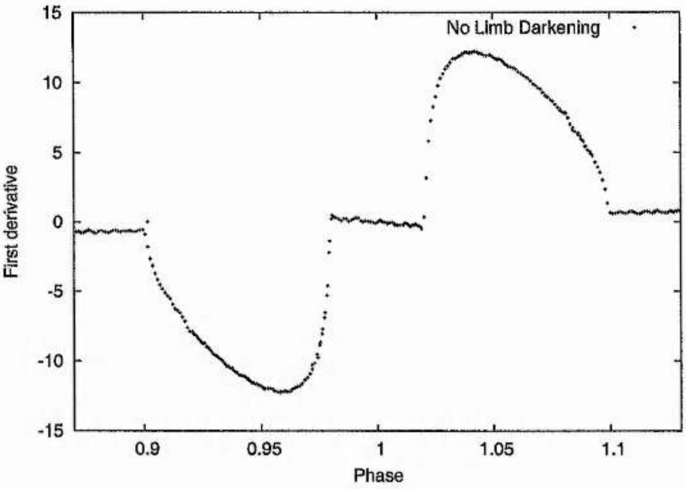

Figure 7.7: First derivative profiles, constructed with the same stellar parameters as in Figure 7.6, but with no limb darkening.

in Figure 7.3. The increased fluctuations at shorter wavelengths are consistent with the presence of bright magnetic activity, as they are strongest in the bluest wavelength band. The fluctuations at blue wavelengths are not a short-timescale phenomenon, but rather a mismatch in flux levels arising from a change in the star's UV flux from second to third visit.

The curvature of the eclipse profile between second and third contact illustrates clearly that limb darkening increases towards shorter wavelengths. It is consistent with published values of limb darkening (Claret 2000) that indicate the limb darkening should increase at shorter wavelengths. Both the brightness variation and the variation of the limb darkening with wavelength are illustrated by plotting the bluest and reddest wavelength bands, as shown in Figure 7.4.

7.6 First Derivative Profiles of Lightcurves

7.6.1 Basic properties

As the primary star dominates the light of the binary system, the cooler secondary acts as a dark occulting disc scanning across the equatorial region of the primary during eclipse. The variation of the specific intensity as a function of limb angle across the primary star shows the degree of limb darkening. This is illustrated by comparing a modelled lightcurve

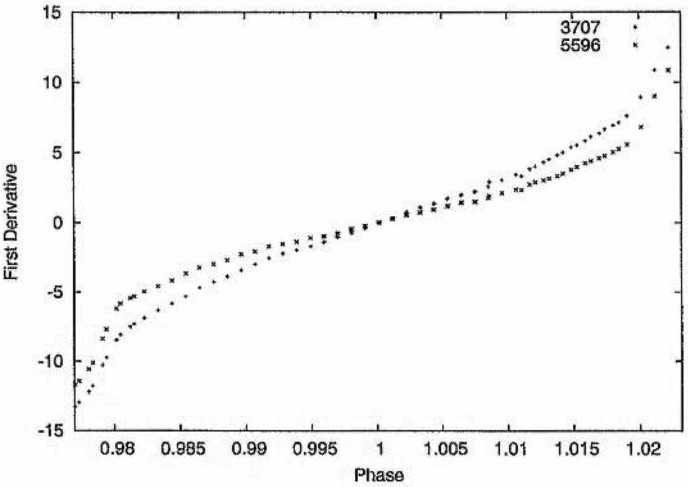

Figure 7.8: First derivative profiles of the observed lightcurve of wavelengths 5596 Å and 3707 Å for total eclipse, i.e. between second and third contact, showing the variation of limb darkening with wavelength.

with no limb darkening as shown in Figure 7.5, with the observed lightcurve of Figure 7.4.

To ascertain the optimally fitting model atmosphere to the HST lightcurves it is necessary to examine the degree of curvature in the eclipse profile. We use the first derivative, with respect to phase, of the lightcurves to determine the rate of change of the eclipsed flux with phase. The profiles of the first derivative for each of the 10 HST wavebands are shown in Figure 7.6. The first contact point is at phase 0.906±0.003, the second contact point is at phase 0.977±0.003, the third contact point is at 1.023±0.003, and the fourth contact point is at 1.093±0.003. The gradient of the first derivative profile between second and third contact points is indicative of the degree of limb darkening in the lightcurve. In the first derivative of the model with no limb darkening, this region the profile is flat (Figure 7.7). The variation of limb darkening with wavelength is illustrated in Figure 7.8, where the first derivative lightcurves from the longest wavelength (5596 Å) and the second shortest wavelength (3707 Å) are plotted between the second and third contact points. The first derivative profile of the shortest wavelength contains too much deviation, caused by small scale flickering in the data, to provide a clear example.

The variation of the first derivative profile with wavelength is also visible in the profile using the PHOENIX model atmosphere, as shown in Figure 7.9. In contrast to this Figure 7.10 shows the same first derivative profiles based on the ATLAS model atmosphere. In the ATLAS first derivative profiles there is more variation between the two

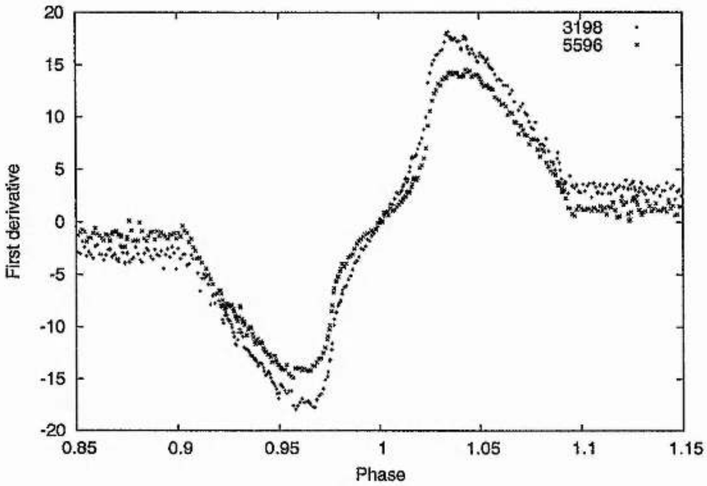

Figure 7.9: First derivative profiles for the longest (5596 Å) and shortest wavelengths (3198 Å), as plotted in Figure 7.6, using PHOENIX spherical model atmospheres.

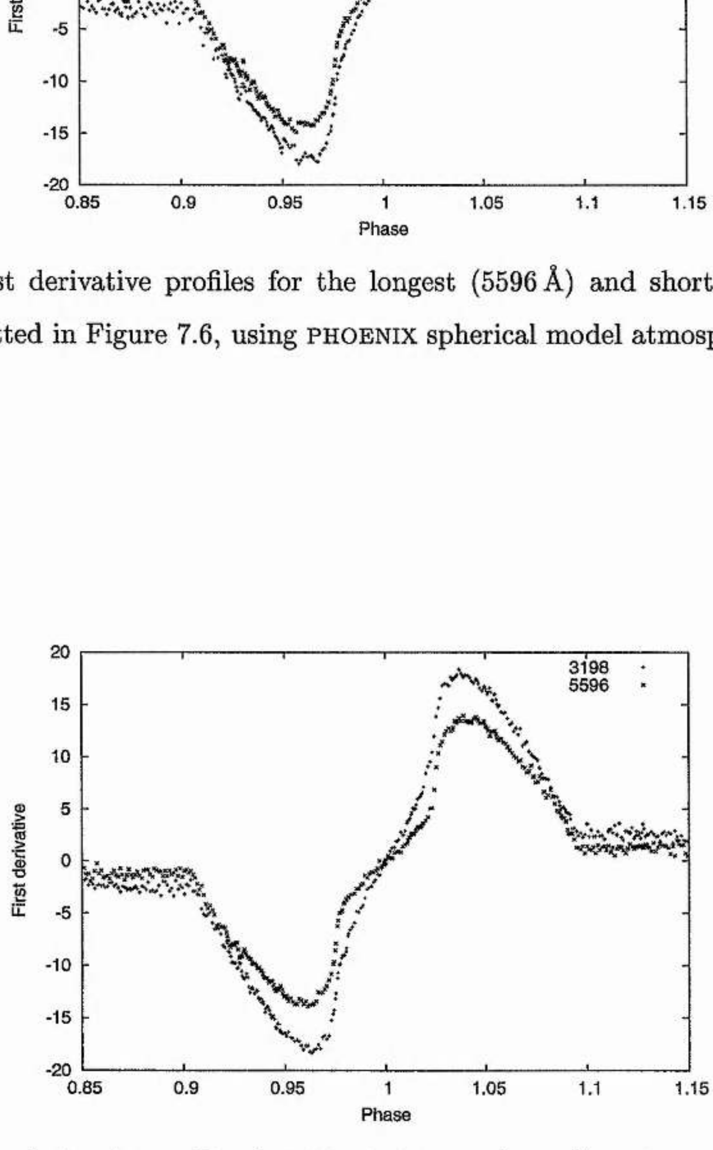

Figure 7.10: First derivative profiles for with the longest (5596 Å) and shortest wavelengths (3198 Å), using ATLAS plane parallel model atmospheres.

Wavelength	PHOENIX(1)	ATLAS(1)	PHOENIX(2)	ATLAS(2)
3198	206.84	206.55	354.55	353.183
3707	4.24	4.03	3.87	4.12
4052	3.42	3.58	2.69	2.76
4313	2.66	2.83	2.63	2.31
4539	2.65	2.91	1.84	1.73
4753	2.77	2.81	2.31	2.03
4952	2.42	2.88	2.79	2.77
5169	2.48	2.99	2.13	2.70
5384	2.68	3.17	2.09	2.29
5598	3.87	4.80	2.35	2.84

Table 7.3: Best fitting χ^2 values for lightcurves fitted in the regions in the primary eclipse profile between (1) first and fourth contact, and (2) second and third contact. This table is graphically shown in Figure 7.14

wavelength bands than in the PHOENIX model atmosphere. The variation with wavelength relates directly to the variation of specific intensity with wavelength as previously shown in Figure 7.1.

7.6.2 First derivative lightcurve fitting

The first derivative profiles of the HST observations, in each of the 10 wavelength bands (Figure 7.6), are fitted using the χ^2 minimisation technique to the first derivatives of the PHOENIX and ATLAS model atmospheres of the same wavelength as the observations. The fits are determined using (i) the totally eclipsed section of the lightcurve between second and third contact points only, and (ii) the region of the eclipse between the first and fourth contact. Figure 7.11, case (i), and Figure 7.12, case (ii), respectively show the results for the wavelength 4535 Å. The χ^2 values for all of the lightcurves are summarised in Table 7.3.

The results show that between first and fourth contact PHOENIX gives the best fit, except for the wavelength band centred at 3198Å and 3707Å. However, the best fitting model in the region of total eclipse between second and third contact shows a wavelength dependence. For wavebands centred at 4313Å, 4539Å, and 4743Å ATLAS provides the best fit, while PHOENIX is the best fitting model atmosphere at shorter and longer wavelengths.

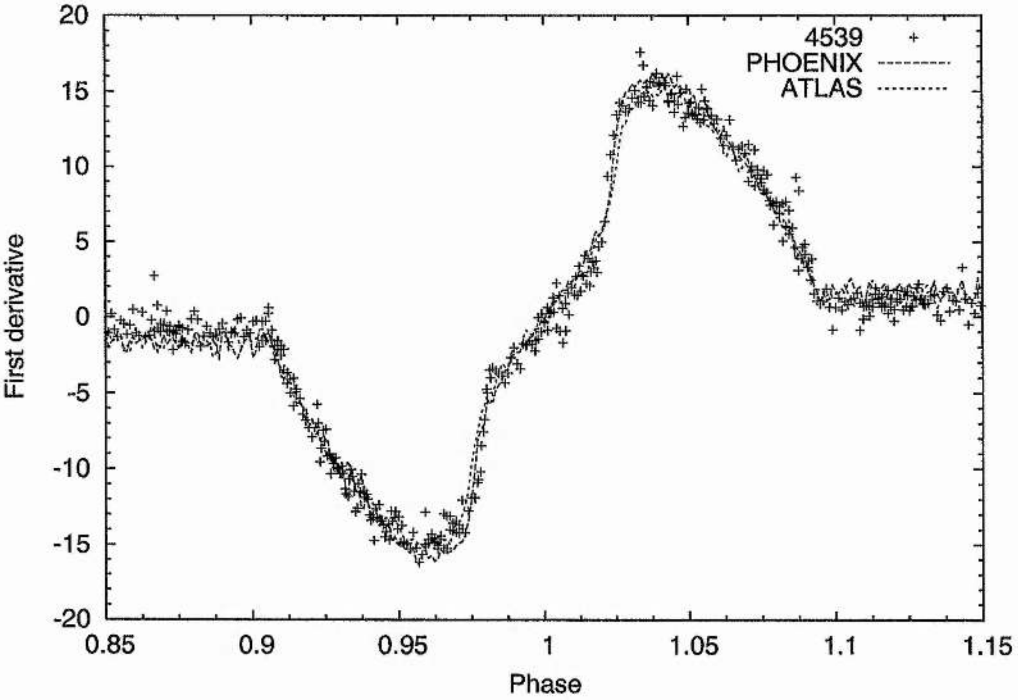

Figure 7.11: The first derivative profile centred at 4539Å, plotted with the PHOENIX and ATLAS model atmospheres. The phase range is between first and fourth contact.

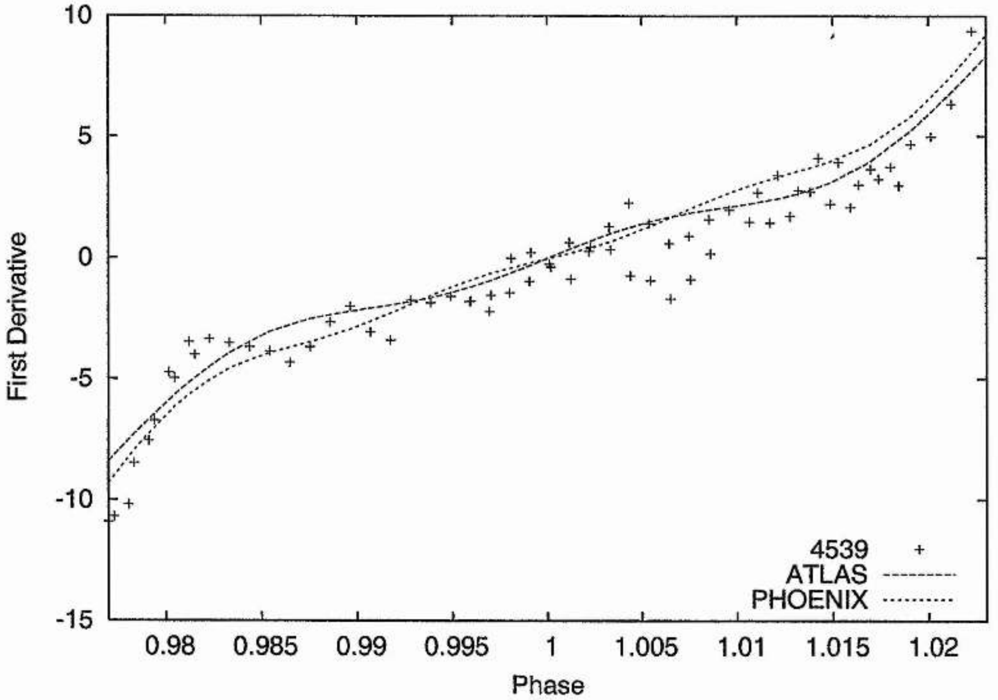

Figure 7.12: The first derivative profile centred at 4539Å, plotted with the PHOENIX and ATLAS model atmospheres. The phase range is between second and third contact.

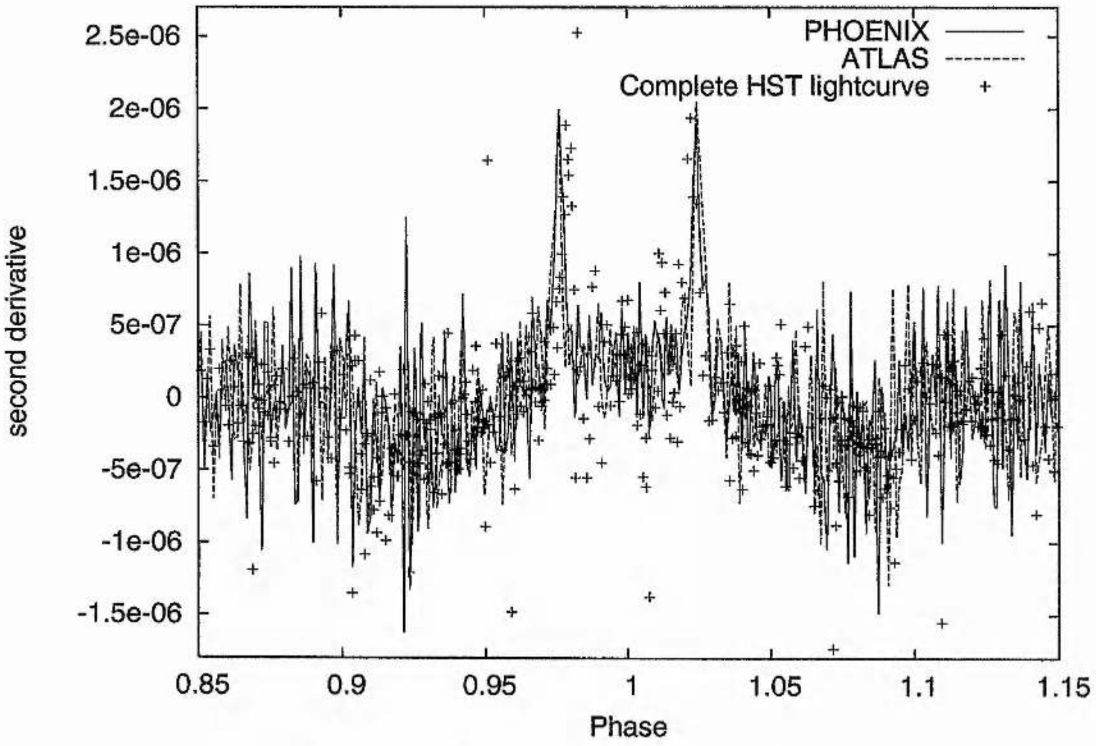

Figure 7.13: The second derivative profile using the complete HST lightcurve, plotted with the PHOENIX and ATLAS model atmospheres.

7.7 Second derivative lightcurve fitting

As with taking the first derivative of the lightcurve to determine the rate of change of the slope in the eclipse profile, we now determine the rate of change of the first derivative profile, i.e. the second derivative of the eclipse profile. The signal-to-noise ratio of the observed data set was insufficient to determine useful second derivative profiles for each of the 10 HST lightcurves. Instead we take the second derivative of the complete HST lightcurve and fit PHOENIX and ATLAS model atmospheres centred at 4670Å. We fit the second derivative profile between first and fourth contact as between second and third contact we would only fit numerical noise.

The best fitting model atmosphere is PHOENIX with a relative χ^2 of 5.02, while the ATLAS model atmosphere has a relative χ^2 of 7.23. The fit to the second derivative profile for the PHOENIX and the ATLAS model atmospheres are shown in Figure 7.13. The jitter in the models is caused by numerical noise arising from the finite number of planar surface elements used to model the star in the synthesis code.

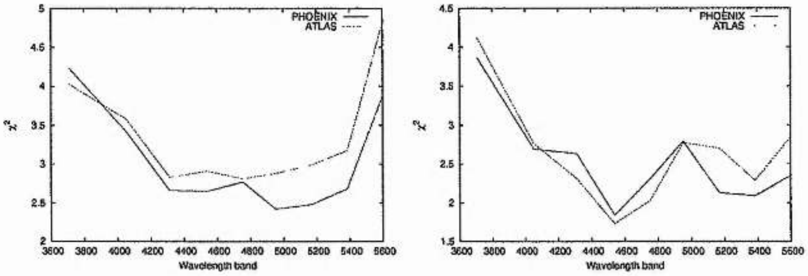

Figure 7.14: The variation of χ^2 as a function of wavelength for phases between first and fourth contact (left) and between second and third contact (right) as tabulated in Table 7.3.

7.8 Discussion and Conclusions

We have shown the wavelength dependence of limb darkening by sub-dividing the HST lightcurve into 10 bands of equal flux. The variation of flux between first and fourth contact shows that the limb darkening decreases towards longer wavelengths, confirming published limb darkening values, for example by Claret (2000). The splitting of the HST lightcurve into 10 wavelength bands also highlights the presence of a time variable bright bright feature, possibly an active region or plage on the surface of the primary star, visible in the bluest wavelength band (3198Å). The temporal variation of the bright feature is of the order of 3 days as it comes into view on the primary star between the second and third HST visit.

The ratio of the temperatures of the two stars has the effect that the secondary star acts as a dark occulting disc that scans the surface of the primary star. During partial eclipse (i.e. between first and second, and third and fourth contacts) the curvature of the lightcurve provides information about the variation of the specific intensity at the limb of the primary star. During total eclipse the curvature of the lightcurve provides information on the variation of specific intensity as a function of limb angle. The first derivative profile for each of the 10 HST wavelength bands clearly indicates the change in slope as a function of phase. Figure 7.8 shows the wavelength variation of the gradient of the first derivative profile of the HST lightcurves centred at 3707Å and 5596Å. The slope of the shorter wavelength is steeper than for the longer wavelength, consistent with the limb darkening decreasing towards longer wavelengths.

The best fitting model atmosphere is determined using χ^2 minimisation. The first derivative profile of the modelled lightcurves, generated with PHOENIX and ATLAS model atmospheres, was fitted to the HST lightcurves. The results show that ATLAS is the best fitting model atmosphere between second and third contact for central wavelengths, whereas PHOENIX provides the best fit at shorter and longer wavelengths. Between first and fourth contact PHOENIX is marginally the best fitting atmosphere. If the primary star of SV Cam was of the order of spectral type M, we would expect a greater difference between the model atmospheres.

At the limb of the star, i.e. during partial eclipse, the spherical geometry of the PHOENIX model atmosphere with its smooth cutoff (Figure 7.1) gives the best fit. This can be seen at phases ≈ 0.975 to ≈ 0.98 (just before second contact) in the fit to the observed first derivative profile (Figure 7.11). Between second and third contacts the difference between spherical and plane-parallel geometry is less important. However the slight difference in the χ^2 values for the PHOENIX and ATLAS model atmospheres shows that here, ATLAS provides only a marginally better fit at central wavelengths (4313Å, 4539Å, and 4743Å), while PHOENIX shows a slightly better fit at other wavelengths.

The first derivative profiles show a small excess in the observed flux at phase $\approx$ 0.9825 (just after second contact), compared with the fitted model atmospheres. The counterpart is present at phase 1.015, i.e. just before third contact. The increase and decrease of the first derivative at these points could imply a decrease/increase in the lightcurve for an unaccounted for emission. As this light excess is located just before the second contact point, and the reverse just before the third contact point, it could indicate that the very edge of the secondary's limb is transparent to the light of the primary star.

The signal-to-noise ratio of this data set was not high enough to determine useful second derivative profiles for each of the 10 HST lightcurves. Instead we take the second derivative of the complete HST lightcurve and fit PHOENIX and ATLAS model atmospheres centred at 4670Å to the observed lightcurve. We fit the lightcurve between first and fourth contact as there is insufficient structure to fit between second and third contact. The results show that the PHOENIX model atmosphere code gives a better fit at the limb of the star. However, PHOENIX does not provide an exact fit, which could indicate that the observed cut-off is steeper than predicted. This could be the reason why Jeffers et al. (2004c) (Chapter 6), using eclipse mapping, could not completely remove the peaks in the observed minus computed residual.

CHAPTER 8

Summary and Conclusions

This Chapter summarises the main conclusions of this thesis. The aim of this work has been to increase our understanding of the surface brightness distributions of late-type stars through Doppler imaging and eclipse mapping techniques.

8.1 Surface distribution of Spots on He 699 and AB Dor

The reconstructed surface image of He 699, from a combination of spectroscopic and photometric observations, shows a decentered polar cap with smaller features at low latitude. When the amount of low latitude surface features and the amplitude of the photometric lightcurve are compared with previous observations of Barnes et al. (2001), it is concluded that there is a correlation between the amplitude of the photometric lightcurve and the presence of low latitude spots.

Doppler images of AB Dor for both January 1992 and November 1993, show a strong polar cap, with small surface features also present. These images, to a first approximation, agree with previous results but with an increased surface resolution resulting from using LSD. It was not possible to detect differential rotation using the sheared-image method for either data set. However, as differential rotation has been measured for these data sets using a method that does not rely on MaxEnt reconstructions, the ability of MaxEnt to reconstruct individual small scale surface features has been questioned.

8.2 High Precision Eclipse-Mapping of SV Cam

8.2.1 The Deceptive Presence of Active Longitudes and Two-spots on Eclipsing Binary Stars

This work has modelled the solar size distributions extrapolated to active stars (Solanki 1999) to synthesize images of stellar photospheres with high filling factors of starspots. Synthetic eclipse light-curves were generated from these images. I attempted to recover the initial images using MaxEnt eclipse mapping. The resulting surface brightness distributions, with large spot features at the quadrature points (90° and 270°), bear little resemblance to the input distribution of spots. The reconstruction of spots at the quadrature points (90° and 270°) are not artifacts of the eclipse mapping technique, but a consequence of the χ^2 minimisation method.

It is concluded from this work that while 'active longitudes' and the 'two spot model' can be used to fit the flux deficit of the photometric lightcurve caused by spots, they can give a misleading picture of the spatial distribution of spots if the surface of the star is peppered with a large number of small unresolvable spots.

8.2.2 First Direct Evidence for a Polar Cap on SV Cam

This work provides strong evidence, independently of Doppler Imaging, that the poles of SV Cam's primary star are darkened by extensive polar caps, and that at lower latitudes the photosphere is peppered with small star-spots as has been suggested by TiO band monitoring for other active stars. It is important to establish if active stars are in fact peppered by small star-spots in addition to the presence of a polar cap, as this can significantly impact theoretical interpretations of the spot distributions on these stars. Standard colour-surface brightness relation will break down if star-spots cover a large fraction of the stellar surface, but contribute little to the stellar optical flux.

8.2.3 Eclipse Mapping of the Star-spot Distributions on SV Cam using the Hubble Space Telescope

The information content of the final image and the fit to the data were optimised with respect to various system parameters using the χ^2 landscape method. We found that dark spots are recovered on the image of the primary at first and second quadrature (phases 0.25 and 0.75). Observed minus computed residuals showed strong spurious peaks at the quadrature points. It was only possible to reduce these peaks with the addition of a polar cap, and the reduction of the primary star's temperature to account for the star being peppered with spots below the resolution limits of eclipse mapping.

8.2.4 Modelling of HST eclipsing-binary lightcurves using PHOENIX and ATLAS model atmospheres

We have shown the wavelength dependence of limb darkening by sub-dividing the HST lightcurve into 10 bands of equal flux. The variation of flux between first and fourth contact shows that the limb darkening decreases towards longer wavelengths, confirming published limb darkening values. At the limb of the star, i.e. during partial eclipse, the spherical geometry of the PHOENIX model atmosphere with its smooth cutoff gives the best fit. Between second and third contacts the difference between spherical and plane-parallel geometry is less important. However there is a wavelength dependence on the best fitting atmosphere.

8.3 Future Work

This thesis has opened up many opportunities for further research. I have been awarded 10 nights on the Telescope Bernard Lyot (TBL) to determine a surface brightness distribution and a magnetic field map of HD 221970. HD 221970 is of spectral type F6, and represents the earliest spectral type that has been Doppler imaged. Previous observations at TBL indicate that this star does indeed show bumps in its LSD profile, Figure 8.1.

I have also been awarded 3 nights at the Telescope National Galileo on La Palma to observe SV Cam using high resolution spectroscopy. From these observations I will be able to determine the size of the polar spot on SV Cam.

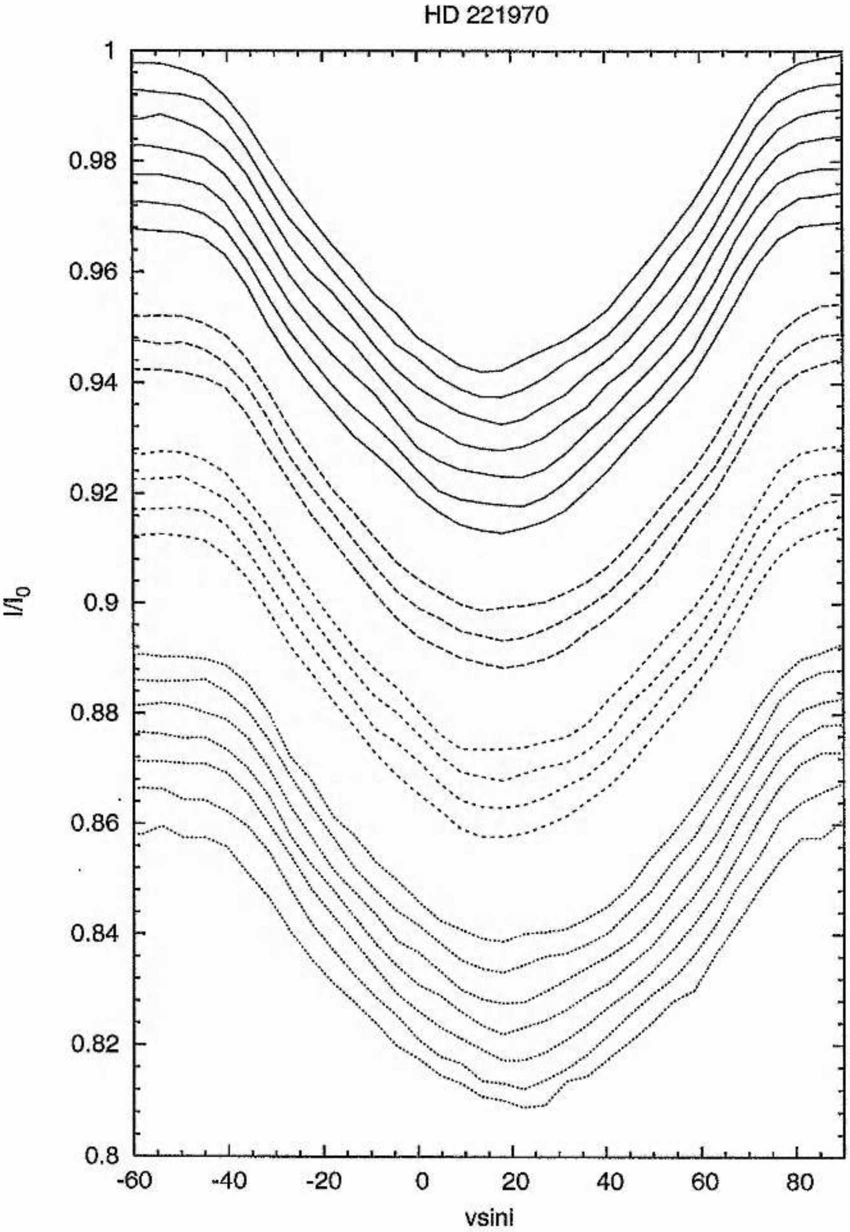

Figure 8.1: The LSD profiles of HD 221970 observed at TBL November 2003

REFERENCES

Albayrak B., Demircan O., Djurašević G., Erkapić S., Ak H., 2001, A&A, 376, 158

Allard F., Hauschildt P. H., Schweitzer A., 2000, ApJ, 539, 366

Andretta V., Doyle J. G., Byrne P. B., 1997, A&A, 322, 266

Babcock H. W., 1965, in ASSL Vol. 3: Plasma Space Science. p. 7

Baliunas S. et al., 1995, ApJ, 438, 269

Barnes J. R., Collier Cameron A., 2001, MNRAS, 326, 950

Barnes J., Collier Cameron A., James D., 1999, MNRAS, In Press

Barnes J., Collier Cameron A., Unruh Y., Donati J.-F., Hussain G., 1998, MNRAS, 299, 904

Barnes J., Collier Cameron A., James D., Donati J.-F., 2000, MNRAS, 314, 162

Barnes J. R., Collier Cameron A., James D. J., Steeghs D., 2001, MNRAS, 326, 1057

Barnes J. R., Lister T. A., Hilditch R. W., Collier Cameron A., 2004, MNRAS, 348, 1321

Beer J., Raisbeck G. M., Yiou F. Time variations of Be-10 and solar activity, p. 343, The Sun in Time, 1991

Bell S., Hilditch R., Edwin R., 1993, MNRAS, 260, 478

Berdyugina S. V., Tuominen I., 1998, A&A, 336, L25

Bogdan T., Gilman P., Lerche I., Howard R., 1988, ApJ, 327, 451

Brown S. F., Donati J.-F., Rees D. E., Semel M., 1991, A&A, 250, 463

Bruls J. H. M. J., Solanki S. K., Schüssler M., 1998, A&A, 336, 231

Bruning D. H., 1991, PASP, 103, 368

Budding E., Zeilik M., 1987, ApJ, 319, 827

Byrne P. B., 1992, in NATO ASIC Proc. 375: Sunspots. Theory and Observations. p. 63

Byrne P. B., 1996, in Stellar surface structure: proceedings of the 176th Symposium of the International Astronomical Union, held in Vienna, Austria, October 9-13, 1995. Edited by Klaus G. Strassmeier and Jeffrey L. Linsky. International Astronomical Union. Symposium no. 176, Kluwer Academic Publishers, Dordrecht. p. 299

Choudhuri A. R., Gilman P. A., 1987, ApJ, 316, 788

Choudhuri A. R., 1989, Solar Phys., 123, 217

Cini Castagnoli G., 2000, in ESA SP-463: The Solar Cycle and Terrestrial Climate, Solar and Space weather. p. 481

Claret A., 2000, A&A, 363, 1081

Collier Cameron A., Donati J.-F., 2002, MNRAS, 329, L23

Collier Cameron A., Hilditch R. W., 1997, MNRAS, 287, 567

Collier Cameron A., Unruh Y. C., 1994, MNRAS, 269, 814

Collier Cameron A., 1992, in Byrne P. B., Mullan D. J., eds, Surface Inhomogeneities on Late-type Stars. Springer-Verlag, Berlin, p. 33

Collier Cameron A., 1997, MNRAS, 287, 556

Collier Cameron A., 2001, Lecture Notes in Physics, Berlin Springer Verlag, 573, 183

DeLuca E., Fan Y., Saar S., 1997, ApJ, 481, 369

Dere K. P., Subramanian P., 2001, in IAU Symposium 203. p. 362

Deutsch A., 1958, in Lehnert B., ed, Proceedings, IAU Symposium No. 6: Electromagnetic Phenomena in Cosmological Physics. Cambridge University Press, Cambridge, p. 209

Deutsch A., 1970, ApJ, 159, 985

Djurasevic G., 1998, A&A, 127, 233

Donati J.-F., Brown S. F., 1997, A&A, 326, 1135

Donati J.-F., Collier Cameron A., 1997, MNRAS, 291, 1

Donati J.-F., Collier Cameron A., Petit P., 2003, MNRAS, 345, 1187

Donati J.-F., Semel M., Carter B., Rees D. E., Collier Cameron A., 1997, MNRAS, 291, 658

Donati J.-F., Mengel M., Carter B., Marsden S., Collier Cameron A., Wichmann R., 2000, MNRAS, 316, 699

Donati J.-F. et al., 2003, MNRAS, 345, 1145

Dzervitis U., Paupers O., Vansevicius V., 1994, Baltic Astronomy, 3, 348

Eaton J. A., Henry G. W., Fekel F. C., 1996, ApJ, 462, 888

Eddy J. A., 1978, in The New Solar Physics. p. 11

Fröhlich C., Lean J., 1998, Geophysical Research Letters, 25, 4377

Galloway D. J., Weiss N. O., 1981, ApJ, 243, 945

Goncharsky A. V., Stepanov V. V., Khokhlova V. L., Yagola A. G., 1982, SvA, 26, 690

Granzer T., Schüssler M., Caligari P., Strassmeier K. G., 2000, A&A, 355, 1087

Guthnick P., 1929, Astron. Nachr., 235, 83

Hale G. E., 1908, ApJ, 28, 315

Hall J. C., Lockwood G. W., 2004, ApJ, 614, 942

Hall D. S., 1976, in Fitch W. S., ed, Multiple Periodic Variable Stars. Reidel, Dordrecht, p. 287

Hall D. S., 1996, in IAU Symp. 176: Stellar Surface Structure. p. 217

Hatzes A. P., Vogt S. S., 1992, MNRAS, 258, 387

Hatzes A. P., Vogt S., Ramseyer T., Misch A., 1996, ApJ, 469, 808

Hatzes A. P., 1995, AJ, 109, 350

Hatzes A. P., 1998, A&A, 330, 541

Hauschildt P. H., Allard F., Ferguson J., Baron E., Alexander D. R., 1999, ApJ, 525, 871

Hempelmann A., Schmitt J. H. M. M., Schultz M., Ruediger G., Stepien K., 1995, A&A, 294, 515

Henry G. W., Eaton J. A., Hamer J., Hall D. S., 1995, ApJS, 97, 513

Hilditch R. W., McLean B. J., Harland D. M., 1979, MNRAS, 187, 797

Horne K. D., 1986, PASP, 98, 609

Hoskin P., 1999, Cambridge University Press, 49, 149

Hussain G. A. J., 2002, Astronomische Nachrichten, 323, 349

Jeffers S. V., Barnes J. R., Collier Cameron A., 2002, MNRAS, 331, 666

Jeffers S. V., Aufdenburg J. P., Hussain G. A. J., Collier Cameron A., Holzwarth V. R., 2004a, submitted to Astrophysical Journal

Jeffers S. V., Collier Cameron A., Barnes J. R., Aufdenburg J. P., Hussain G. A. J., 2004b, accepted by Astrophysical Journal

Jeffers S. V., Collier Cameron A., Barnes J. R., Donati J. F., 2004c, submitted to MNRAS

Jeffers S. V., 2004, submitted to MNRAS

Jetsu L., 1996, A&A, 314, 153

Johns-Krull C. M., Hatzes A. P., 1997, ApJ, 487, 896

Kitchatinov L. L., Rüdiger G., 1999, A&A, 344, 911

Kitchatinov L. L., Jardine M., Donati J.-F., 2000, MNRAS, 318, 1171

Kjurkchieva D., Marchev D., Ogloza W., 2000, Acta Astronomica, 50, 517

Kjurkchieva D. P., Marchev D. V., Zola S., 2002, A&A, 386, 548

Korhonen H., Berdyugina S. V., Strassmeier K. G., Tuominen I., 2001, A&A, 379, L30

Kosovichev A. G. et al., 1997, Solar Phys., 170, 43

Kratzwald L., 2002, in Masters Thesis, Univ. Vienna

Kron G. E., 1947, PASP, 59, 261

Kuerster M., Dennerl K., 1993, in ASSL Vol. 183: Physics of Solar and Stellar Coronae. p. 443

Kurucz R. L., 1993, CDROM # 13 (ATLAS9 atmospheric models) and # 18 (ATLAS9 and SYNTHE routines, spectral line database), Cambridge, MA

Lanza A. F., Catalano S., Cutispoto G., Pagano I., Rodono M., 1998, A&A, 332, 541

Lanza A. F., Rodonò M., Mazzola L., Messina S., 2001, A&A, 376, 1011

Lehmann H., Hempelmann A., Wolter U., 2002, A&A, 392, 963

Leighton R. B., 1964, ApJ, 140, 1547

Leighton R. B., 1969, ApJ, 156, 1

Livingston W., 2002, Solar Phys., 207, 41

Love J., 1999, Astronomy and Geophysics, 40, 14

Maceroni C., Vilhu O., van't Veer F., van Hamme W., 1994, A&A, 288, 529

McGurk P., 1998, Clarendon Press, 3, 183

Mills D., 1994, Technical Report 152, Rutherford Appleton Laboratory

Narain U., Ulmschneider P., 1990, Space Sci. Rev., 54, 377

O'Dell M. A., Collier Cameron A., 1993, MNRAS, 262, 521

O'Dell M. A., Hendry M. A., Collier Cameron A., 1994, MNRAS, 268, 181

Oláh K., Strassmeier K. G., 2002, Astron. Nachr., 323, 361

Olah K., Hall D. S., Henry G. W., 1991, A&A, 251, 531

Oláh K., Strassmeier K. G., Weber M., 2002, A&A, 389, 202

O'Neal D., Neff J., Saar S., 1998, ApJ, 507, 919

Parker E. N., 1955, ApJ, 122, 293

Patkos L., Hempelmann A., 1994, A&A, 292, 119

Petit P., Donati J.-F., Collier Cameron A., 2002, MNRAS, 334, 374

Pojmanski G., 1998, Acta Astronomica, 48, 711

Popper D. M., 1996, ApJS, 106, 133

Priest E. R., Smith E. A., 1979, Solar Phys., 64, 267

Priest E. R., 1984, Solar Magnetohydrodynamics. D. Reidel, Dordrecht

Prosser C. F., Stauffer J., Kraft R. P., 1991, AJ, 101, 1361

Rüdiger G., Küker M., 2002, A&A, 385, 308

Radick R. R., Lockwood G. W., Skiff B. A., Baliunas S. L., 1998, ApJS, 118, 239

Rainger P. P., Hilditch R. W., Edwin R. P., 1991, MNRAS, 248, 168

Reiners A., Schmitt J. H. M. M., 2002, A&A, 384, 155

Rice J. B., Strassmeier K. G., 1996, A&A, 316, 164

Rice J. B., Wehlau W. H., Khokhlova V. L., 1989, A&A, 208, 179

Rucinski S. M., Lu W., Capobianco C. C., Mochnacki S. W., Blake R. M., Thomson J. R., Ogłoza W., Stachowski G., 2002, AJ, 124, 1738

Rüdiger G., Elstner D., 1994, A&A, 281, 46

Schrijver C. J., Title A. M., 2001, ApJ, 551, 1099

Schüssler M., Solanki S. K., 1992, A&A, 264, L13

Skilling J., Bryan R. K., 1984, MNRAS, 211, 111

Soderblom D. R., Stauffer J. R., Hudon J. D., Jones B. F., 1993b, ApJS, 85, 315

Solanki S. K., 1999, in ASP Conf. Ser. 158: Solar and Stellar Activity: Similarities and Differences. p. 109

Spruit H. C., Van Ballegooijen A. A., 1982, A&A, 106, 58

Spruit H. C., Weiss A., 1986, A&A, 166, 167

Spruit H. C., 1994, A&A, 289, 441

Stauffer J. R., Hartmann L. W., Burnham N., Jones B. F., 1985, ApJ, 289, 247

Stauffer J. R., Caillault J. P., Gagne M., Prosser C. F., Hartmann L. W., 1994, ApJS, 91, 625

Stauffer J. R., Jones B. F., Backman D., Hartmann L. W., Barrado y Navascués D., Pinsonneault M. H., Terndrup D. M., Muench A. A., 2003, AJ, 126, 833

Steenbeck M., Krause F., Rädler K. H., 1966, Zeitschrift Naturforschung Teil A, 21, 369

Stepien K., Kiraga M., Muthsam K. J. H. J., 1997, Acta Astron., 47, 235

Strassmeier K. G., Bartus J., 2000, A&A, 354, 537

Strassmeier K. G., Rice J. B., 1998, A&A, 339, 497

Strassmeier K. G., Rice J. B., Wehlau W. H., Hill G. M., Matthews J. M., 1993, A&A, 268, 671

Strassmeier K. G., Bartus J., Kovari Z., Weber M., Washuettl A., 1998, A&A, 336, 587

Strassmeier K. G., Lupinek S., Dempsey R. C., Rice J. B., 1999, A&A, 347, 212

Strassmeier K. G., 1994, A&A, 281, 395

Strassmeier K. G., 2000, A&A, 357, 608

Strassmeier K. G., 2002, Astronomische Nachrichten, 323, 309

Thurl C., Sackett P. D., Hauschildt P. H., 2004, Astron. Nachr., 325, 247

Unruh Y. C., Collier Cameron A., 1997, MNRAS, 290, L37

Unruh Y. C., Collier Cameron A., Cutispoto G., 1995, MNRAS, 277, 1145

Unruh Y. C., Collier Cameron A., Guenther E., 1998, MNRAS, 295, 781

Usoskin I. G., Mursula K., Solanki S., Schüssler M., Alanko K., 2004, A&A, 413, 745

van Helden A., 1996, in Proc. Am. Phil. Soc., 140, 358

van Leeuwen F., Alphenaar P., Meys J. M. M., 1987, A&AS, 67, 483

Vernazza J. E., Avrett E. H., Loeser R., 1981, ApJS, 45, 635

Vincent A., Piskunov N. E., Tuominen I., 1993, A&A, 278, 523

Vogt S. S., Penrod G. D., 1983, ApJ, 275, 661

Vogt S. S., Hatzes A. P., Misch A. A., Kürster M., 1999, ApJS, 121, 547

Washuettl A., Strassmeier K. G., Collier-Cameron A., 2001, in ASP Conf. Ser. 223: 11th Cambridge Workshop on Cool Stars, Stellar Systems and the Sun. p. 1308

Weber M., Strassmeier K. G., 1998, A&A, 330, 1029

Wilson O. C., 1968, ApJ, 153, 221

Zboril M., Djurašević G., 2003, A&A, 406, 193

Zeilik M., de Blasi C., Rhodes M., Budding E., 1988, ApJ, 332, 293